

Strong-field photoelectron imaging of complex molecules

Dissertation

**zur Erlangung des Doktorgrades an der Fakultät für
Mathematik, Informatik und Naturwissenschaften**

Fachbereich Chemie der Universität Hamburg

vorgelegt von

Joss Wiese

Hamburg

2020

Gutachter der Dissertation: Prof. Dr. Jochen Küpper
Prof. Dr. Gabriel Bester

Mitglieder der Prüfungskommission: Prof. Dr. Jochen Küpper
Prof. Dr. Gabriel Bester
Prof. Dr. Henry Chapman
Prof. Dr. Carmen Herrmann
Prof. Dr. Holger Lange

Datum der Disputation: 11. September 2020

Datum der Druckfreigabe: 11. September 2020

Eidesstattliche Versicherung

Hiermit versichere ich an Eides statt, die vorliegende Dissertationsschrift selbst verfasst und keine anderen als die angegebenen Hilfsmittel und Quellen benutzt zu haben. Die eingereichte schriftliche Fassung entspricht der auf dem elektronischen Speichermedium. Die Dissertation wurde in der vorgelegten oder einer ähnlichen Form nicht schon einmal in einem früheren Promotionsverfahren angenommen oder als ungenügend beurteilt.

Hamburg, den 29. September 2020

Joss Wiese

Zusammenfassung

Die Bildgebung mittels Starkfeldionisation ermöglicht das Messen und Visualisieren von Molekülstruktur mit pikometer-räumlicher und femtosekunden-zeitlicher Auflösung. Der zugrunde liegende Ionisationsprozess wird durch das intensive elektrische Feld eines Laserpulses ausgelöst und erlaubt das selektive Entfernen eines einzelnen Elektrons aus den äußersten Valenzorbitalen des zu untersuchenden Moleküls. Das dabei entstehende Photoelektron trägt Informationen über die entsprechenden Molekülorbitale und offenbart bestimmte Aspekte der Topologie dieses chemisch reaktivsten Teils der Elektronenwolke des Moleküls. Des Weiteren kann das intensive Laserfeld dazu verwendet werden, das Photoelektron zum Molekülion zurückzutreiben, was zu einer möglichen Kollision bei hohem Impuls führen kann. Aus dem dabei auftretenden Beugungsmuster kann dann die räumliche Anordnung von Atomen innerhalb des Moleküls ermittelt werden.

Diese Doktorarbeit behandelt die Abbildungen von molekularer Struktur in der Photoelektronenimpulsverteilung, die im Zuge des initialen Ionisationsschrittes und darauf folgender Rekollisionen zwischen Elektron und Molekül entstehen. Es werden Experimente und Simulationen zur Starkfeldphotoelektronenbildgebung präsentiert, welche die Moleküle Carbonylsulfid, Indol sowie den Wasserstoffbrückenkomplex Indol-H₂O untersuchen. Eine allgemeine theoretische Beschreibung der zeit- und raumintegrierten Interaktion zwischen Laser und Molekül wird für einen gepulsten Laserstrahl vorgestellt, der in einen Gasphasenmolekularstrahl fokussiert wird. Diese ermöglicht die Bewältigung der Intensitätsmittelung im Laserfokusvolumen, welche ein gängiges Problem in Starkfeldionisationsstudien darstellt, und eröffnet einen genauen Einblick in die Photoelektronenbildgebung von Carbonylsulfid. Anhand desselben Moleküls wird außerdem die Dynamik der starkfeldgetriebenen Kollisionen zwischen Photoelektron und Molekül entschlüsselt, wobei insbesondere die Auswirkungen der Knotengeometrie in den betroffenen Molekülorbitalen in einer sowohl experimentellen als auch computergestützten Studie beleuchtet werden. In einem weiteren Experiment wird zudem die Erzeugung einer reinen Probe von Indol-H₂O unter starker Laser-Ausrichtung demonstriert, wodurch dieses prototypische Teilstück eines solvatisierten Proteins für Photoelektronenbildgebung im Molekülrahmen zugänglich gemacht wird. Schließlich wird die Starkfeldionisation des komplexen Moleküls Indol ausgiebig behandelt, mittels stark kontrollierter Photoelektronenbildgebungsexperimente sowie eines neuen und hocheffizienten Starkfeldionisationsmodells, welches die Beschreibung elastischer Rekollisionen zwischen Photoelektron und Molekül mit quantenchemischer Genauigkeit ermöglicht. Eine tomographisch gemessene, dreidimensionale Photoelektronenimpulsverteilung erlaubt es zudem, den Ionisationsprozess dieses komplexen Moleküls in seinem natürlichen Koordinatensystem innerhalb des optischen Zyklus' des Lasers zu verfolgen, und zeigt die Unterschiede in der Manifestation von molekularer Struktur entlang resonanter und nichtresonanter Ionisationswege auf. Die neu gewonnenen Erkenntnisse, die in dieser Dissertation vorgestellt werden, befördern das Verständnis sowie die Kontrolle von Valenzelektronen- und selbstbeugungsvermittelter Molekülbildgebung, womit entscheidende Schritte in Richtung der Realisierung des langersehnten *Quantenmolekülfilms* gemacht werden.

Abstract

Strong-field ionisation imaging offers elegant ways to measure and visualise molecular structure with picometre spatial and femtosecond temporal resolution. The underlying ionisation process is driven by an intense laser-electric field and allows to selectively extract a single electron from the outermost valence orbital(s) of the target molecule. The arising photoelectron carries information on the molecular orbital(s) from which it escaped, revealing topological details about this most reactive portion of the molecule's electron cloud. Moreover, the intense laser field can be used to drive the photoelectron back to the molecular ion, leading to electron–molecule collisions at high momentum, which allow to determine the arrangement of atoms within the molecule from the resulting diffraction pattern.

This doctoral work deals with the signatures of molecular structure in the photoelectron's momentum distribution as they arise from the initial ionisation step and subsequent electron–molecule recollisions. Strong-field photoelectron imaging experiments and simulations are presented that tackle the molecules carbonyl sulfide, indole and the hydrogen-bond cluster indole–H₂O. A theoretical description of the time- and space-integrated laser–target interaction is introduced for a pulsed laser beam that is focussed into a gas-phase molecular beam. This treatment allows to overcome focal-volume intensity averaging, which is a common problem in strong-field ionisation studies, and enables an intimate view on photoelectron imaging of carbonyl sulfide. The same molecule is moreover employed to unravel the dynamics of strong-field-driven photoelectron–molecule collisions, shining light onto the impact of molecular-orbital nodal structure in a combined experimental and computational survey. Furthermore, the experimental creation of a pure and strongly laser-aligned sample of indole–H₂O is demonstrated, enabling molecular-frame photoelectron imaging of this prototypical snippet of a solvated protein. Finally, strong-field ionisation of the complex molecule indole is studied extensively by means of highly controlled photoelectron imaging experiments as well as a novel and very efficient strong-field ionisation model, which allows for the quantum-chemically exact description of elastic photoelectron–molecule recollisions. A tomographically measured, three-dimensional photoelectron momentum distribution provides deep insights into the ionisation process of this complex molecule on a sub-laser-cycle level and reveals how resonant and nonresonant ionisation pathways differently encode molecular structure. The findings presented in this thesis advance the understanding and control of valence-electron and self-diffractive imaging of complex molecules, making crucial steps towards the ultimate goal of realising the *quantum molecular movie*.

Contents

Zusammenfassung	v
Abstract	vii
1. Introduction	1
2. Fundamental concepts	5
2.1. Atoms and molecules in electric fields	6
2.1.1. Quantum-state selection and species separation	6
2.1.2. Laser alignment	8
2.1.3. Strong-field ionisation	10
2.2. Imaging techniques	12
2.2.1. Tomographic imaging	12
2.2.2. Coulomb-explosion imaging	14
2.2.3. Laser-induced electron diffraction	16
3. Strong-field photoelectron imaging at finely resolved incident intensities	17
3.1. Introduction	17
3.2. Intensity-difference signals	18
3.3. Experimental setup	21
3.4. Results and discussion	22
3.4.1. Integral photoelectron yield	22
3.4.2. Radial and angular distributions	22
3.5. Conclusions	27
4. The role of molecular-orbital structure in strong-field-driven electron–molecule collisions	29
4.1. Introduction	29
4.2. Results	30
4.2.1. Experimental approach	30
4.2.2. Photoelectron momentum distributions	30
4.2.3. Quantum-mechanical model of the electron dynamics	32
4.2.4. Semiclassical model of the electron dynamics	32
4.2.5. Differential analysis of the momentum distributions	34
4.3. Discussion	34
5. Strong laser alignment of solvent–solute aggregates in the gas-phase	37
5.1. Introduction	37
5.2. Experimental setup	38
5.3. Results	39
5.4. Discussion	41
5.5. Conclusions	42
6. Modelling strong-field tunnel ionisation of complex molecules	43
6.1. Introduction	43

6.2. Semiclassical model	44
6.2.1. Initial photoelectron wavefunction	45
6.2.2. Continuum propagation	46
6.2.3. Asymptotic wavefunction	47
6.3. Computational setup	48
6.4. Experimental setup	49
6.5. Results and Discussion	50
6.6. Conclusions	53
7. Disentangling strong-field multiphoton ionisation of a complex molecule through photoelectron tomography	55
7.1. Introduction	55
7.2. Experimental setup	56
7.3. Results and discussion	56
7.4. Conclusions	61
8. Conclusions and outlook	63
8.1. Molecular strong-field photoelectron imaging	63
8.2. Further experimental campaigns	66
Appendices	69
A. Photoelectron-dynamics calculations for OCS	71
A.1. Numerical quantum-dynamics simulations	71
A.2. Semiclassical trajectory simulations	72
A.2.1. Initial electron wavepacket	72
A.2.2. Classical propagation	75
B. Quantum-chemistry calculations for indole	77
B.1. Equilibrium geometry and electrostatic properties	77
B.2. Field-direction model	79
B.3. Cationic electric field	79
Bibliography	81
Acknowledgements	95
Acronyms	96
Chemical hazard and precautionary statements	97
List of publications	102

1 Introduction

Life on earth is driven by biomolecules. The underlying, multifaceted biochemical machinery is composed of proteins in many different sizes and shapes, with a human being comprising billions of chemically unique species¹. In a well-coordinated concert, these macromolecules run the essential processes in all living organisms. They enable the replication of genetic information, empower metabolic activity like energy harvesting and matter transport, and allow the exchange of stimuli among cells. Many proteins moreover have enzymatic character, being able to enormously speed up biochemical reactions by several orders of magnitude².

The function of each protein is determined by its three-dimensional structure, which arises from a one-dimensional sequence of amino acids. These individual building blocks introduce functional groups that are strung together along the peptide backbone of the protein and enable concerted intra- and intermolecular interactions. While the interplay among such functional groups within the protein shape the final three-dimensional structure of the macromolecule, their interaction with other molecules or ions gives rise to the biochemical activity. A protein's role within an organism is therefore highly dependent on its structure, enabling it to tackle very specialised tasks like molecular recognition at high specificity, binding of ligands at extraordinary strengths or catalysing biosynthetic processes that would take millions of years without it³. Such relationships between structure and function are at the heart of the molecular sciences.

In many cases, the establishment of just a single bond between a protein and another molecule results in dramatic changes of the protein's overall shape. An example for such behaviour is haemoglobin, which acts as an oxygen transporter in the blood of almost all vertebrates. This protein carries four iron atoms that each provide a binding site for one oxygen molecule. Although the attachment of just a single oxygen molecule in first instance only affects the distribution of electron density at the respective iron site, it is followed by a large-scale deformation of the whole protein complex⁴. A subtle modification on a single-atom level thereby triggers the motion of ten thousand atoms. The case of haemoglobin demonstrates the necessity to observe a biomolecule across a large range of length scales, if one aims at a full understanding of its structure and function. At the same time, the crucial reactive sites need to be examined in quantum-mechanical detail.

Before we are going to discuss certain ways to view the static and dynamic appearance of molecules, let us take a brief look at molecular structure in general. A molecule is a union of multiple atoms that are held together by chemical bonding, the sharing of electron density between the nuclei. The spatial arrangements of the atomic cores and of the surrounding electron cloud stand in continuous interaction with each other, striving at the minimisation of the system's total energy. In order to take a snapshot of a molecule in its entirety, one needs to capture both the positions of the nuclei and the topology of the electron density. Since chemical activity mainly arises from the most loosely bound valence electrons of a molecule, it is of particular importance to track especially these most reactive portions of the electron density. So by following the instantaneous positions of the atomic cores and the electron density associated with the valence electrons, one gains full access to the chemically relevant dynamical structure of the target molecule, the so-called *quantum molecular movie*. Its realisation still remains to be demonstrated, since it poses several technical challenges, some of which will be discussed in the following.

The relative positions of a molecule's atomic nuclei can be determined by diffraction measurements. Most commonly, either photons or electrons are sent through the target molecule of choice and the resulting interference pattern in momentum space is recorded, which encodes the inverse interatomic distances of the sample. The portion of the diffraction signal that offers the most straightforward

access to molecular structure originates from elastic scattering off the molecule and needs to be isolated from other, unwanted contributions that arise from competing inelastic processes⁵. To eventually reconstruct the geometrical arrangement of atoms from which the molecule is built up, it is essential to know both intensity and phase of the elastically scattered wave. But since usually only the intensity is measured in such diffraction experiments, the phase often needs to be retrieved *a posteriori* in an iterative procedure⁶.

The desired spatial resolution of a diffraction experiment is determined by the bond lengths in the target molecule, which are typically in the order of $0.1 \text{ nm} = 10^{-10} \text{ m}$. This imposes certain requirements on the wave that is used for the interrogation of molecular structure. If electromagnetic radiation is employed, its wavelength is demanded to be sufficiently short, following the Abbe diffraction limit, which puts it into the hard x-ray regime. The underlying process can be described through Thomson scattering of an x-ray photon off the molecule's electron density⁷, resulting in a diffraction pattern that allows to infer the atomic positions at the instant of the light-matter interaction. X-ray diffractive measurements have revealed a vast number of intriguing details about biomolecular topology, for instance the double-helical form of DNA⁸ and the three-dimensional structure of the ribosome⁹.

Using electrons instead to probe molecular structure changes the scattering mechanism itself and therefore the requirements to the experimental setup. In contrast to photons, electrons are charged particles and possess a rest mass. As a consequence, the process of electron scattering involves the whole Coulomb potential of the molecule and is especially sensitive to the atomic nuclei. The wavelength of an electron is reciprocally linked to its momentum through the de Broglie wave equation. Accordingly, a typical bond length can be resolved with an electron that impinges on the molecule with a kinetic energy of at least 150 eV. A prominent example of a biomolecule, whose structure was determined by means of electron diffraction, is the light-harvesting complex of chlorophyll¹⁰.

Both x-ray as well as electron diffraction can therefore be used to investigate static molecular structure. However, in order to trace a (bio)chemical process through all its stages it is essential to follow how the structures of the affected molecules evolve with time. The motion of atomic cores within a molecule occurs on the femtosecond (10^{-15} s) to picosecond (10^{-12} s) scale. In principle, such ultrafast structural dynamics can be interrogated with the aid of the so-called pump-probe scheme¹¹, which allows to follow the evolution of a molecule after excitation with a short laser pulse, the pump pulse. By setting the time interval between this pump and a second, delayed pulse, which probes the current structure of the target, one obtains a molecular snapshot at a controllable and well-defined point in time. Fundamentally, this scheme requires both pump and probe pulse to be shorter than the process to be observed.

Yet there exists another reason for choosing ultrashort pulses, even for investigating static molecular structure, as the exposure to x-rays or electrons at high dose may cause severe damage of the target. The usage of correspondingly short probe pulses, in the order of a few tens of femtoseconds or shorter, enables an investigator to outrun such radiation damage and record a diffraction pattern that reflects the target's structure before the onset of fragmentation^{12,13}. Thus, it is crucial to carefully control both wavelength and duration of the light or electron pulse that is employed to measure the arrangement of atoms in a molecule, whether static or dynamic.

Now let us have a look at how to capture the second component of the *quantum molecular movie*, the valence electron density. To understand and predict a molecule's chemical behaviour one needs to examine these most reactive of its bound electrons. At which sites within the molecule is this part of the electron density located? And where are possible nodes – planes of zero electron density – in the affected valence orbitals? The answers to those questions permit to spot where new chemical bonds are likely to be established or where existing ones might be broken. This flow of valence electron density represents the essence of chemistry and takes place on the attosecond (10^{-18} s) to femtosecond scale.

X-ray diffraction is quite insensitive to this most reactive portion of the electron density, because the related scattering signal is dominated by the inert electrons that populate the core and inner valence orbitals¹⁴. Neither does electron diffraction provide isolated information on the outer valence electrons alone, since the scattering process involves the whole Coulomb potential of the molecule. However, there exists an elegant way to address exclusively these chemically active electrons. By exposing the molecular target to an intense laser-electric field, strong enough to deform the molecule's electronic cloud, one can selectively extract a single electron from the outermost valence orbital(s). This process is called strong-field ionisation and the momentum of the freed photoelectron encodes the sought-after information on the respective valence orbital(s). By carefully recording and analysing such photoelectron momentum distributions an experimenter may visualise the nodal structure of molecular orbitals¹⁵ or image the transient localisation of valence electron density^{16,17}.

Yet strong-field ionisation offers even further opportunities to detect molecular structure. Once an electron gets detached from its parent molecule, it is born into a continuum that is heavily dominated by the strong laser-electric field. As a consequence, the nascent photoelectron experiences periodic acceleration that follows the polarisation of the laser. At linear polarisation, the electron may be driven back to the molecular ion, possibly resulting in a recollision at high momentum. It is these recollision events that allow further insights into the target molecule.

If the recolliding electron scatters elastically off the molecule, it produces an interference pattern that encodes the interatomic distances, similar to conventional electron diffraction. Such laser-driven self-diffraction, however, has the inherent advantage that it occurs just a few femtoseconds after ionisation – independent of the actual laser pulse duration – and at extremely high current density¹⁸. This method is called laser-induced electron diffraction (LIED) and complements strong-field photoelectron imaging to form a wholistic approach that might enable the simultaneous recording of the full *quantum molecular movie*. So far LIED experiments could successfully be employed to determine the atomic coordinates of several simple molecules like carbonyl sulfide¹⁹, acetylene²⁰, water²¹ and benzene²². But the extension of this method to more complex molecular targets still remains a matter of ongoing research. The growing complexity of the molecule comes along with an increased intricacy of both the ionisation and the recollision process, which will be discussed extensively in the course of this thesis.

Besides elastic scattering the returning electron can also inelastically interfere with its parent ion. In the most prominent inelastic process the recollision event leads to a recombination of electron and molecular ion, releasing a burst of light that reflects the properties of the returning electron. The emitted light flash exhibits a spectrum that extends to high multiples of the incident laser frequency and has a duration in the order of attoseconds. This process, termed high harmonic generation, can be employed to create tailored attosecond laser pulses in the extreme ultraviolet for the investigation of ultrafast molecular dynamics²³. Moreover, the emitted burst of light carries temporally concise information on the molecular ion, corresponding to the instant of the electron–molecule collision. It allows to reconstruct molecular orbitals and to perform transient spectroscopy that can keep up with the motion of bound electrons²⁴.

Owing to the intriguing detail that can be revealed by means of such strong-field-driven recollisions, it is of particular interest to the molecular-physics community to advance the understanding and control of the underlying photoelectron motion. It represents one key aspect of this doctoral work.

Another crucial facet of molecule imaging is the access to the molecular frame, which allows to switch from the laboratory to the molecule perspective. Many imaging experiments – and all those presented in this thesis – are conducted in the gas phase in order to study the intrinsic properties of isolated molecules, segregated from any unwanted interactions with their environment. As a result, an experimenter needs to cope with molecules that are randomly oriented in the laboratory frame. In principle, two different routes can be followed in order to enter the molecular frame: One can either make sure that all molecules are in the same orientation when the imaging snapshot is taken or one infers each molecule's individual orientation *a posteriori*. While either approach comes

with certain advantages and disadvantages, the former is more generally applicable – especially to complex molecules – and was employed exclusively in this work. Eventually, the access to the molecular frame makes molecular-orbital imaging feasible in the first place¹⁵ and strongly benefits the structure retrieval from diffraction measurements^{25–28}.

This thesis deals with strong-field ionisation imaging of molecules, with the aim to trace back and decode different kinds of molecular structure, as they leave their fingerprints during the strong-field interaction with the laser field. It is structured as follows: In chapter 2, the fundamental concepts are described to state-select, control and image molecules. In chapter 3, a survey is presented that advances the acquisition of strong-field ionisation data in general, enabling a view on photoelectron imaging of carbonyl sulfide in quantum-mechanical detail and providing the separate analysis of resonant and nonresonant ionisation pathways. Chapter 4 illuminates the photoelectron-recollision dynamics for the same molecule, in particular investigating the influence of molecular-orbital structure in a combined experimental and computational study. In chapter 5, an experimental route is demonstrated to obtain a pure sample of indole–H₂O under strong spatial control, making this prototypical snippet of a solvated protein accessible to molecular-frame photoelectron imaging. The chapters 6 and 7 deal with the strong-field ionisation of indole in its molecular frame. In chapter 6, photoelectron imaging following linearly polarised laser fields is unravelled. Experimentally acquired images, recorded at a high degree of control, are discussed alongside their computationally obtained equivalents, introducing a novel and highly efficient strong-field ionisation model that allows for a detailed, quantum-chemically exact description of photoelectron–molecule recollisions. Chapter 7 gives intimate insights into the strong-field ionisation processes taking place in a complex molecule, disentangling photoelectron imaging at circular polarisation in a purely experimental survey. The tomographically acquired, three-dimensional photoelectron data enable the individual analysis of resonant and nonresonant ionisation paths and allow to identify the respective instants of ionisation during the optical cycle of the laser. Finally, chapter 8 summarises and concludes the findings of this doctoral work, followed by an outlook on future strong-field ionisation surveys. Moreover, further experimental campaigns are briefly summarised, which tackled miscellaneous objectives in molecular physics. These campaigns represent side projects that I participated in during the past years as a doctoral student and acquainted me with various experimental techniques and theoretical models in this field of research.

2 Fundamental concepts

This chapter provides a brief introduction into the theoretical, experimental and numerical methods and concepts used throughout this thesis.

For the imaging of molecular structure, which comprises both the topology of the electron density and the arrangement of atomic cores, it is crucial to have a high degree of control over the target molecule^{15,28} and the imaging process itself²⁹. In order to study the intrinsic, unperturbed nature of a molecule it is essential to isolate it from its environment. For this purpose, all experiments that are discussed in this thesis were conducted in the gas phase, which ensured the suppression of any unwanted intermolecular interactions.

Another generally important aspect of molecule-imaging experiments is the accumulation of data until an image of sufficiently high quality is obtained. In the vast majority of studies the underlying imaging procedure has to be repeated many times under identical conditions, which requires picturing many copies of the target molecule of choice. Accordingly, the time needed to record such a molecule snapshot is affected by both the repetition rate of the experiment and the number of molecules that are illuminated at the same time within one shot. This requires all individual molecules that contribute to the same image to be identical, i. e., ideally they should all be in the same quantum state and share the same orientation in the laboratory-fixed frame.

The creation of cold and dense molecular gas-phase ensembles can be achieved by means of a pulsed supersonic expansion. The method used in this work relies on the periodic co-expansion of the target compound, seeded in an inert carrier gas at high pressure, into vacuum. Typical carriers are noble gases at pressures between 10 and 100 bar that are expanded into a compartment at $\leq 10^{-6}$ mbar. This pressure difference, spanning many orders of magnitude, rapidly drives the gas mixture through a small orifice that connects the high-pressure reservoir with the vacuum. As a consequence, the embedded molecules undergo many collisions with the lighter carrier-gas atoms during the expansion. This leads to an energy transfer from molecules to carrier atoms, which cools the target's internal degrees of freedom and leaves the carrier with a higher translational energy. The resulting supersonic jet accommodates sample molecules that are exclusively in the electronic and vibrational ground state and possess a rotational temperature in the order of 1 K. Further refinement of the molecular ensemble in terms of quantum-state selection and species purification can be obtained through manipulation with static electric fields, which is elaborated in subsection 2.1.1.

To eventually get a glimpse at the target molecule in its natural, molecule-fixed frame one needs to collectively hold all molecular replicas in an ensemble in a mutual orientation at the moment when the imaging snapshot is taken. Both the three-dimensional fixation and the interrogation of molecular structure can be achieved through irradiation with intense laser pulses. The underlying physical processes are at the heart of matter interacting with strong electric fields and are further

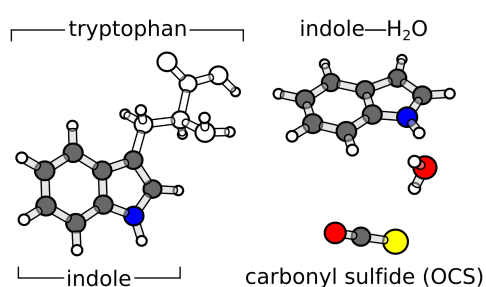


Figure 2.1: The bicyclic indole molecule (C_8H_7N) represents the aromatic side chain of the amino acid tryptophan. Its hydrogen-bonded water cluster indole-H₂O has a well-defined minimum-energy conformation. In contrast to these two asymmetric-top molecules OCS is a linear rotor. In the ball-and-stick representations shown, H atoms appear as white, C atoms as grey, N atoms as blue, O atoms as red and S atoms as yellow spheres. The amino-acid backbone of tryptophan is coloured in white.

described in section 2.1. Section 2.2 gives a brief overview of relevant imaging techniques.

The three main molecular species that were studied through imaging experiments and computations in the frame of this work were: carbonyl sulfide (OCS), indole and its 1:1 water cluster indole–H₂O. See Figure 2.1 for ball-and-stick representations of these compounds. While OCS served as a test case to further understand and improve strong-field-ionisation imaging in general in chapters 3 and 4, indole and indole–H₂O were intensely enquired through photoelectron and photoion imaging in the molecular frame, which is described in chapters 5, 6 and 7. Indole represents the aromatic side chain of the essential amino acid tryptophan, making it the major ultraviolet-absorbing chromophore of proteins³⁰. It is therefore a crucial prototypical biomolecular building block, whose molecular properties shape the protein-based machinery of life. The indole–H₂O cluster, moreover, offers the rare opportunity to investigate the first step of a biomolecule’s solvation through the formation of hydrogen bonds. Due to the ubiquity of water in biological systems, the exhaustive understanding of such elementary intermolecular interactions grants access to the core of biochemical reactions.

Unless stated otherwise, atomic units are used throughout this thesis, $\hbar = m_e = e = 1$, with the reduced Planck constant \hbar , the electron mass m_e and the elementary charge e .

2.1. Atoms and molecules in electric fields

The interaction of matter with external electric fields is at the core of this work. While weak static and moderately intense laser-electric fields were employed to state-select and control the molecular targets in space, highly intense laser radiation was utilised to image molecular structure through strong-field ionisation. In the former case, the molecule’s response can be understood by looking at its static properties, which is described in subsections 2.1.1 and 2.1.2. For strong-field ionisation, however, one needs to employ a detailed, time-dependent description in order to grasp the dynamics of both bound and freed electrons, which is outlined in subsection 2.1.3.

A ubiquitous phenomenon, that follows the exposure to external electric fields, is the Stark effect. It gives rise to energy shifts of rotational, vibrational and electronic state manifolds and can lift degeneracies, reduce or increase the energy spacing between individual states. Perturbation theory offers a mathematical description of such energy shifts by means of a power-series expansion³¹:

$$E(\vec{\epsilon}) = E^{(0)} + \frac{\partial E}{\partial \epsilon_i} \epsilon^i + \frac{1}{2} \frac{\partial^2 E}{\partial \epsilon_i \partial \epsilon_j} \epsilon^i \epsilon^j + \frac{1}{6} \frac{\partial^3 E}{\partial \epsilon_i \partial \epsilon_j \partial \epsilon_k} \epsilon^i \epsilon^j \epsilon^k + \dots \quad (2.1)$$

This expression approximates the Stark-shifted energy E as a function of an external electric field $\vec{\epsilon}$. On the right-hand side the Einstein summation convention is employed, with the indices i, j, k, \dots each running through the Cartesian coordinates x, y, z . The partial derivatives in (2.1) are the negative electrostatic properties permanent dipole moment $\vec{\mu}$, static first polarisability α , static second polarisability β , and so on:

$$E(\vec{\epsilon}) = E^{(0)} - \mu_i \epsilon^i - \frac{1}{2} \alpha_{ij} \epsilon^i \epsilon^j - \frac{1}{6} \beta_{ijk} \epsilon^i \epsilon^j \epsilon^k - \dots \quad (2.2)$$

Usually, even for modelling strong-field ionisation, it is sufficient to know $\vec{\mu}$ and α to describe the departure from the field-free energy $E^{(0)}$ for a given molecular target.

2.1.1. Quantum-state selection and species separation

All experiments that are discussed in this thesis rely on the creation of cold and pure ensembles of molecules. After supersonic co-expansion one typically obtains sets of molecules in the vibrational and electronic ground state. Yet several rotational states might still be populated and many different

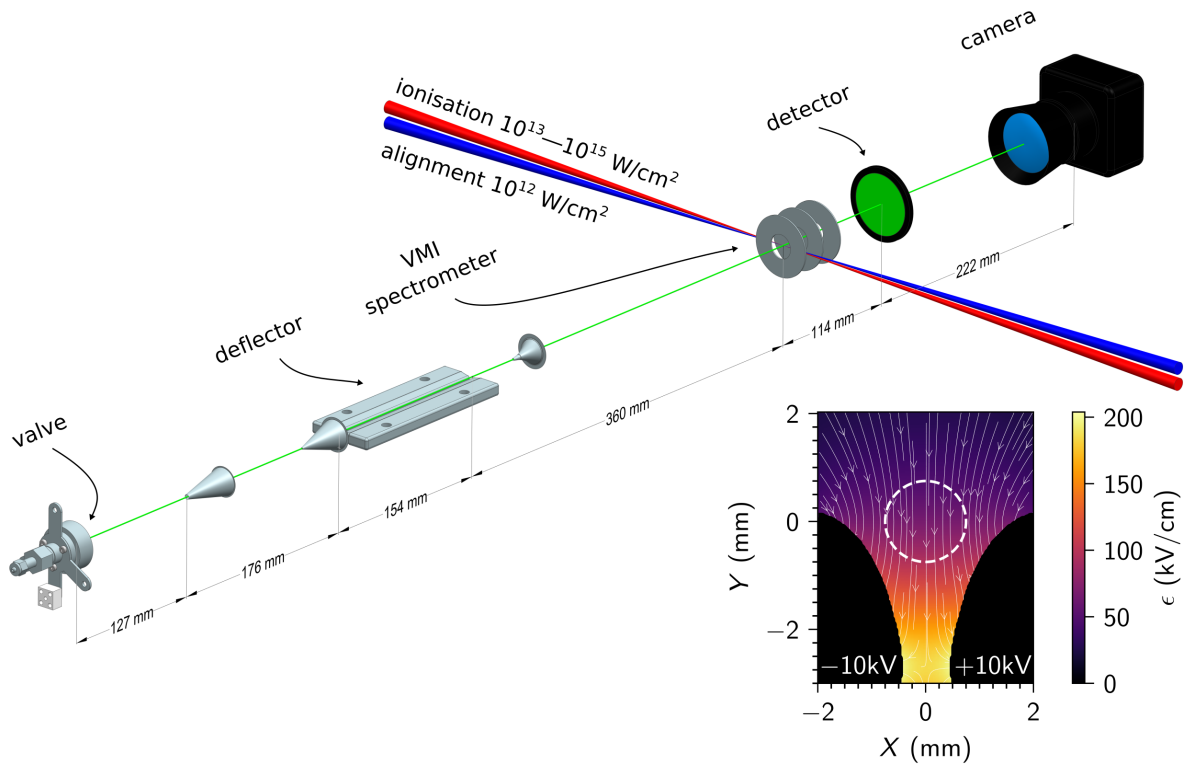


Figure 2.2.: Scheme of the experimental setup's essential components. A molecular beam is created by supersonic expansion, multiply skimmed, spatially dispersed through an electrostatic deflector and finally crossed by two collinear laser beams in the centre of a velocity-map imaging (VMI) spectrometer. Alignment of the molecules occurs at moderately high laser intensities, while very intense radiation is used for ionisation. The velocity vectors of the resulting charged particles are projected onto a position-sensitive detector that is imaged by a high-frame-rate camera. The inset in the lower right depicts a cross-section through the electric field within the deflector unit: The local field strength is colour-coded, the gradient of the electric field is illustrated by the white arrows and the dashed white circle displays the size of the molecular beam. The black-coloured regions correspond to two parallel electrodes, to which a voltage difference of 20 kV is applied. The resulting deflection is directed downwards, along the gradient of the electric field.

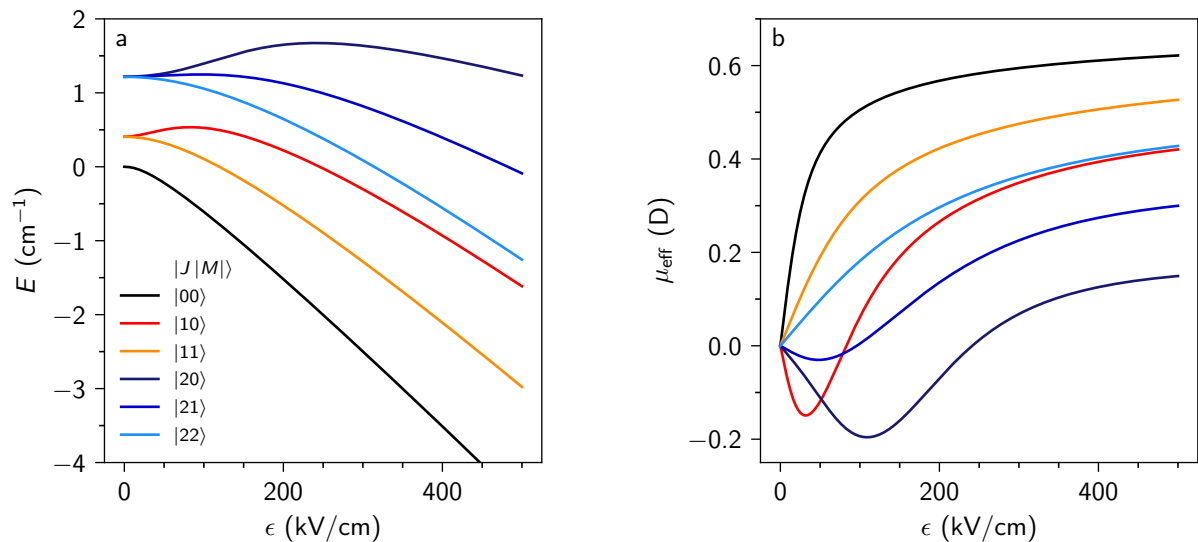


Figure 2.3.: a) Stark-shifted energies E and b) effective dipole moments μ_{eff} of the six lowest-lying rigid-rotor eigenstates of OCS as a function of the static electric field strength ϵ . This figure is a reproduction of Figure 2a in Chang *et al.*³². The corresponding calculations were conducted with the CMiStark Python package³².

conformers and clusters might be contained in the nascent gas jet. A further purification of the molecular beam in terms of rotational quantum states, conformations and cluster sizes can be achieved by exploiting the dc Stark effect. The underlying propagation through an inhomogeneous static electric field can be described in a time-independent manner, if the interaction with the field happens adiabatically³³. However, if the molecules experience an electric field, that changes too fast either in amplitude or direction, one needs to invoke a time-dependent description to deal with the resulting diabaticity^{34,35}.

Figure 2.2 shows a sketch of a typical experimental setup: After co-expansion of target and carrier through a pulsed Even-Lavie valve³⁶ the arising gas jet is skimmed multiple times in order to obtain a quasi-collimated molecular beam. Subsequently, the beam passes through an electrostatic deflector unit³⁷, which spatially disperses the different species within the molecular beam according to their individual effective-dipole-moment to mass ratios μ_{eff}/m . The inset in Figure 2.2 depicts a cross-section through the deflector's electric field, which is homogeneous along the horizontal but strongly inhomogeneous along the vertical axis. The deflecting force

$$\vec{F} = \mu_{\text{eff}}(\epsilon) \cdot \vec{\nabla}\epsilon, \quad (2.3)$$

which each molecular species experiences, is the product of its effective dipole moment and the local gradient of the electric field. μ_{eff} represents the projection of a molecule's permanent dipole moment onto the laboratory-fixed electric field axis and depends both on the exact rotational state and the electric field strength ϵ . It corresponds to the negative derivative of the energy with respect to the electric field strength, $\mu_{\text{eff}} = -\partial E/\partial\epsilon$. Figure 2.3 shows the Stark-shifted energies and effective dipole moments for the six lowest-energy rotational states of the OCS molecule. States with identical rotational quantum number J but different absolute magnetic quantum number $|M|$ lose their degeneracy in the presence of the external electric field, which can be appreciated in Figure 2.3a. As can be seen in Figure 2.3b, the average effective dipole moment, and therefore the degree of deflection, drops with increasing quantum numbers J . Since those molecules in the lowest rotational quantum states J undergo the largest deflection, they can be conveniently separated from their faster rotating neighbours, which benefits the degree of spatial fixation that can be achieved through laser alignment³². Furthermore, a difference in permanent dipole moment, which can be induced by a conformational change or the formation of a weakly bound cluster with another molecule, results in a different degree of deflection. Accordingly, one can also discriminate between species with respect to their conformation and their number of binding partners^{38–41}. An example for the latter is given in chapter 5, the spatial separation of indole and indole-H₂O.

2.1.2. Laser alignment

Molecules can be spatially controlled by exploiting their orientation-dependent Stark energies in the presence of intense external electric fields⁴². The potential created upon the laser field acting on the molecular system forces the molecule to change from a free rotational motion to a pendular motion that results in a certain degree of spatial confinement⁴³. Typical laser intensities are in the vicinity of 10^{12} W/cm², which corresponds to electric field strengths in the MV/cm regime, limited by the onset of unwanted multiphoton effects like electronic excitation or ionisation. Commonly used wavelengths are 800 and 1064 nm^{44–47}, because they are nonresonant with electronically excited states in most molecules and conveniently available at high pulse energies. In this optical to near-infrared regime, the approximate description is a second-order Stark shift, which varies as a function of the molecule's alignment in the polarisation-fixed frame of the irradiated laser field $\vec{\epsilon}$:

$$\Delta E(\vec{\epsilon}) = -\frac{1}{2}\alpha'_{ij}\epsilon^i\epsilon^j. \quad (2.4)$$

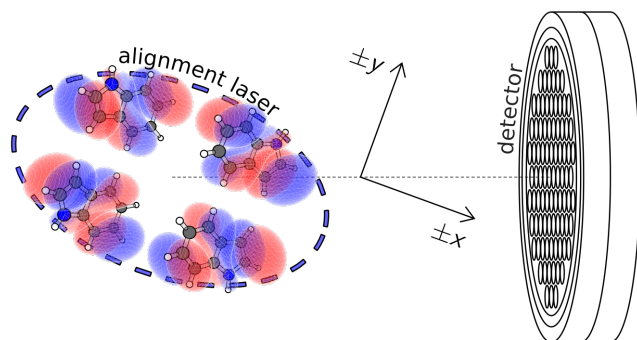


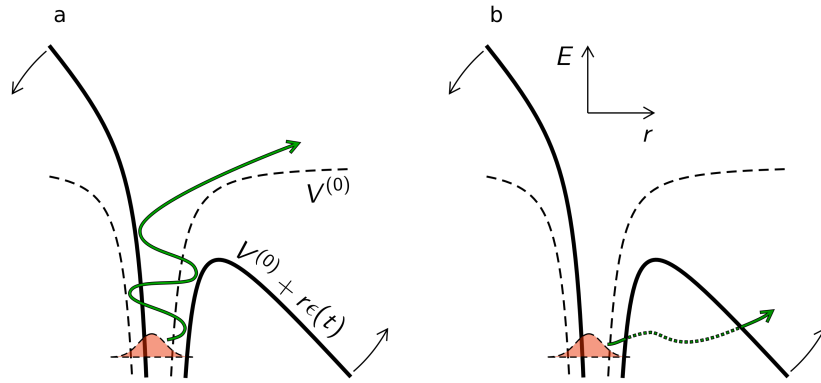
Figure 2.4: Indole molecules were fixed in the laboratory frame by irradiation with elliptically polarised laser pulses, sketched as blue ellipse. This enabled access to the molecule's principal-axes-of-polarisability frame. Isosurface representations of indole's HOMO are shown for all four coexisting orientations.

α' corresponds to the molecule's polarisability tensor in the polarisation-fixed frame of the aligning laser field. Note that the dipole term in (2.2) does not contribute to the Stark shift in (2.4). This is due to the instantaneous electric field $\vec{e}(t)$ changing on a much faster scale than the molecule could react to it by means of an energy-minimising rotation, i. e., reorientation of its permanent dipole⁴⁸. While the optical cycle at 800 nm spans roughly 2.7 femtoseconds (fs), rotational periods of molecules are in the picosecond (ps) to nanosecond (ns) domain. As a consequence, the molecule experiences an optical-cycle-averaged interaction with the laser field. Thus, the dipole term, which depends linearly on the electric field, vanishes, whereas the quadratic term (2.4) remains nonzero. This requires the molecular target to have an anisotropic polarisability in order to be alignable.

Another consequence of the quadratic electric-field dependence is that the time-averaged electric potential that is created by the laser possesses inversion symmetry. This results in the coexistence of degenerate spatial orientations, if the target molecule does not carry an inversion centre. Such behaviour is encountered, for example, when indole molecules undergo three-dimensional alignment in response to irradiation with elliptically polarised laser pulses. The molecule assumes one out of four minimum-energy orientations, which all have in common that the most and the second most polarisable axes of the molecule are aligned along the major and the minor axes of the polarisation ellipse. These four orientations, which are illustrated in Figure 2.4, are to be considered to coherently superimpose in a following imaging experiment⁴⁹. In this case one gains only restricted access to the molecule-fixed frame xyz , i. e., the principal-axes-of-polarisability frame, resulting from the signs of x and y axes not being determined through the polarisability interaction. Such orientation degeneracy can be lifted by the additional use of a static electric field^{15,50} or a second laser field with different colour⁵¹.

Fundamentally, the alignment process can be triggered in two limiting regimes: If all relevant time scales of the laser pulse envelope are much longer than the molecule's rotational period τ_{rot} , the alignment occurs adiabatically. A short laser pulse, however, interacts diabatically with the target and creates a wavepacket of rotational states that undergoes alignment revivals at certain multiples of τ_{rot} after the kick pulse⁵². By employing two carefully timed kick pulses, one can achieve very high degrees of alignment under laser-field-free conditions⁵³. However, these approaches are mostly restricted to symmetric-top molecules, because the occurrence of alignment revivals requires the commensurability of energy levels across the rotational degrees of freedom. Thus, for an asymmetric-top rotor like indole it is advisable to follow the adiabatic route to align the molecule, as it was done exclusively in the studies that are discussed in this thesis. Also for this adiabatic alignment scheme there is the opportunity to obtain aligned molecules under laser-field-free conditions. This can be achieved by a slow, quasi-adiabatic turn on of the alignment field followed by a sudden truncation that leaves the target strongly aligned for a small fraction of its rotational period^{54,55}.

Figure 2.5: Sketch of the two archetypical strong-field ionisation pathways: a) vertical ionisation through the classically allowed region and b) tunnelling through the moving barrier. A simplified atomic binding potential $V^{(0)}$ is shown that is deformed by a time-dependent laser-electric potential $r\epsilon(t)$. This illustration is inspired by Ivanov *et al.*⁵⁶.



2.1.3. Strong-field ionisation

Strong-field ionisation refers to the extraction of electrons from either atoms or molecules through irradiation of a very intense electric field, typically provided by laser pulses with intensities $\geq 10^{13}$ W/cm². The ionisation process is widely independent of the target and the exact central wavelength of the laser radiation and predominantly affects the most loosely bound electrons in the highest occupied states. It forms the first step of many compelling strong-field phenomena that allow to closely observe molecules on their natural time and position scales¹⁸, making it an ideal instrument for molecule imaging.

The driving force for ionisation is the severe periodic deformation of the target's binding potential by the strong laser-electric field. In the strong-field regime, there are two coexisting mechanisms that can release a bound electron into the continuum: by multiply rebounding off the laser-shaken potential walls, referred to as strong-field multiphoton ionisation, or *via* tunnelling through the moving barrier that results from the deformation exerted by the external field⁵⁶. Both mechanisms are schematically sketched in Figure 2.5 for an atomic target. The multiphoton path leads vertically through the classically allowed region, i. e., staying within the potential walls, into the continuum. In this scenario, the electron density of the atom cannot instantaneously adapt to the fast rocking potential well. As a consequence, it is periodically bounced back and forth between the walls, heating up until a certain portion has gained enough energy to escape. Along the tunnelling pathway, however, an electron is diving through the potential barrier, which represents a purely nonclassical process. Also in this case the moving barrier can significantly alter the ionisation process and, thus, the properties of the freed photoelectron when it appears in the continuum. While multiphoton ionisation gains importance for increasing laser frequencies ω , the tunnelling channel predominates at high field strengths. Keldysh ascribed this interplay between the two archetypical pathways to the ratio of laser cycle $1/\omega$ and tunnelling time τ ⁵⁷. He introduced an adiabaticity parameter

$$\gamma = \omega \cdot \tau = \frac{\omega \cdot \sqrt{2I_p}}{\epsilon}, \quad (2.5)$$

which classifies strong-field ionisation to be multiphoton dominated for $\gamma \gg 1$ and ruled by tunnelling for $\gamma \ll 1$. The tunnelling time in this simplified description is just proportional to the height of the barrier $\sqrt{2I_p}/\epsilon$, which depends on the system's ionisation potential I_p and the field strength.

Let us now take a brief look at the theoretical description of strong-field ionisation and the two most prominent approaches that make the majority of models feasible at all: the strong-field approximation (SFA) and the semiclassical approximation (SCA). In order to rigorously describe a dynamical quantum-mechanical process like strong-field ionisation one needs to invoke the time-dependent Schrödinger equation (TDSE),

$$i \frac{\partial |\psi\rangle}{\partial t} = \hat{H}(t) |\psi\rangle, \quad (2.6)$$

which relates the Hamilton operator \hat{H} to the time-derivative of the wavefunction $|\psi\rangle$. It's formal solution is

$$|\psi(t)\rangle = e^{-i \int_{t_i}^t \hat{H}(t') dt'} |\psi_i\rangle = \hat{U}(t_i, t) |\psi_i\rangle. \quad (2.7)$$

The exponential operator $\hat{U}(t_i, t)$ is called a propagator and promotes the initial wavefunction $|\psi_i\rangle$ at time t_i until a desired point in time t . The rigorous evaluation of \hat{U} is extremely tedious already for atomic systems⁵⁸. In most cases, especially for tackling molecules, it is therefore indispensable to resort to a simplified description of \hat{U} in one way or another. That is where the SFA and the SCA come into play. But before we look into the ideas behind those two approximations, let us consider what is actually observed in a strong-field-ionisation experiment. In the focus of this thesis is the imaging of molecular structure by inspection of the momentum distribution of the freed photoelectron. So far we have just looked at the propagation from one bound state to another, in (2.7). But the photoelectron that is eventually detected is in a continuum state with an asymptotic momentum \vec{p}_∞ . Commonly, the path from the initial bound state to the final, detectable state is divided into two steps: (i) the actual transition into the continuum and (ii) the subsequent motion in the continuum, which is driven by both the laser and the ionic potential. For a single active electron the transition amplitude $a(\vec{p}, t)$ for step (i) can be expressed by means of the strong-field S-matrix⁵⁸:

$$a(\vec{p}, t) = -i \int_{t_i}^t \langle \vec{p} | e^{-i \int_{t'}^t \hat{H} dt''} \hat{V}_L e^{i I_p^{(0)}(t'-t_i)} |\psi_i\rangle dt'. \quad (2.8)$$

The integrand of (2.8) can be understood as follows (read from right to left): One starts with a field-free initial state $|\psi_i\rangle$ at time t_i that has an energy of $-I_p^{(0)}$. $|\psi_i\rangle$ evolves under field-free conditions until t' , which is grasped by the field-free propagator $\exp[i I_p^{(0)}(t' - t_i)]$. At t' the potential of the laser $\hat{V}_L(t')$ kicks in, followed by a propagation through the full propagator \hat{U} . Finally, the wavefunction is projected onto a continuum state with instantaneous momentum \vec{p} . The total transition amplitude is then obtained by integrating over all possible ionisation times t' between t_i and t . Although (2.8) does not look very inviting, it is still exact and represents the starting point for many physical approximations^{56,58}.

The SFA for instance assumes a simplified Hamilton operator \hat{H}_V that only includes the electron's kinetic energy and the laser potential, i. e., it completely neglects the ionic potential. The resulting propagator $\exp[-i \int_{t'}^t \hat{H}_V dt'']$ corresponds to the motion of a free electron in the laser field. It is called Volkov propagator and is known exactly⁵⁸. The SCA, however, employs another approach to make \hat{U} more tractable, i. e., by substituting

$$-i \int_{t'}^t \hat{H} dt'' \rightarrow iS(t', t). \quad (2.9)$$

S is the classical action that the electron picks up between t' and t . This substitution is based on Feynman's path integral formulation and forms the basis for semiclassical propagators. Using both SFA and SCA for the description of tunnelling ionisation from an atom, there were two closely related models formulated that provide elegant analytical expressions for the phase-space properties of the photoelectron when it is born in the continuum: the Ammosov-Delone-Krainov (ADK)⁵⁹ and the Perelomov-Popov-Terentev (PPT) theory⁶⁰. In this thesis, the ADK framework is utilised to model the tunnel ionisation of the indole molecule, considering the increased level of complexity that is imprinted onto the nascent photoelectron compared to the atomic case.

The post-ionisation motion of the electron in the continuum is dominated by the laser potential and is known to be rather classical⁶¹. This enables a straightforward computation of its time-dependent position and momentum by evaluation of the equations of motion, and permits the description of its phase through the Coulomb-corrected SFA⁶² or time-dependent semiclassical propagators⁶³. The latter approach is employed in this thesis, see chapter 6.

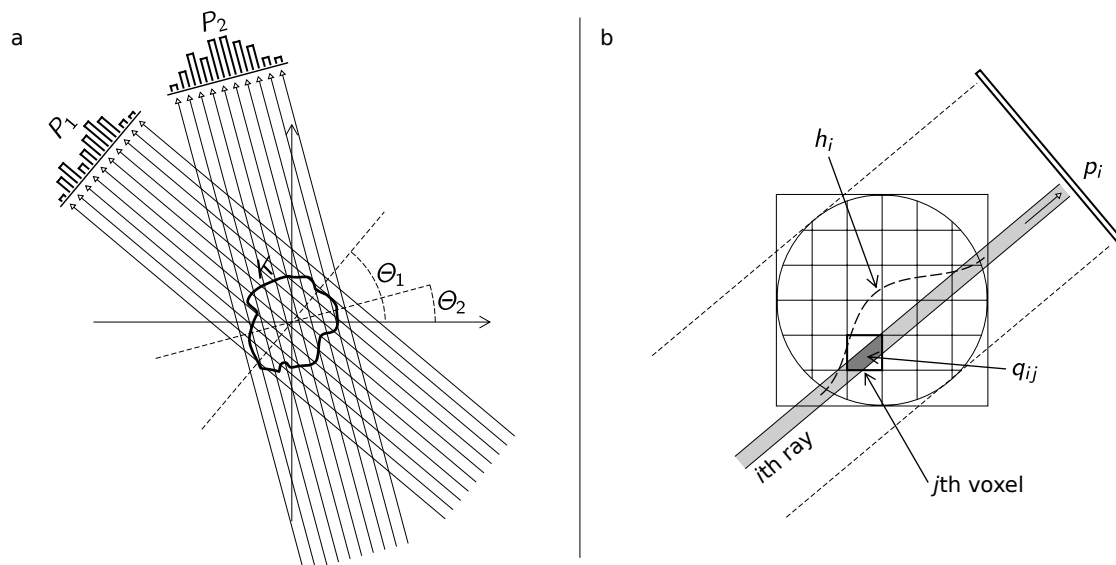


Figure 2.6.: a) The principle of tomographic imaging. By measuring multiple projections of an object from different perspectives one gets access to the object in its full extent. The image illustrates the recording of two parallel-ray projections P_i that image an object K . Each individually recorded ray corresponds to a unique line integral through K . b) Schematic view of the volume cross-section q_{ij} between the i th projection ray and the j th voxel of the object basis. The total integral of the i th cuboid ray through the entire voxel basis is compared to the recorded pixel value p_i . Application of the Hamming window h_i emphasises the central voxels within the cylindrical object space during the iterative reconstruction procedure. These illustrations are inspired by Kak and Slaney⁶⁴.

2.2. Imaging techniques

This section gives a short description of imaging and related techniques that were either directly employed during my doctoral work or that are frequently referred to in the main part of this thesis.

2.2.1. Tomographic imaging

Our world is three-dimensional. But acquiring a usual image of any three-dimensional object, like taking a photograph, reduces the recorded information to two dimensions. The most straightforward and probably also the most intuitive way to circumvent this issue is through tomographic imaging⁶⁴. Instead of recording just a single projection of the object of interest, one looks at it from many different perspectives. The simplest case, the projection along bundles of parallel rays, is sketched in Figure 2.6a.

The three-dimensional resolution that can be achieved through tomographic imaging depends both on the camera resolution and the number of available projections⁶⁴. Thus, it is advisable to sample as many tomographic angles Θ as possible while ensuring that all individual images possess a reasonable quality. Θ describes the angle between the two-dimensional detector and the object's coordinate system. Ideally, it should be sampled throughout the full angular range $0^\circ \leq \Theta < 180^\circ$ to obtain the best possible results. In medical x-ray imaging the realisation of different tomographic angles is achieved by rotating the detector around the patient, because he or she might be in a state that forbids any severe motion. Molecules, however, do not mind being turned from one orientation to another. Accordingly, in this doctoral work tomographic molecular imaging was realised by rotating the molecules with respect to the detector. This was achieved through rotation of the alignment laser's polarisation ellipse with a half-wave plate.

Now let us have a look at how to retrieve the original three-dimensional object from all available

projections. Each ray that hits the detector plane represents a line integral through the object. But since camera detectors usually consist of discretised pixel arrays, the actually recorded information corresponds to partial integrals through the object within cuboid volumes that sit on the individual square pixels. Each of these cuboid rays has a unique position within the object space. In this doctoral work, an algebraic reconstruction technique⁶⁴ was utilised that iteratively built the desired objects in a Cartesian voxel basis. The essence of this method is the modelling of forward and backward projection, which establishes the connection between object space and the recorded projections. For this it is crucial to know the volume cross-sections between all rays and all voxels. Figure 2.6b illustrates this relation by displaying a side view onto the effective cylindrical object volume that is mutually illuminated by all projections.

In the following, the applied custom reconstruction algorithm is described that was tailored to reliably tackle tomographic imaging of objects that span many orders of magnitude in density. Although the exact calculation of all cross-sections q_{ij} employs just simple geometry, it represents a rather cumbersome task that results in a huge amount of data even for moderate numbers of pixels. In this work, the number of voxels within the effective cylindrical reconstruction volume was chosen to equal half the total number of rays. Accordingly, for the acquisition of $N_{\text{pro}} = 90$ projections with each $N_{\text{pix}} = 10^6$ pixels one has to deal with $N_{\text{ray}} = N_{\text{pro}}N_{\text{pix}} = 9 \times 10^7$ rays that intersect with $N_{\text{vox}} = 4.5 \times 10^7$ voxels. All nonzero cross-sections q_{ij} were computed once and stored as a basis set for the subsequent reconstruction procedure. In principle, one could obtain the best match of voxel values to all recorded projections through matrix inversion. But the size of the resulting cross-section matrix makes such an approach difficult. For this reason an iterative reconstruction procedure was employed.

The reconstruction started with all voxel values $v_j^{(0)}$ being 0. One iteration corresponded to applying all recorded projections exactly once in order to improve the current object. Within one iteration the projections were ordered such that the differences between consecutive tomographic angles Θ were roughly 90° . Within one projection the following steps were made:

- (i) For each ray the cuboid sum c_i through the current object was evaluated by summing over all voxel values $v_j^{(k)}$:

$$c_i^{(k)} = \sum_j q_{ij} v_j^{(k)}. \quad (2.10)$$

The indices i , j and k refer to rays, voxels and iterations. The index for the current projection is omitted for the sake of brevity.

- (ii) The preliminary changes to all intersected voxels were computed by comparison with the pixel value p_i :

$$\Delta v_{ij}^{(k)} = \frac{(p_i - c_i^{(k)}) q_{ij}}{\sum_j q_{ij}}. \quad (2.11)$$

- (iii) Subsequently, the preliminary new voxel values $v_j^{(k+1)} = v_j^{(k)} + \Delta v_{ij}^{(k)}$ for the i th ray were calculated. At this point, the algorithm exploited the nonnegativity of the imaged objects. If necessary, the $\Delta v_{ij}^{(k)}$ values were redistributed along the i th ray to assure $v_j^{(k+1)} \geq 0$ for all voxels affected.
- (iv) After evaluation of all rays, the voxel-wise mean changes were computed:

$$\Delta v_j^{(k)} = \frac{\sum_i h_{ij} q_{ij} \Delta v_{ij}^{(k)}}{\sum_i q_{ij}}. \quad (2.12)$$

h_{ij} corresponds to a Hamming window that attenuated the voxel changes towards the periphery of the cylindrical reconstruction volume. This measure relies on the assumption, that the object is more dense towards the centre of the reconstruction volume, and gives rise to an increased convergence rate.

(v) Eventually, the new voxel values,

$$v_j^{(k+1)} = v_j^{(k)} + \lambda \Delta v_j^{(k)}, \quad (2.13)$$

were obtained using a relaxation parameter $0 < \lambda \leq 1$. Conducting such a relaxed optimisation enables the retrieval of the best matching object even for sets of low-statistics projections. This effect relies on the fact that the maximum-likelihood solution grows in faster with proceeding iterations compared to the appearance of three-dimensional Poissonian noise⁶⁴. The lower λ , the further separated are these two components as a function of the iteration number, at the cost of a decreased convergence rate. All three-dimensional distributions shown in this thesis were found through reconstruction procedures with $\lambda = 0.05$ that converged for $k < 15$.

2.2.2. Coulomb-explosion imaging

A common and effective method to image and measure molecular alignment and orientation is through Coulomb-explosion imaging (CEI). It relies on multiple ionisation of the target molecule, followed by a rapid disintegration into several ionic fragments that is driven by Coulomb repulsion between the positive charges. The removal of several electrons can be achieved, for instance, through irradiation with intense infrared light^{53,65,66} or high-photon-energy radiation from free-electron lasers^{44,66,67}, or by passing the molecules through a thin stripping foil⁶⁸. Since individual ionic fragments from the same species can carry different kinds of information, it is crucial to record and inspect them separately. Such separation by means of the fragments' mass/charge ratios is readily achieved by exploiting their different times of flight within the velocity-map imaging spectrometer. If at least one of the observable break-up channels follows axial recoil, one can quantify the degree of alignment. Yet this is only the case for linear rotors^{53,65} or molecules that contain heavy-atom markers^{44,66,69}. For asymmetric-top molecules without such marker substituents, like indole, the theoretical modelling of both the alignment process and the fragmentation is still needed in order to assess the degree of alignment in experiment⁵⁵.

Figure 2.7 depicts slices through the tomographically reconstructed ion-velocity distributions of three different ionic fragments that followed the Coulomb explosion of three-dimensionally aligned indole molecules. The molecules were quasi-adiabatically laser-aligned at a peak intensity of 10^{12} W/cm² with 3:1 elliptically polarised pulses with a saw-tooth temporal shape and a rise time of 500 ps. Coulomb explosion was triggered by irradiation with circularly polarised 800-nm pulses at a peak intensity of 2.1×10^{14} W/cm². Both laser beams were polarised in the same plane.

The case of indole already demonstrates the difficulties that arise, if one aims at the observation and characterisation of a complex (bio-)molecule's degree of alignment. The sixteen atoms that form the indole molecule constitute only three different chemical elements. Although the nitrogen atom is unique in the molecule scaffold, it is strongly bound within an aromatic five-membered ring and is not located on any of the molecule's principal axes of polarisability. Even though the out-of-plane alignment is clearly visible for all three ions in the top row of Figure 2.7, the degree of in-plane alignment is a lot harder to estimate from the bottom-row velocity slices. The H⁺ distribution is almost isotropic in the molecular plane, except for a very shallow maximum along the molecule-fixed x axis. For the C²⁺ fragment the situation is just slightly better: Its in-plane velocity distribution appears to consist of two components, one that is isotropic in the plane and another one that exhibits a clear maximum along the x axis. Yet it is the most meaningful of all observed fragments. The two rings in the CH_{*n*}N⁺ ions' in-plane distribution carry an angularly broad

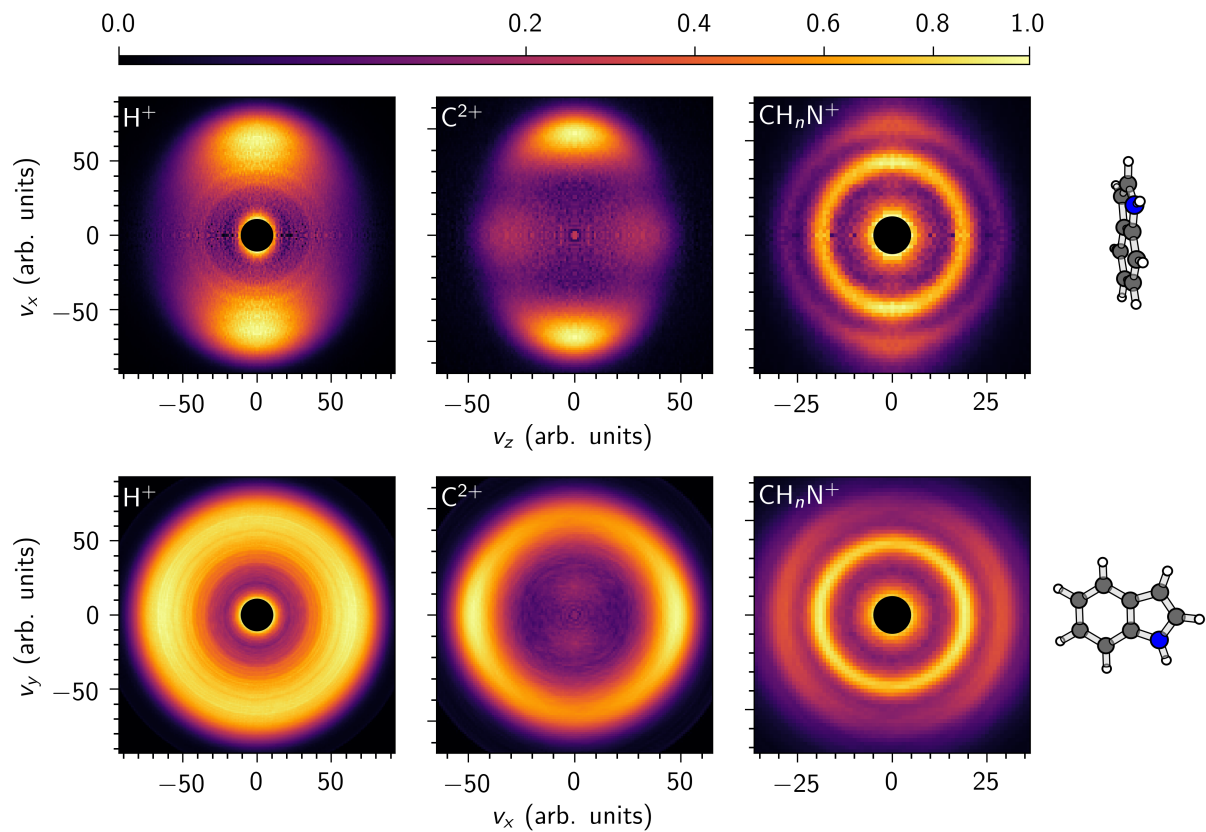
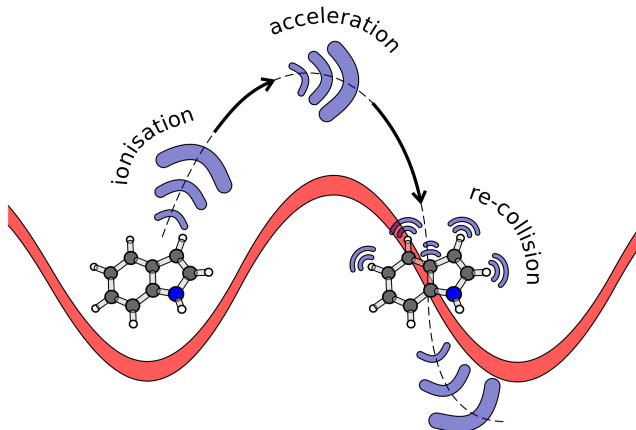


Figure 2.7.: Slices through the three-dimensional velocity distributions of the H^+ , C^{2+} and CH_nN^+ ($n = 0, 1, 2$) fragments are shown that followed the Coulomb explosion of aligned indole molecules. Each ion distribution is depicted on two orthogonal planes, at $v_y = 0$ in the top row at and $v_z = 0$ in the bottom row. The cut out, intense contributions in the centres of the H^+ and CH_nN^+ ion slices occur only in the presence of the alignment laser. They are a result of the alignment laser destroying “hot” singly charged indole parent ions that were previously created by the probe laser. The ball-and-stick models of the molecule on the right illustrate the slices’ positions in the molecular frame. For the sake of simplicity only one out of four coexisting orientations is shown.

Figure 2.8: Sketch of laser-induced electron diffraction. Strong-field ionisation at a peak of the linearly polarised laser-electric field releases a photoelectron into the continuum, accelerates it to high energy and steers it back to the molecule. A small portion of the returning electron wave elastically scatters off the molecule, probing the instantaneous interatomic distances at the moment of recollision. The laser-electric field is sketched in red and the photoelectron wave is shown in light blue.



maximum along that same axis, which could be due to the main recoil direction being between x and y axis. Those rather limited and only qualitative views on the molecule's in-plane alignment are a result of a highly nonaxial many-body fragmentation process that follows the bicyclic structure of indole. For this reason the full three-dimensional degree of alignment $\langle \cos^2 \delta \rangle \approx 0.9$ ⁷⁰ could only be estimated in conjunction with simulations that considered both the alignment dynamics of the neutral molecule and the subsequent Coulomb explosion of the multiply charged parent ion⁵⁵.

2.2.3. Laser-induced electron diffraction

Laser-induced electron diffraction (LIED) is a method that allows for the determination of interatomic distances on femtosecond timescales^{71,72}. It relies on strong-field ionisation in linearly polarised laser-electric fields and constitutes three fundamental steps: First, an electron is ejected into the continuum through strong-field ionisation from the highest occupied molecular orbital(s) of the target molecule. Subsequently, the nascent photoelectron is tossed back at the molecular ion by the laser field. Upon recollision, the electron may elastically scatter off the molecule, interrogating the instantaneous positions of the nuclei. The process is schematically depicted in Figure 2.8. The maximum photoelectron kinetic energy at recollision is roughly three times the ponderomotive potential U_p ⁷³, with

$$U_p = \left(\frac{\epsilon_0}{2\omega} \right)^2. \quad (2.14)$$

Thus, by either increasing the peak electric field strength ϵ_0 or decreasing the circular frequency ω of the laser one can achieve high kinetic energies and therefore small de Broglie wavelengths λ_{dB} of the returning electron. At a photoelectron kinetic energy of 150 eV λ_{dB} is 10^{-10} m, representing a resolving power that reaches common interatomic distances^{19,74}. Since the maximum usable value of ϵ_0 is limited by the onset of double ionisation of the target, LIED experiments need to be conducted with low-frequency, that is mid-infrared, radiation.

If recollision occurs at the earliest possible instant, after roughly 3/4 of an optical cycle, the diffraction pattern gets encoded in the maximum-kinetic-energy contribution of the asymptotic wavepacket and can be easily separated from the rest. Scattering contributions from later revisits of the ion, however, result in larger time spans between ionisation and recollision, and thus carry less concise temporal information⁷⁵. Both the probability for recollision at first revisit and the complexity of the returning electron wave, which influences the possibility to extract meaningful molecular structure, depend on the target itself and the exact ionisation mechanism that extracted the photoelectron in the first place. These aspects will be illuminated and further discussed in the main part of this thesis, in chapters 4, 6 and 7.

3 Strong-field photoelectron imaging at finely resolved incident intensities¹

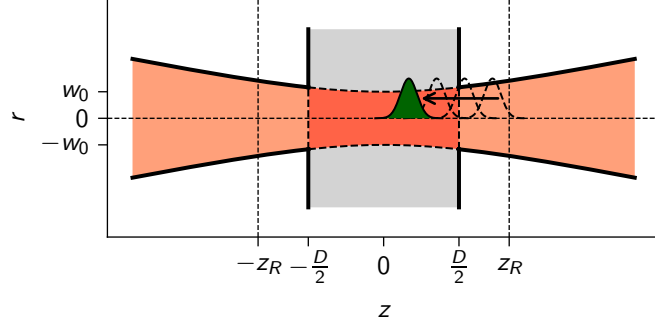
3.1. Introduction

Studies in strong-field physics aim at the understanding and control of the electron wave packet emitted by an atomic or molecular target following the exposure to intense radiation. Vast theoretical and experimental efforts are focused on, e. g., the determination of intensity-dependent ionisation probabilities^{76,77} and cut-off energies for direct and rescattered electrons⁷⁷, the recognition of Freeman resonances^{78–80}, the observation of channel-switching and -closing effects^{81,82}, and the analysis of the photoelectron orbital angular momentum^{80,82} in the multiphoton regime as well as the imaging of the initial state's electron density distribution^{15,83,84}. In general for strong-field ionisation, the electron wave packet's initial distribution in phase space – and thereby its subsequent dynamics in the field – is strongly shaped by the intensity of the electric field⁵⁶. Within the framework of multiphoton ionisation the intensity-dependent ac Stark shift alters the energies of initial and final target states as well as of any intermediate state that is resonantly passed through. In addition, the continuum the electron is born into is raised by the intensity-dependent ponderomotive energy. From the perspective of tunnelling ionisation, the intensity dictates the shape of the potential barrier to be traversed in order to reach the continuum⁵⁹. As a result, the outgoing electron wave packet is substantially dependent not only on the target system, but also on the intensity of the driving field.

Resolving the incident intensity in a strong-field experiment is as fundamental as knowing the incident photon energy in optical spectroscopy. Especially for the comparison of experimental data with predictions from strong-field ionisation models intensity selectivity is highly beneficial, since intensity integration does not blur the results. However, in experimental investigations employing typical laser-focus geometries the recorded target response results from intensities ranging from 0 to the peak intensity. As a consequence, the target information encoded in the experimental observables is often highly obscured by integration over all incident intensities. Various schemes were reported that allow the investigator to overcome this issue and enable access to the target response in an intensity-resolved fashion. An intensity-selective scanning method, which relies on the extraction of charged particles created within a restricted slice of the longitudinal intensity distribution – implemented through an aperture – in conjunction with an intensity deconvolution step in post-processing, was introduced⁸⁵ and later further refined⁷⁷. For continuous-wave laser beams the acquisition of intensity-difference spectra was described⁸⁶. The approach proposed is based on the evaluation of the derivative of the target response with respect to the peak intensity. Through analytical inversion by means of a power-series expansion in intensity, namely multiphoton expansion technique, the retrieval of distinct-intensity responses from a set of intensity-averaged measurements at different peak intensities was demonstrated⁸⁷. While the intensity-selective scanning and the multiphoton expansion technique employ rather complex post-processing, they essentially eliminate the effect of focal intensity averaging, depending on the peak-intensity step size of the data set. Although through the acquisition of intensity-difference spectra, using the most common focus

¹This chapter is based on the publication J. Wiese, J.-F. Olivieri, A. Trabattoni, S. Trippel, and J. Küpper, “Strong-field photoelectron momentum imaging of OCS at finely resolved incident intensities,” *New. J. Phys.* **21**, 083011 (2019). I contributed to this work by setting up the experiment together with A. T. and S. T. as well as by formulating the presented description of the laser–target interaction and analysing the experimental data by myself. Moreover, I interpreted the data and wrote the manuscript.

Figure 3.1: Schematic view of the focal geometry: The laser beam (orange) intersects the gas-target beam (gray), which is assumed to possess a uniform density distribution. If the diameter of the gas-target beam, D , is smaller than twice the Rayleigh length of the focus, z_R , the effective focal volume can be approximately described with a constant radial standard deviation, $\sigma_r = w_0/2$. The spatial equivalent of the laser pulse's temporal distribution for a distinct time is a Gaussian profile (green). Since neither the longitudinal nor the radial intensity distribution change upon the pulse's passage through the effective focal volume, the whole space- and time-integrated laser-target interaction can be described by a spheroidal intensity function, see (3.1).



geometry, the impact of intensity averaging is only highly suppressed yet not completely removed, it represents the by far simplest approach of the three.

In this manuscript, the advantages of intensity-difference spectra are studied for pulsed laser beams and utilised to investigate the intensity-dependent photoelectron momentum distributions from strong-field ionisation of carbonyl sulfide (OCS) molecules in the intermediate regime between multiphoton and tunnelling ionization.

3.2. Intensity-difference signals

The differential volume occupied by a distinct intensity in a continuous-wave laser beam can be readily described⁸⁶. This focal intensity distribution is referred to as one implementation of a 2D configuration. In the following, the corresponding case of a pulsed laser beam will be investigated.

The intensity profile of an effective laser focus in a typical gas-phase experiment is assumed to have the following geometric properties: In space it is rotation-symmetric about the wave vector and its distribution along the propagation direction is given by a rectangular function with the width of the diameter of the skimmed gas-target beam D , relying on D to be smaller than twice the focus's Rayleigh length z_R . Figure 3.1 provides a schematic illustration of the focus geometry. The transverse spatial and the temporal profile follow normal distributions with standard deviations σ_r and σ_t . For a distinct time during the laser pulse's propagation through the focus volume the three-dimensional intensity distribution can be written as

$$I = I_0 \cdot \exp\left(-\frac{r^2}{2\sigma_r^2}\right) \cdot \exp\left(-\frac{z^2}{2\sigma_z^2}\right). \quad (3.1)$$

Here, I_0 is the temporal peak intensity and $\sigma_z = c\sigma_t$ is the spatial equivalent of the temporal standard deviation σ_t . If $D \gg \sigma_z$, the full intensity spectrum, i. e., for all possible longitudinal positions of the pulse, will be quasiproportional to the intensity spectrum at a single position far away from the longitudinal borders given by the edges of the gas-target beam. Thus, the intensity distribution displayed above can be used to deduce the intensity spectrum of the complete space- and time-integrated focus interaction. In the following, a focus with such an intensity distribution is referred to as 3D configuration. After rearrangement of (3.1) to

$$\frac{r^2}{\sigma_r^2} + \frac{z^2}{\sigma_z^2} = 2 \ln \frac{I_0}{I} \quad (3.2)$$

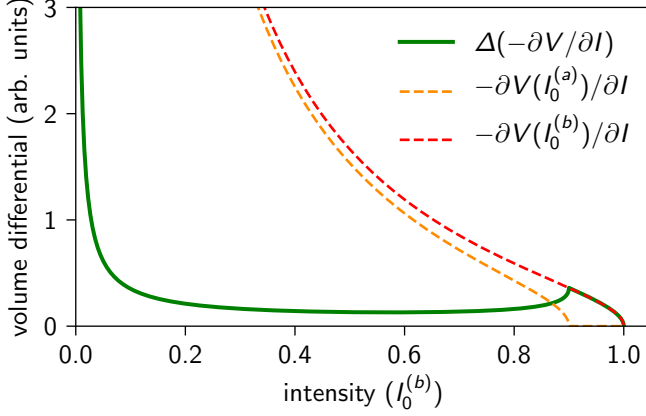


Figure 3.2: Intensity-dependent volume differentials for a space- and time-integrated laser-target interaction in a 3D configuration for two peak intensities $I_0^{(a)}/I_0^{(b)} = 0.9$ (dashed lines). The difference between the two volume differentials (solid line) exhibits highly suppressed intensity contributions for $I < I_0^{(a)}$.

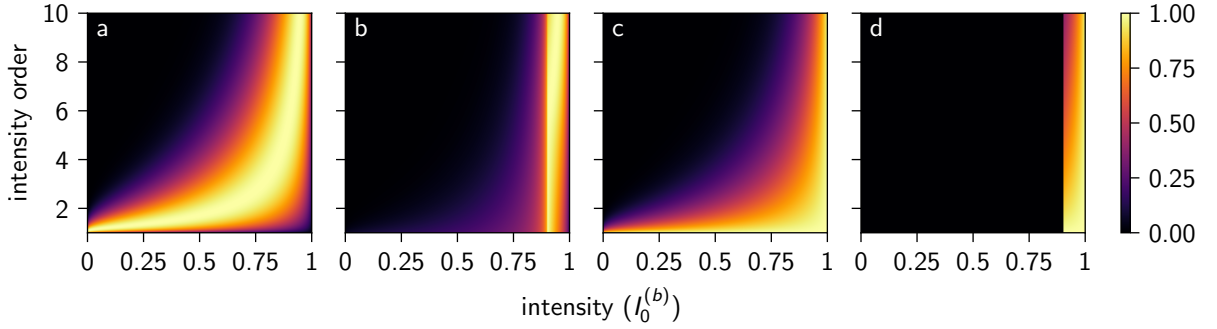


Figure 3.3.: Normalised signals as a function of intensity and intensity order n for different volume differentials: a) full volume in 3D configuration, b) differential volume in 3D configuration, c) full volume in 2D configuration, d) differential volume in 2D configuration. These provide a measure for the relative contribution of a distinct intensity to an overall signal, that scales with intensity to the power of a fixed exponent. For the differential-volume signals a ratio of $Q = I_0^{(a)}/I_0^{(b)} = 0.9$ was used, which represents the lowest Q value employed in experiment. All signal maps depicted were row-wise normalised to their maxima. For the 2D configuration case the volume differential follows $-\partial V_{2D}/\partial I \propto -1/I^{86}$.

it is obvious that points of equal intensity are located on the surface of a spheroid. Accordingly, the volume function is

$$V_{3D}(I) = \frac{4\pi}{3} \sigma_r^2 \sigma_z \left(2 \ln \frac{I_0}{I} \right)^{3/2} \quad (3.3)$$

with the differential volume $-(\partial V_{3D}/\partial I) dI$ that is occupied by the isointensity shell dI around I following

$$-\frac{\partial V_{3D}}{\partial I} dI \propto \frac{\sqrt{\ln \frac{I_0}{I}}}{I} dI. \quad (3.4)$$

This provides a measure for the weight of any intensity between 0 and I_0 in the laser-target interaction. It complements the previous elaborations⁸⁶ by the additional consideration of the laser pulse's temporal intensity profile. Note that the description of the volume function V_{3D} will only be as simple as (3.3) if the radial intensity distribution is independent of z , i. e., $D < 2z_R$.

Figure 3.2 shows the resulting intensity spectra for two peak intensities $I_0^{(a)}/I_0^{(b)} = 0.9$ along with the corresponding difference spectrum. Evidently, in the difference spectrum the contributions from intensities $< I_0^{(a)}$ are highly suppressed, albeit not completely eliminated. The pole point at $I = 0$ does not affect the determination of any intensity-dependent quantity, because the corresponding signal scales with $\Delta(-\partial V_{3D}/\partial I) \cdot I^n$, $n > 0$. Here, n would be an integer for a pure single-channel multiphoton process but does rather represent an intensity-dependent quantity for a realistic strong-field interaction. The full-volume and exemplary difference signals are shown in Figure 3.3 for

Figure 3.4: Mean intensity as a function of the intensity order n for different intensity-difference signals with peak-intensity ratios $Q = I_0^{(a)}/I_0^{(b)}$ for the 3D (solid lines) and 2D configurations (dashed lines). The black lines correspond to signals at full volume integration, $Q = 0$, i. e., evaluated at a single peak intensity. Q values of 0.9 and 0.99 represent the lower and upper limits of peak-intensity ratios used in our experiments, *vide infra*.

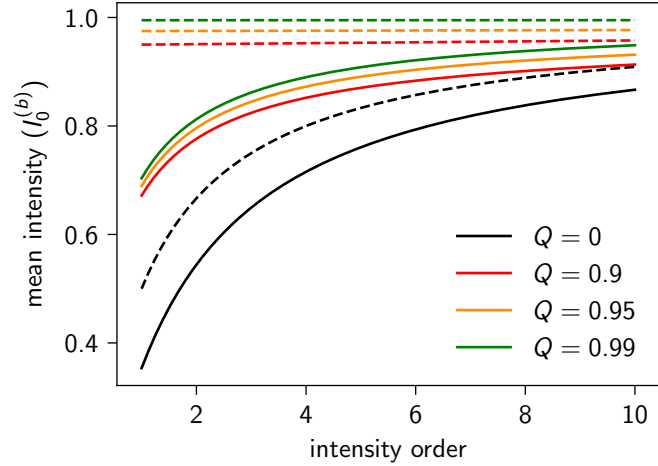
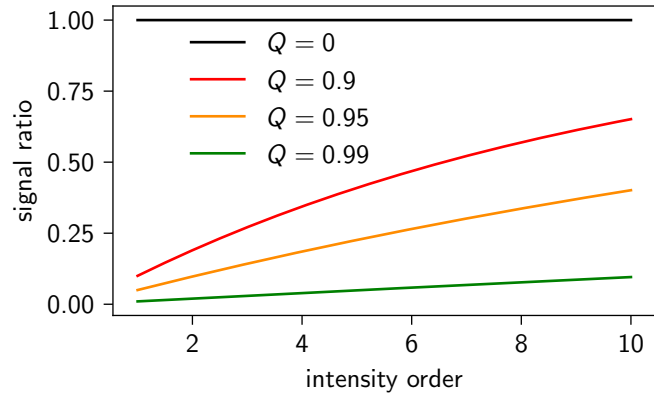


Figure 3.5: Fraction of the intensity-difference signal of the overall signal at peak intensity. 2D and 3D configuration show identical behaviour.



both, the 2D and the 3D configuration, as a function of intensity and intensity order n . Note that for a focal interaction with intensities normally distributed only along two dimensions (2D configuration), i. e., either a spatial laser sheet with a Gaussian temporal profile or a two-dimensional spatial profile with a flat-top temporal profile, the corresponding intensity-difference spectrum carries nonzero contributions only for $I_0^{(a)} \leq I < I_0^{(b)}$. Figure 3.4 displays the mean intensities for various intensity-difference signals in dependence of the intensity order. In general, the use of a 2D focus configuration gives rise to mean intensities that are closer to the peak intensity compared to the 3D case. The black lines illustrate the change of the mean intensity with increasing intensity order for measurements at a single peak intensity. Especially for low intensity orders the corresponding mean intensities are far below the (upper) peak intensity. In contrast, in an intensity-difference setup the situation is much better, further improving with rising peak-intensity ratios $Q = I_0^{(a)}/I_0^{(b)}$. The green graphs, $Q = 0.99$, provide insight into the achievable mean intensity for $Q \rightarrow 1$: For the 2D configuration the mean intensity reflects, almost independently of the intensity order, the actual peak intensity. However, for the 3D case there is an appreciable deviation, especially for signals that arise at low intensity orders. Furthermore, as Q increases, the fractional signal that is kept with respect to the full signal at peak intensity becomes smaller. This behaviour is depicted in Figure 3.5 and is identical for 2D and 3D configurations. In actual experiments one needs to find a compromise between intensity resolution and remaining signal.

In the following paragraph, intensity-integrated observables and their derivatives with respect to peak intensity are elucidated. Any M -dimensional observable $S(I_0)$, e. g., a two-dimensional projection of photoelectron momenta, that results from the full laser–target interaction at peak

intensity I_0 , obeys the relation

$$S(I_0) \propto \int_0^{I_0} \Omega(I)s(I) \left(-\frac{\partial V}{\partial I} \right) dI, \quad (3.5)$$

with a normalised M -dimensional distribution $s(I)$ that is created at the distinct intensity I with probability $\Omega(I)$ and the volume $-(\partial V/\partial I) dI$ occupied by the isointensity shell dI . If $-(\partial V/\partial I) dI$ is independent of I_0 (2D configuration), the evaluation of dS/dI_0 enables the direct determination of $\Omega(I)s(I)$ by elimination of the integral sign in (3.5). This is not viable for the 3D configuration, since the volume differential is a function of I_0 . But also for this case dS/dI_0 is proportional to an effective distribution \tilde{s} , that arises from a restricted intensity spectrum as depicted in Figure 3.2 and 3.3. Thus, the acquisition of dS/dI_0 , or its discrete equivalent $\Delta S/\Delta I_0$, allows for the investigation of intensity-dependent changes in the signal distribution, while intensity-dependent occurrence probabilities, $\Omega(I)$, are not accessible.

Although a 2D focus configuration would enable the determination of intensity-dependent ionisation rates as well as momentum distributions without contamination from intensities $I < I_0^{(a)}$, the experimental realisation of such a setup suited for intensities appropriate for strong-field ionisation studies proves to be challenging. However, the evaluation of $\Delta S/\Delta I_0$ in a 3D configuration is easy to implement and provides the investigator with incident-intensity-resolved signal distributions \tilde{s} . This enables analyses of the intensity-dependence of an M -dimensional signal, while the information about the integral signal remains obscured.

3.3. Experimental setup

The experimental setup was described elsewhere^{33,88}. In brief, a cold molecular beam was created by supersonically expanding OCS seeded in 85 bar of helium through an Even-Lavie valve⁸⁹ operated at a repetition rate of 250 Hz. The skimmed molecular beam was intersected in the centre of a velocity-map imaging spectrometer (VMIS) by a laser beam from a mode-locked Ti:sapphire system, which delivered Fourier-limited pulses at 800 nm central wavelength and 35 fs pulse duration (full width at half maximum) at a repetition rate of 1 kHz. Employing a 500 mm focal length biconvex lens resulted in a laser focus with a beam waist of 44 μm and a Rayleigh length of $z_R = 7.5$ mm. The diameter of the molecular beam was found to be $D = 2.2$ mm and $2z_R > D$ provides justification for treating the longitudinal intensity distribution of the effective focus as a rectangular function (*vide supra*). The pulse energy reaching the interaction region was defined using a half-wave plate and a thin-film polariser. Ionisation of OCS could be studied employing peak intensities of 4.6–13 $\times 10^{13}$ W/cm², respectively. Due to the charge-dissipation limit of the in-vacuum detector components measurements at $I_0 > 8 \times 10^{13}$ W/cm² were conducted at a reduced sample density – namely 1/3 of the density employed for measurements at $I_0 \leq 8 \times 10^{13}$ W/cm². This was achieved by delaying the laser pulses with respect to the maximum of the molecular beam's temporal profile. Sample densities of 1×10^8 cm⁻³ and $1/3 \times 10^8$ cm⁻³ were utilised, respectively. Peak intensities as determined by a combination of beam-profiling, auto-correlation, and measurement of the pulse energy were found to be too low by 20 % compared to the intensity-dependent kinetic energy shift of distinct above-threshold ionisation (ATI) peaks, see (3.8). In combination with the known energy spacing between adjacent ATI peaks, namely the photon energy $h\nu$, this approach allowed for an intrinsic calibration of both, the photoelectron momentum and the laser intensity. Two-dimensional projections of photoelectron momenta were recorded by mapping the electrons onto a position-sensitive detector, consisting of a microchannel plate (MCP), a phosphor screen and a high-frame-rate camera (Optronis CL600), by means of a VMIS. This detection scheme allowed for counting and two-dimensional momentum-stamping of single electrons. The momentum resolution achieved – given by the voltage applied to the VMIS electrodes and the pixel size of the camera – was

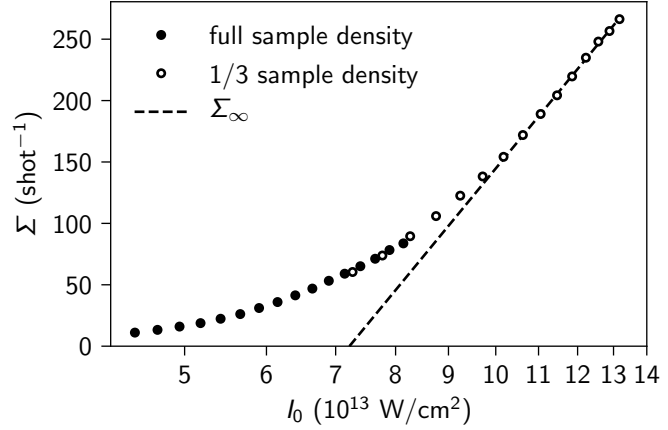


Figure 3.6: Experimental electron count rates versus the peak intensity on a semilogarithmic scale (dots). Open dots represent measurements conducted at 1/3 of the maximum sample density, rescaled accordingly to match those recorded at full density. The asymptotic behaviour beyond the saturation intensity is depicted by the dashed line.

5.6×10^{-3} atomic units (electron velocity of 12 km/s). Momentum slices of the full three-dimensional momentum distributions $S(I_0)$ were recovered through inverse Abel-transformations employing the ‘‘Onion-Bordas’’ onion-peeling algorithm^{90,91} as implemented in the PyAbel software package⁹².

3.4. Results and discussion

3.4.1. Integral photoelectron yield

Extensive strong-field ionisation studies⁷⁶ employing various laser peak intensities demonstrated that the asymptotic slope of an integral ionisation signal $\Sigma(I_0)$ with respect to $\ln I_0$, arising from the full intensity spectrum of the laser–target interaction at peak intensity I_0 , follows

$$\lim_{I_0 \rightarrow \infty} \left(\frac{d\Sigma}{d \ln I_0} \right) = 2\pi\alpha\sigma_r^2 D \varrho. \quad (3.6)$$

α is the instrument sensitivity, σ_r the standard deviation of the transverse intensity distribution, D the length of the focus volume and ϱ the sample density. The only requirements for the validity of this equation are the predominance of single ionisation and the cylindrical symmetry of the spatial focus geometry. Due to the onset of saturation, starting at intensity I_{sat} , the slope of $\Sigma(\ln I_0)$ converges to a constant value for increasing peak intensity. Within the notation of this chapter, $\Sigma(I_0)$ equals the momentum-space integral of the distribution $S(I_0)$, which for the present case is just the total number of electrons detected. Figure 3.6 shows the resulting values of Σ plotted versus I_0 on a semilogarithmic scale. With increasing values of $\ln I_0$ the slope of the total electron yield converges to a constant value. In the following analysis, this behaviour is used as implicit evidence for a negligible contribution from multiple ionisation. The asymptotic slope and the saturation onset were deduced by modelling a line through the highest peak-intensity points providing a saturation onset of $I_{\text{sat}} = 7.2 \times 10^{13} \text{ W/cm}^2$. The saturation intensity is a function of both the pulse duration and the orientation-dependent ionisation probability⁷⁶. Using the MCP’s open-area ratio of 0.64 as instrument sensitivity α , a transverse focal standard deviation of $\sigma_r = 22 \text{ }\mu\text{m}$ (beam waist of $44 \text{ }\mu\text{m}$) and a molecular beam diameter of $D = 2.2 \text{ mm}$ resulted in a sample density of $\varrho = 1 \times 10^8 \text{ cm}^{-3}$. Since the intensity could be intrinsically calibrated from the ponderomotive shift of the ATI peaks (see next subsection), the deduced sample density is as accurate as $\alpha\sigma_r^2 D$.

3.4.2. Radial and angular distributions

Due to their rotational symmetry the three-dimensional momentum distributions $S(I_0)$ can be completely described by two-dimensional slices of momenta parallel (p_{\parallel}) and perpendicular (p_{\perp}) to

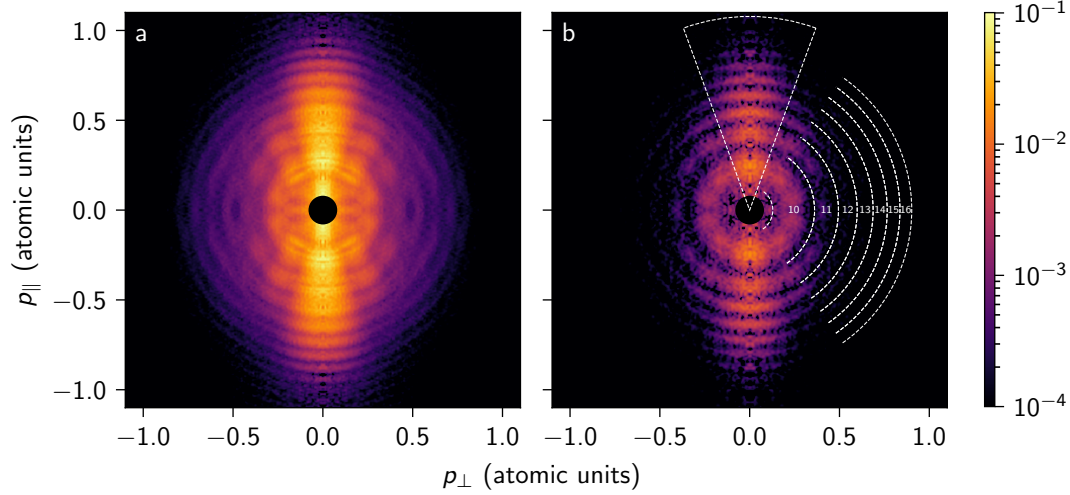


Figure 3.7.: Photoelectron momentum slices a) for the full-intensity distribution S at a peak intensity of $5.7 \times 10^{13} \text{ W/cm}^2$ and b) for the differential-intensity distribution S' , which is dominated by intensities of $5.4\text{--}5.7 \times 10^{13} \text{ W/cm}^2$. The white-line wedge sketches the polar angles used to evaluate the intensity-dependent radial distributions shown in Figure 3.8 and 3.9; the white arcs separate contributions from distinct photon numbers N and correspond to kinetic energies $T(N \pm 0.5, \tilde{l}_0)$ as obtained from (3.8).

the polarisation axis. In the following, the slope of S with respect to l_0 ,

$$S'(\tilde{l}_0) = \frac{\Delta S}{l_0^{(b)} - l_0^{(a)}}, \quad (3.7)$$

is analysed regarding its radial and angular distributions. Here, the mean intensity \tilde{l}_0 corresponds to the arithmetic mean of every two peak intensities $l_0^{(b)} > l_0^{(a)}$ that were used to measure S . Since $S'(\tilde{l}_0)$ arose from a more narrow distribution of incident intensities than $S(l_0)$, it allows for the detailed investigation of intensity-dependent effects.

Both $S(l_0)$ and $S'(\tilde{l}_0)$ exhibit rich angular and radial structure. Figure 3.7 displays a typical momentum slice for the two cases, here for intensities around $5.5 \times 10^{13} \text{ W/cm}^2$. Both momentum distributions show broad radial patterns that repeat with integer multiples of the photon energy – referred to as ATI structure –, sharp radial features on top of the ATI structures – referred to as Freeman resonances⁹³ – and a carpet-like pattern perpendicular to the polarisation axis⁹⁴.

Radial distributions

In Figure 3.8, the peak-intensity-dependent radial distributions for polar angles between -20° and $+20^\circ$ with respect to the polarisation axis are illustrated for $S(l_0)$. There are two kinds of features to be noted: (i) broad peaks with a spacing of $h\nu$ that experience a shift in kinetic energy proportional to the negative value of the peak intensity and (ii) sharp peaks at constant kinetic energies. The radial distributions of $S(l_0)$ are dominated by feature (ii). Figure 3.9 displays the equivalent radial distributions for $S'(\tilde{l}_0)$, which exhibit predominant contributions from feature (i). Note that there is a change in sample density and intensity bin size at $8.3 \times 10^{13} \text{ W/cm}^2$, cf. Figure 3.6.

In the following, feature (i), which corresponds to nonresonant above-threshold ionisation, is analysed employing the radial distributions of $S'(\tilde{l}_0)$. Dashed black lines in Figure 3.9 correspond to final kinetic energies⁹⁵

$$T(N, \tilde{l}_0) = N h\nu - I_p^{(0)} - U_p(\tilde{l}_0), \quad (3.8)$$

with the number of absorbed photons N , the photon energy $h\nu = 1.55 \text{ eV}$, the field-free ionisation

Figure 3.8: Radial distributions of $S(l_0)$ were evaluated for polar angles between -20° and $+20^\circ$ as sketched in Figure 6.3b: a) intensity-integrated radial distribution carrying imprints of Freeman resonances with principal quantum numbers $n = 4, 5, 7, 8$ indicated for $k = 1$ (solid red lines) and $k = 2$ (dashed red lines) as obtained through (3.9) and b) peak-intensity-dependent radial distributions. Values of $S(l_0)$ are mapped onto a square-root colour scale.

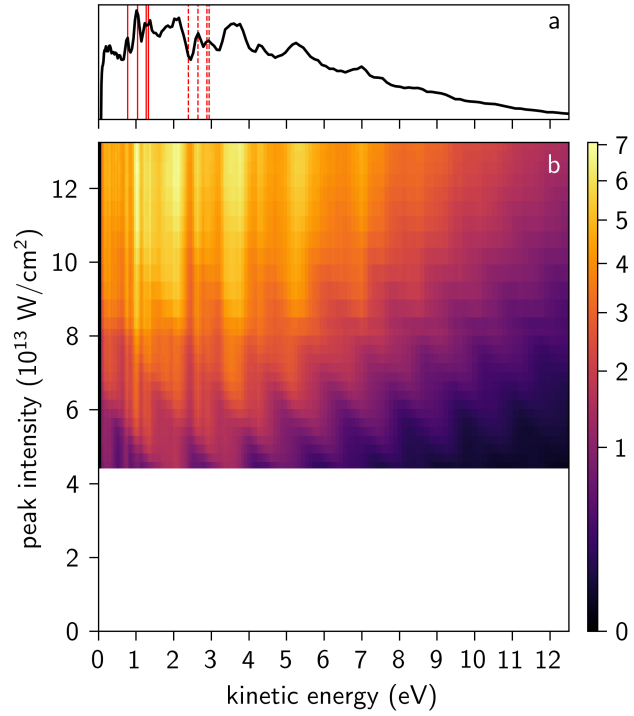
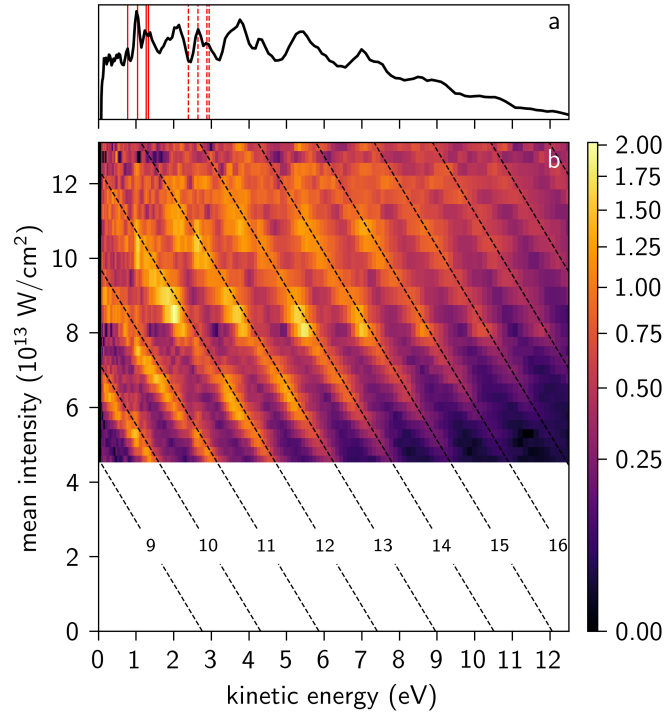


Figure 3.9: Radial distributions of $S'(\tilde{l}_0)$ were evaluated for polar angles between -20° and $+20^\circ$ as sketched in Figure 6.3b: a) intensity-integrated radial distribution and b) intensity-dependent radial distributions. Broken black lines in b) depict ponderomotively shifted final kinetic energies as obtained through (3.8) for the given numbers of photons. Values of $S'(\tilde{l}_0)$ are mapped onto a square-root colour scale.



potential of OCS, $I_p^{(0)} = 11.19 \text{ eV}$ ⁹⁶, and the ponderomotive potential $U_p = \tilde{I}_0/4\omega^2$ (for atomic units). Clearly, (3.8) describes the kinetic energies of the radial local maxima in Figure 3.9 quite well except for minor deviations towards lower kinetic energies at $T < 3 \text{ eV}$, which are ascribed to the Coulomb interaction between photoelectron and cation. Thus, the total ionisation energy appears to be dictated by the ponderomotive continuum shift. For the intensity range of the current study the relative Stark shift between the neutral and the cationic species is dominated by the permanent-dipole interaction¹⁵ and, hence, equals zero in average over the isotropic distribution of molecular orientations.

Within the peak-intensity range investigated all radial distributions of $S(I_0)$ carry series of sharp peaks, feature (ii), that are also reproduced periodically with the photon energy $h\nu$. Close inspection of Figure 3.9 reveals that the kinetic energies of those peak series are independent of the incident intensity, i. e., they appear as vertical lines imprinted onto the nonresonant ATI pattern, feature (i). Based on this intensity-independence and the energy spacing between individual series, these peaks can unambiguously be assigned to Freeman resonances⁹³, i. e., photoelectron emission from resonance-enhanced multiphoton ionisation through Rydberg states. Since those Rydberg states experience the same ac Stark shift as their corresponding continua, namely the ponderomotive energy, the resulting final kinetic energies T_F are independent of the incident intensity^{95,97}:

$$T_F(k, n) = kh\nu - \frac{R_\infty}{(n + 0.25)^2}, \quad (3.9)$$

with the number of photons k that ionise a resonant Rydberg state with principal quantum number n and the Rydberg constant R_∞ . The subtrahend reflects the energy difference between the Rydberg state and its asymptotic unbound state. Resonant transitions for $n = 4, 5, 7$ could be observed together with a combination band for $n = 8 \dots 10$, with $k = 1 \dots 3$. These assignments agree with previous single-photon absorption studies on OCS⁹⁸⁻¹⁰⁰. In the present study, individual angular momentum states could not be resolved: At a kinetic energy of 1.2 eV, where the $k = 1$ Freeman manifold occurred, an energy resolution of 0.05 eV was achieved, which is roughly ten times larger than what would be required to distinguish between different ℓ states.

Previous results on OCS for comparable peak intensities of $2.8-9.4 \times 10^{13} \text{ W/cm}^2$, analysed without the intensity-difference spectra, lacked information about the incident ponderomotive shift and, hence, assigned intensity-independent photoelectron lines to valence-valence transitions⁷⁹. Three sharp peaks in the photoelectron kinetic energy spectra, which follow $T_{1,3} = 0.73 \text{ eV} + \tilde{k}h\nu$, with $\tilde{k} = (0, 1)$, and $T_2 = 1.17 \text{ eV}$, were attributed to the valence transitions ${}^1\Delta \leftarrow \tilde{X}{}^1\Sigma^+$ and ${}^1\Pi \leftarrow \tilde{X}{}^1\Sigma^+$. The corresponding excited valence states have field-free vertical ionisation energies of roughly 5.8 eV (${}^1\Delta$) and 3.9 eV (${}^1\Pi$)⁹⁹. Both, the ${}^1\Delta$ and the ${}^1\Pi$ state, were considered to experience ac Stark shifts equal to the ponderomotive potential, resulting in intensity-independent kinetic energy releases⁷⁹. Since U_p is the kinetic energy imparted to an unbound electron in an oscillating electric field, it represents the asymptotic ac Stark shift of an electronic state at the onset of the continuum. However, treating the ${}^1\Delta$ and ${}^1\Pi$ states as quasi-unbound states is in conflict with their large binding energies. Thus, in our present investigation the very same three peaks are, instead, assigned to ionisation of resonant Rydberg states leading to final kinetic energies of $T_{1,3} = T_F(k = (1, 2), n = 4)$ and $T_2 = T_F(k = 1, n = 7)$.

While $S'(\tilde{I}_0)$ mainly carries contributions from nonresonant above-threshold ionization, $S(I_0)$ is dominated by resonance-enhanced multi-photon ionisation. Through averaging over all intensities present in the focal volume the ponderomotively shifted nonresonant contributions get washed out in the final momentum distribution $S(I_0)$, while resonant contributions with constant final momentum, e. g., Freeman resonances, gain intensity¹⁰¹. By inspection of $S(I_0)$ only, the contributions from resonant ionisation pathways are highly overestimated and final kinetic energies cannot be related to distinct numbers of absorbed photons, because the ponderomotive continuum shift U_p cannot be resolved. In the momentum distributions $S(I_0)$, the closing of ionisation channels with increasing

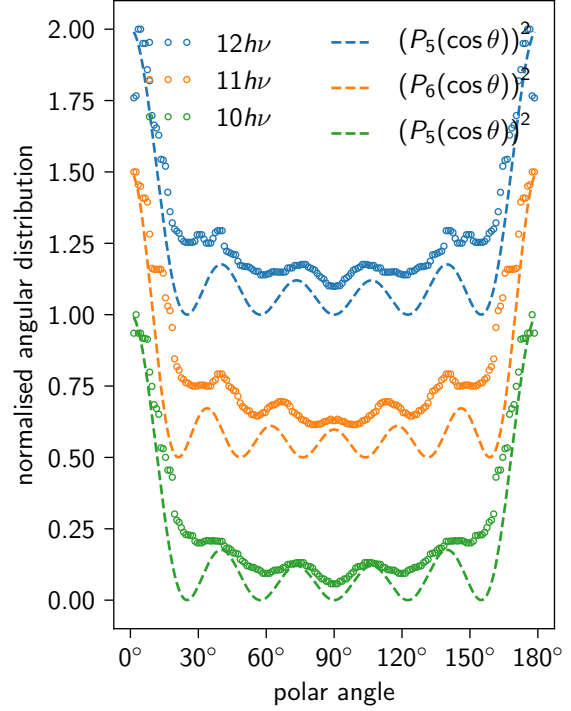


Figure 3.10: Angular distributions of the lowest-order nonvanishing ATI channels for the minimum photon numbers of 10, 11, 12 required to ionise the OCS molecule. The three distributions were retrieved within the intensity intervals 4.6–7.2, 7.2–9.8 and 9.8–12.4 $\times 10^{13}$ W/cm², which represent the channel-closing intensities obtained by setting $T(N, \tilde{I}_0) = 0$ in (3.8). Experimental data are shown by circles, calculated traces of the squares of Legendre polynomials $P_\ell(\cos\theta)$ of order ℓ , with the polar angle θ to the laser polarisation axis, are shown by dashed lines. The distributions are plotted with an arbitrary vertical offset for clarity.

peak intensities is highly obscured, because contributions from all intensities between 0 and I_0 are contained. Thus, even if a channel is already closed at the peak intensity, $S(I_0)$ will embody all contributions from $I < I_0$ with even larger weight, i.e., larger differential volume, at which the channel is still open. In principle, $S(I_0)$ contains just more and more open ionisation channels with increasing peak intensity. Nevertheless, experimental evidence for channel-closing was reported for xenon at fully focal-volume averaged momentum distributions^{80,81}. In the present study, three channel-closings could be clearly observed, visible in Figure 3.9 at intensities when the ATI peaks assume zero kinetic energy.

Angular distributions

In the following, the nonresonant ATI channels for ionisation with a minimum number of photons are analysed with respect to their photoelectron angular distributions. These channels give rise to the lowest radial layers of the carpet-like pattern⁹⁴ visible in Figure 3.7a. The minimum number of photons needed to ionise the target is a staircase function proceeding upward with increasing intensity. Accordingly, $S'(\tilde{I}_0)$ was sectioned by the channel-closing intensities, which were obtained by evaluating the roots of (3.8). Within the intensity range investigated, the closing of the 9, 10, 11, 12 photon channels were encountered at intensities of 4.6, 7.2, 9.8, 12.4 $\times 10^{13}$ W/cm², respectively. In Figure 3.10, circles depict the resulting angular distributions for ionisation by 10, 11, 12 photons, each representing the lowest-order nonvanishing ATI channel in its corresponding intensity regime. The angular distributions associated with the absorption of 10, 11, 12 photons exhibit 5, 6, 5 local minima, respectively.

As shown by a theoretical study of the strong-field ionisation of atomic hydrogen¹⁰² and by experimental investigations of xenon⁸⁰, the dominant orbital angular momentum quantum number ℓ of the emitted electrons can be deduced from fitting the angular distributions by squared Legendre polynomials $(P_\ell(\cos\theta))^2$ of order ℓ . According to the number of local minima the absorption of $N = 10, 11, 12$ photons gives rise to dominant orbital angular momentum quantum numbers of $\ell = 5, 6, 5$. Best matches of $(P_\ell(\cos\theta))^2$ to the experimental angular distributions are shown as dashed lines in Figure 3.10.

An empirical rule was given that predicts the dominant photoelectron orbital angular momentum quantum number ℓ based only on the minimum number of photons to reach the continuum and the orbital quantum number ℓ_0 of the initial bound electronic state¹⁰³. For intensities implying minimum numbers of 10, 11, 12 photons needed to ionise argon, ground state configuration $[\text{Ne}]3s^23p^6$ ($\ell_0 = 1$), dominant orbital angular momentum quantum numbers of $\ell = 5, 6, 5$ were found. These values for ℓ agree with those obtained for OCS, ground state configuration $\dots 9\sigma^23\pi^4$ ($\ell_0 = 1$), providing clear evidence of the empirical rule and its extension to molecules.

The time-dependent Schrödinger equation for the strong-field ionisation of H and Ar pictured the trajectory of the outgoing electron as a quiver motion along the laser-polarisation axis superimposed to a drift motion following a Kepler hyperbola¹⁰⁴. Identifying the hyperbola's pericentre as the electron's quiver amplitude in the field provided an analytical expression for an effective final orbital momentum that for single ionisation only depends on the electron's final linear momentum and its quiver amplitude in the field. For the ionisation of OCS through 10, 11, 12 photons effective orbital quantum numbers $\tilde{\ell} = 5.5, 6.5, 7.1$ were obtained accordingly¹⁰⁴. Although this model considers neither the initial state's orbital momentum nor a parity selection rule, the values for $\tilde{\ell}$ reflect our experimental observations remarkably well. This further supports the statement that the momentum distribution of an electron wave packet from nonresonant strong-field ionisation is dictated by the electric field and its Coulomb interaction with the cation. The initial bound electronic state imprints onto the free-electron wave packet through its vertical ionisation energy, its orbital angular momentum, and the symmetry of its electron density distribution. While the impact of the former two properties was demonstrated within the scope of this work, the investigation of the latter would require referencing to the molecular frame.

3.5. Conclusions

Three-dimensional photoelectron momentum distributions from strong-field ionisation of OCS at differential peak intensities were recorded and analysed in matters of resonant Rydberg states and photoelectron angular momentum. The evaluation of the derivatives of the momentum distributions with respect to the peak intensity allowed for the unambiguous recognition of Freeman resonances. As a result, sharp photoelectron lines, previously ascribed to valence–valence transitions⁷⁹, were reassigned to progressions of Freeman resonances corresponding to Rydberg states with principal quantum numbers $n = 4, 5, 7, 8, 9, 10$. Furthermore, the empirical rule that relates the initial state's angular momentum and the minimum photon expense to ionise an ac-Stark-shifted atomic system to the observable dominant photoelectron momentum¹⁰³ could be confirmed for a molecular target. In addition, the clear closing of ionisation channels with increasing peak intensity is shown for the OCS molecule, which could eventually enable the probing of a distinct strong-field ionisation channel in a coherent-control experimental setup. It is demonstrated that in order to gain insight into strong-field ionisation processes on a quantum-mechanical level it is essential to relate distinct incident intensities to the resulting response of the system under investigation. Especially for the exploration of the transition regime between multiphoton and tunnelling ionisation a well-defined and narrow intensity distribution is crucial. Studies employing a clear relation between incident intensity and target response could finally shed light onto the importance of resonant states and, thus, show the shortcomings of present molecular strong-field ionisation theories to describe the outgoing electron wave packet.

4 The role of molecular-orbital structure in strong-field-driven electron–molecule collisions²

4.1. Introduction

In the prototypical strong-field interaction, an intense driving field extracts a valence electron from the target through tunnel ionisation, accelerates the free electron in vacuum, and eventually drives it back to the parent ion, predominantly resulting in rescattering or radiative recombination^{61,105}. The radiative recombination results in the emission of high-energy photons by high-harmonic generation⁶¹ and this is a powerful tool to investigate the electronic structure with attosecond temporal resolution^{106–108}. Alternatively, the rescattered portion of this electron wavepacket is exploited in laser-induced electron diffraction (LIED)¹⁸ experiments as a coherent diffraction pattern of the molecular target, potentially providing time-dependent images of the molecule at sub-femtosecond and few-picometre resolution. Recently, corresponding experimental results for the structure or dynamics of small or highly-symmetric molecules were obtained^{20,72,109–112}. At the same time, the initial conditions of the strong-field interaction have attracted much attention for capturing the intrinsic nature of strong-field physics.

While pioneering attosecond experiments and molecular-frame measurements revealed nontrivial spatiotemporal features in electron tunnelling^{113,114}, these initial conditions are still generally considered a weak perturbation in strong-field physics. All the results obtained in LIED experiments, for example, are interpreted in the framework of the strong-field approximation, where the electron is considered to be born in the continuum with a negligible initial momentum and to propagate as a plane wave¹¹⁵. Furthermore, the post-ionisation dynamics before rescattering are assumed to be fully driven by the laser field, by neglecting, for example, the Coulomb interaction with the ionised molecule.

Common strategies to analyse photoelectron momentum distributions rely on the quantitative rescattering theory (QRS)¹¹⁵, where angular dependence in the final photoelectron wavepacket is introduced solely through rescattering. Within this approach, diffraction patterns were analysed utilising the angular^{20,72} or radial¹¹⁶ photoelectron distribution. However, the relevance of the ionised molecular orbital in the rescattered photoelectrons is still under discussion¹¹⁷. So far, this was included by an overall weighting factor in the rescattering probability^{118,119}, or as a spatial phase or an angular feature in the rescattering electron wavepacket^{114,120}. Recently, the influence of molecular alignment on molecular structure retrieval was discussed^{116,121}. However, general predictions are still extremely challenging with new models appearing^{122,123}.

Here, we experimentally and computationally study molecular-frame photoelectron spectroscopy from strongly aligned molecules in order to investigate the relation between the molecular frame and the strong-field-induced ultrafast electron dynamics. We demonstrate that and how the molecular

²This chapter is based on the publication A. Trabattoni, J. Wiese, U. De Giovannini, J.-F. Olivieri, T. Mullins, J. Onvlee, S.-K. Son, B. Frusteri, A. Rubio, S. Trippel, and J. Küpper, “Setting the photoelectron clock through molecular alignment,” *Nature Comm.* **11**, 2546 (2020). I contributed to this work by performing the experiment together with A. T., S. T., J.-F. O., T. M., and J. O., setting up and executing the semiclassical trajectory calculations by myself, and interpreting the results and preparing the manuscript together with A. T., S. T., U. D. G., A. R., and J. K..

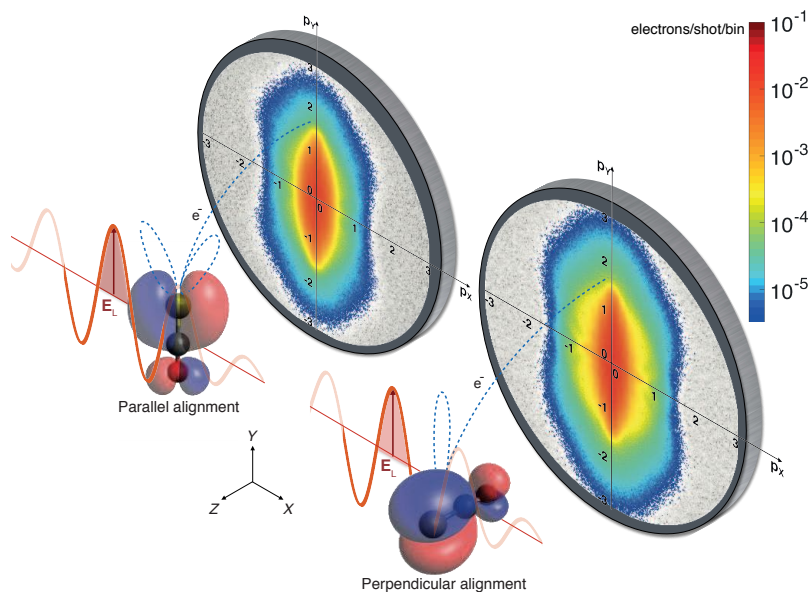


Figure 4.1.: Sketch of the experimental arrangement. OCS molecules (O in red, C in black, S in yellow) were aligned in the laboratory frame, parallel and perpendicular to the Y axis. The ionising laser-electric field (E_L) was linearly polarised along the Y axis and the detection was in the XY plane. The molecular-frame angle-resolved photoelectron spectra were projected onto a 2D detector in a velocity-map-imaging spectrometer. The alignment-dependent photoelectron trajectories are pictorially shown (blue dashed lines), as well as the corresponding shape of the ionising orbital (blue and red lobes). The spectra are displayed on a logarithmic intensity scale in units of electrons/shot/bin.

frame governs the rescattering time for the photoelectron and, consequently, its final kinetic energy.

4.2. Results

4.2.1. Experimental approach

Figure 4.1 depicts the experiment. An ensemble of carbonyl sulfide (OCS) molecules all in the rovibronic ground state³³ was adiabatically aligned in the laboratory frame, with $\langle \cos^2 \theta_{2D} \rangle = 0.9$, by using a linearly polarised, 500 ps laser pulse, centred at 800 nm^{43,88}, with a peak intensity $I = 3 \times 10^{11} \text{ W cm}^{-2}$. The molecules were aligned in two different configurations, shown in Figure 4.1, with the molecular axis along the Y and Z axes, named parallel and perpendicular alignment, respectively. A second laser pulse, centred at 1300 nm, with a duration of 65 fs, and a peak intensity $I = 8 \times 10^{13} \text{ W cm}^{-2}$, was used to singly ionise the OCS molecules. For this intensity, the ponderomotive energy of the laser field is $U_p \approx 13 \text{ eV}$ and the ionisation occurred in the tunnelling regime. The electric field of the ionising laser pulse, E_L in Figure 4.1, was linearly polarised along the Y axis (ellipticity $\epsilon = I_Z/I_Y < 0.005$). The produced molecular-frame angle-resolved photoelectron spectra (MF-ARPES) were recorded in a velocity-map imaging spectrometer (VMIS)¹²⁴ with its detector parallel to the XY plane. It is important to note that the de Broglie wavelength of rescattering electrons in the experiment was larger than 200 pm. In this regime no diffraction feature is expected to appear in the photoelectron distributions¹¹⁶.

4.2.2. Photoelectron momentum distributions

Figure 4.1 shows the MF-ARPES for parallel (left) and perpendicular (right) alignment. The two distributions show several differences. The spectrum for parallel alignment has a larger width at

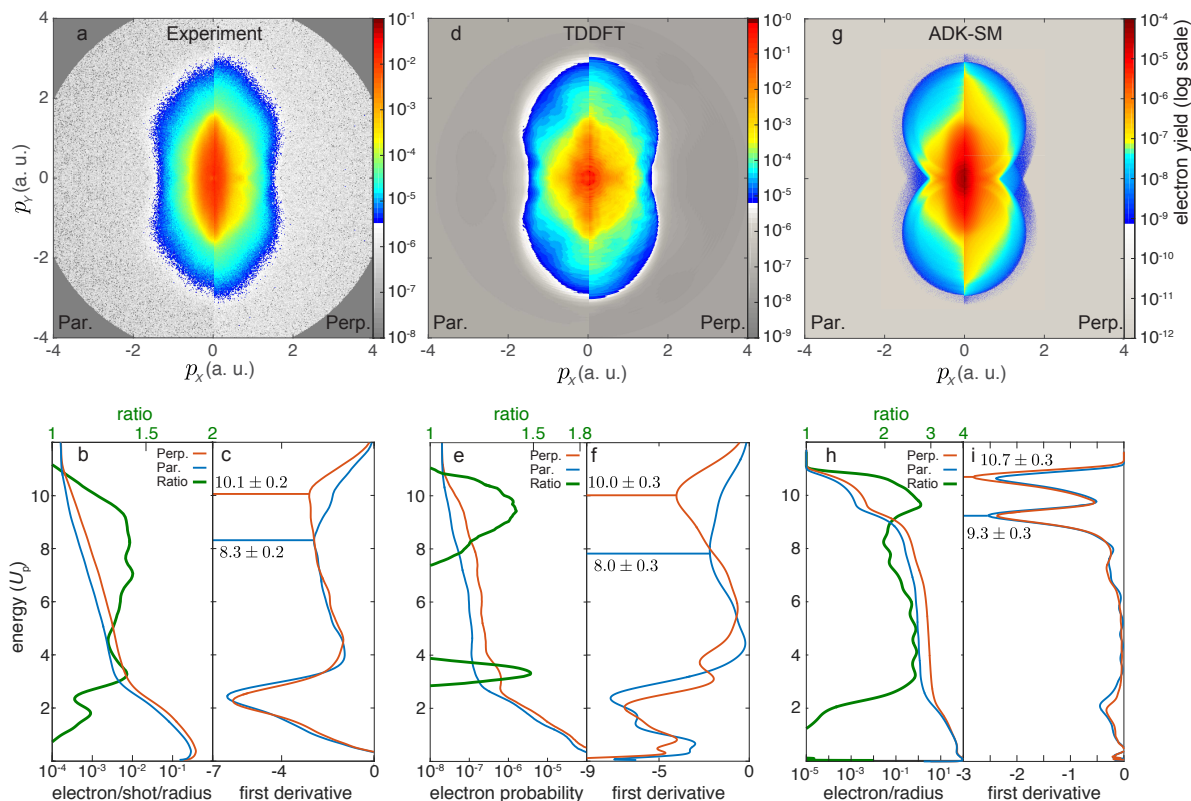


Figure 4.2.: Molecular-frame angle-resolved photoelectron spectra of OCS. These data were obtained **a, b, c** experimentally and computationally from **d, e, f** TDDFT and **g, h, i** ADK-SM calculations. **a, d, g:** Split graphical representation as a comparison of the photoelectron distributions for parallel and perpendicular alignment for the experimental and computational results, respectively. **b, e, h:** Corresponding projected energy distributions of photoelectrons along the Y axis, angularly integrated within a cone of $\pm 20^\circ$, as well as the ratio of the integral-normalised perpendicular and parallel distributions, on logarithmic scales. Energies are reported in units of the ponderomotive energy U_p . **c, f, i:** First derivatives of the photoelectron-energy distributions to evaluate the high-energy cutoff for the two molecular-alignment cases. All TDDFT computational results were obtained by averaging over different laser–molecule orientations according to the experimental alignment distributions and by adding a constant to account for the experimental background level. The ADK-SM results refer to a single laser intensity and perfect alignment for both cases. See appendix A.2 for details.

small transverse momenta, $p_x < 0.5$ a. u. (atomic units), while the spectrum for perpendicular alignment shows a number of angular features for transverse momenta p_x between 0.5 a. u. and 1 a. u.. These angular structures, which are much weaker in the spectrum for parallel alignment, could be identified as forward-rescattering features¹²⁵. Focussing the attention on large longitudinal momenta p_y , the counts for parallel alignment drop around 2.5 a. u.. In the case of perpendicular alignment, however, the spectrum extends to larger momenta, showing an appreciable amount of counts at $p_y = 3$ a. u.. Following the strong-field approximation, the hard cutoff of photoelectron momentum is expected to only depend on the properties of the laser field⁷³. Experimentally, this quantity is hard to measure. Thus, the turning point of the signal drop, i. e., the minimum of the first derivative, at large longitudinal momenta is used instead. In the following, we use the term cutoff in the latter sense. Surprisingly, in the current study we found a clear dependence of the cutoff on the molecular frame.

Figure 4.2a shows a close comparison of the two experimental distributions for the complete range of p_x and p_y , between 0 and 4 a. u.. Here, the spectra were split along the Y axis and the spectrum from parallel alignment is shown on the left and the one from perpendicular alignment on

the right. Now, the differences at small momenta as well as at the cutoff are even more evident. To perform a quantitative analysis of the cutoffs, the momentum distributions were angularly integrated within a cone of $\pm 20^\circ$ with respect to the longitudinal axis (Y) and converted to an energy scale. In Figure 4.2b the resulting photoelectron spectra are shown for parallel (blue) and perpendicular (red) alignment, with energies in units of U_p . The perpendicular/parallel ratio of the two area-normalised spectra (green) shows a predominance of photoelectrons for perpendicular alignment in the energy range between $2 U_p$ and $10 U_p$, where the distribution is dominated by rescattered electrons¹²⁶. Furthermore, the ratio increases with energy, reaching the maximum around the cutoff. To evaluate the cutoffs, the first derivative of the energy distributions are shown in Figure 4.2c and their minima were used to find the edges of the distributions, which allowed us to analyse the cutoff region. The first minimum represents the drop of direct electrons¹²⁶ and it was around $2 U_p$ for both alignment cases. This excluded any significant alignment-dependent direct-electron-cutoff enhancement¹²⁷. Surprisingly, the second minimum behaves differently for the two alignments. While it is located around $10 U_p$ for perpendicular alignment, as expected from the well established above-threshold ionisation theory⁷³, the cutoff is shifted down to a value around $8.5 U_p$ for parallel alignment.

4.2.3. Quantum-mechanical model of the electron dynamics

To unravel the experimental observations, state-of-the-art calculations were performed using both time-dependent density functional theory (TDDFT)¹²⁸ and a semiclassical molecular trajectory simulation setup. Using TDDFT, the MF-ARPES probability was calculated by simulating the complete dynamics of the many-body ionisation process in real-time and real-space with the tSURFF method^{129,130}, see appendix A.1 for details. With this technique the spectrum was obtained by computing the entire time-dependent electron dynamics, including many-body electron interactions, and collecting the flux of electrons through a closed surface surrounding the molecule. Figures 4.2d–f report the same analysis of the numerical results as performed for the experimental data in Figures 4.2a–c. The simulations capture the principal features of experimental data very well. In particular, Figure 4.2f shows that the calculations reproduce the experimental cutoff positions for parallel and perpendicular alignment as well as the corresponding shift between them very well. This result is strongly affected by the electron–electron interaction and the interplay between different orbitals. Indeed, it is evident from the calculation that the molecule is predominantly ionised from the highest occupied molecular orbital (HOMO) for both alignments. In the case of parallel alignment, nevertheless, a small contribution of HOMO–1 to the yield of high-energy rescattered electrons is observed. When the electron–electron interaction is artificially turned off, the HOMO–1 contribution becomes significant and in this scenario the reduced cutoff observed in the experiment is not reproduced, see Figure A.4 in the appendix. Instead, in the case of fully interacting electrons the yield of the rescattered electrons ionised from HOMO–1 is suppressed, resulting in the really good agreement with the experiment.

4.2.4. Semiclassical model of the electron dynamics

Furthermore, semiclassical trajectory simulations based on the Ammosov-Delone-Krainov (ADK) tunnelling theory⁵⁹ in conjunction with a simple-man propagation (SM)^{131,132} were conducted in order to track the molecular-frame electron dynamics during the strong-field interaction⁴⁹, see appendix A.2 for details. Based on the TDDFT analysis of the different molecular orbitals contributing to the photoelectron dynamics, the ionisation was assumed to occur solely from HOMO. In the underlying model, the initial phase-space distribution of the electron wavepacket in the continuum at birth was described by the quasistatic ADK tunnelling theory, and the nodal structure of the HOMO was accounted for as imprint onto this initial momentum distribution. Post-ionisation dynamics of the electron wavepacket were evaluated in the combined interaction with the laser-electric field and the cation’s Coulomb field modelled as a point charge. To evaluate the accuracy of this semiclassical

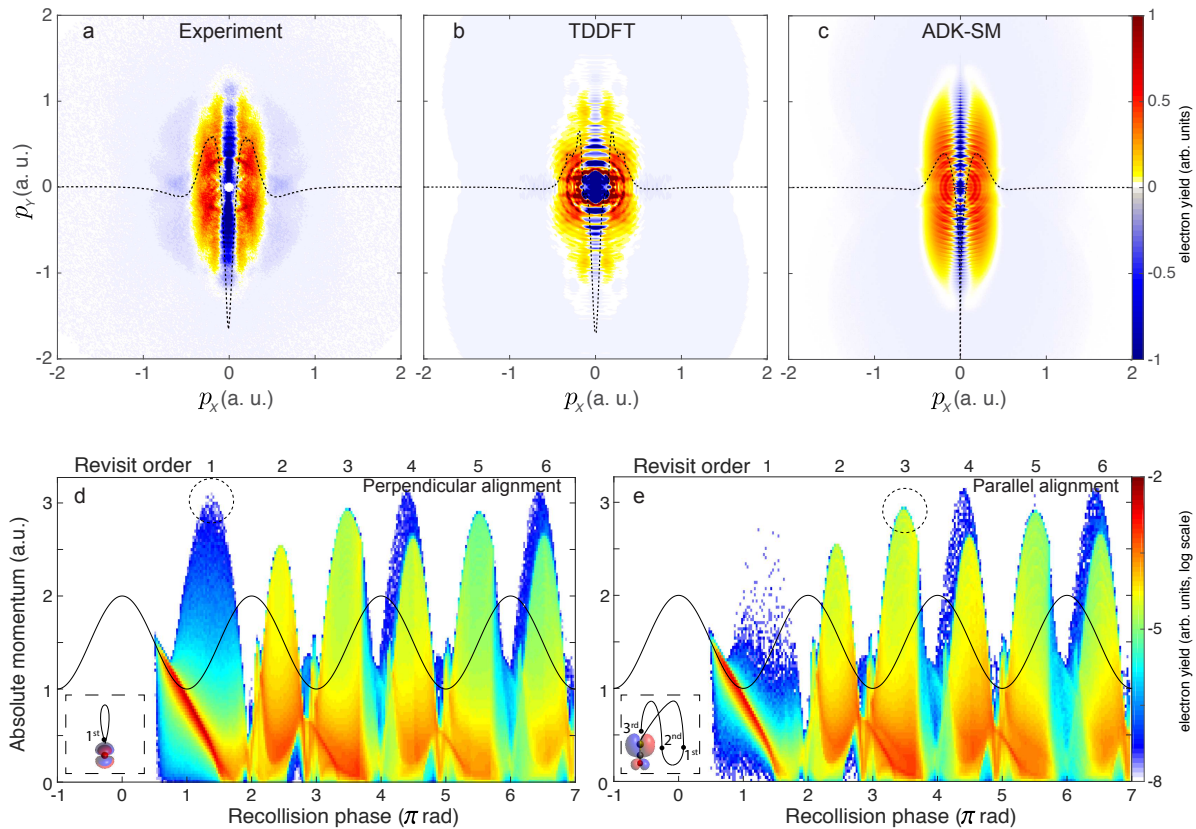


Figure 4.3.: Differential momentum distributions and simulated final absolute photoelectron momentum. **a, b, c:** Differential momentum distributions (parallel – perpendicular) from **a** the experiment, **b** the TDDFT and **c** the ADK-SM calculations. To estimate the difference of the transverse momentum component the signal is integrated along the Y axis, shown by the black dashed lines. **d, e:** Final absolute photoelectron momentum as a function of the recollision phase (bottom) and revisit order (top) for **d** perpendicular and **e** parallel alignment, calculated with ADK-SM. The colour scale maps the electron counts at every momentum–phase point. The dashed black circles highlight the largest-momentum electrons at the most probable revisit order for the two alignments. A distance of $r < 5$ atomic units between electron and point charge is interpreted as a collision and only electrons with exactly one collision are shown. The solid black line depicts the external electric field. The insets give pictorial representations of molecular-frame electron trajectories, where the cardinals represent the revisit order.

description, the resulting MF-ARPES for parallel and perpendicular alignment were calculated and analysed, see Figures 4.2g–i, and they show good agreement both with the experimental data and with the full TDDFT calculation, reproducing the main features and cutoffs observed in the experiment very well. In particular, as seen by the local maximum around $10 U_p$ of the ratio of the two alignment cases, Figure 4.2h, this semiclassical model captures the enhanced yield of high-energy rescattered electrons for perpendicular alignment with respect to parallel alignment. This result is corroborated by the enhanced cutoff around $10.7 U_p$ for perpendicular alignment in Figure 4.2i, although a smaller yield at this energy is present also for parallel alignment. In addition, a relevant minimum appears around $9.3 U_p$ for both alignments. These features of ADK-SM, together with the pronounced yield along the centreline of Figure 4.2g, are known to be mainly due to Coulomb focussing¹³³, i. e., the dynamics of a continuum electron wavepacket being focussed along a perfectly linear laser polarisation axis. The relevance of this effect is discussed further below.

4.2.5. Differential analysis of the momentum distributions

To obtain a more comprehensive picture of the alignment-dependent photoelectron dynamics and, in particular, a glimpse at the initial electron wavepacket, we performed a differential analysis by subtracting the photoelectron distributions of the two alignment cases from each other. Figures 4.3a–c show the relative normalised differences, parallel minus perpendicular, for the experiment, the TDDFT simulations, and the ADK-SM calculations, respectively. The agreement between experimental data and both models is excellent. Here, a strong depletion along the vertical axis and two transversely offset broad lines of positive yield appear as main features, with a really good agreement between experimental and both computational results. The depletion along the centreline is due to the nodal structure of the degenerate π HOMO of OCS: It represents a forbidden direction of electron ejection^{15,118}. Therefore, when the molecular axis was aligned along the polarisation axis of the strong field, the electron preferentially acquired an initial transverse momentum p_{0X} that was much larger than in the case of perpendicular alignment, shown by the red vertical ridges in Figures 4.3a–c.

4.3. Discussion

The features observed in Figures 4.3a–c show the crucial impact of the electronic structure on the initial conditions of the electron at birth. However, a quantitative evaluation of the initial conditions of the electron at tunnelling is challenging^{134–136}. In general, they are defined by the tunnel-exit position as well as by the temporal phase and the momentum acquired during the ionisation with respect to the external field. Here, we demonstrate that the molecular potential, i. e., the combination of the electrostatic potential and the electronic structure of the molecule, has in fact not only a primary role in setting the initial conditions for electron emission, but that it also drives the whole photoelectron dynamics: It defines the cutoff of rescattered electrons and it shapes the time–energy relation for electron recollision. To investigate this, we exploited the ADK-SM calculations to analyse the final absolute momentum acquired by the electron after photoionisation as a function of the recollision phase. In the following discussion we will refer to revisit to describe passages of the electron nearby the cation on a relatively large spatial scale, where momentum transfer is relatively small and soft, whereas recollision, or rescattering, refers to the close approach of the electron to a nucleus, with an associated large momentum transfer, e. g., in back scattering. While multiple revisits may occur during the interaction of the electron with its cation, a recollision event will drive the electron irreversibly away from the molecule. The resulting momentum distributions are reported in Figure 4.3d,e for perpendicular and parallel alignment, respectively. They consist of broad peaks appearing every half cycle of the electric field at phases close to $(k + 1/2)\pi$, $k = 1, 2, 3 \dots$, for which the electron collides with the molecular cation when the laser field’s vector potential is maximum. The first recollision event, i. e., the first peak in Figure 4.3d at a phase of $3\pi/2$, allows the electron to reach the largest momentum as expected from the classical theory⁷³. This is close to the maximum asymptotic kinetic energy, i. e., the $10 U_p$ cutoff. The peaks appearing later correspond to electrons that have initially missed and then revisited the ion at later times. These subsequent rescattering events are expected to lead to lower photoelectron energies⁷³. At the same time, these multiple revisits are possible only due to the Coulomb attraction of the ionised molecule⁷³. Since the current understanding and analysis of strong-field self-diffraction experiments only consider the photoelectron recollision on the first revisit^{72,112}, the relevance of Coulomb attraction is usually neglected. However, our results demonstrate that it is a crucial ingredient to correctly understand molecular-frame electron rescattering. Note that a small yield at large momentum (> 3 a. u.) is visible for both alignments at the fourth and the sixth revisit, Figures 4.3d,e. These revivals, caused by Coulomb focussing, *vide supra*¹³³, are expected to vanish for imperfect linear polarisation of the laser field, as usually occurring in any experiment. This explains why ADK-SM for parallel alignment has another cutoff around $10.7 U_p$, as well as the more pronounced cutoff around $9.3 U_p$.

in Figure 4.2i. Due to the subtle conditions of Coulomb focussing, this effect will not be further considered in the discussion below; it does not contradict any of our general conclusions.

In this framework, the largest absolute momentum for perpendicular alignment comes from the first rescattering event at a phase around $3\pi/2$, see Figure 4.3d and its inset, which yields the largest momentum ~ 3.15 a. u.. This momentum corresponds to an asymptotic kinetic energy $\sim 10.5 U_p$ and thus explains the experimental observation of the $10 U_p$ cutoff for perpendicular alignment, see the red marker in Figure 4.2c. This rescattering event is attenuated by the imprinting of the nodal plane perpendicular to the molecular axis¹¹⁷, as otherwise this first peak would not only correspond to the largest photoelectron momentum, but also to the most probable recollision event. This attenuation for perpendicular alignment is responsible for the rescattering at the third revisit, i. e., at a phase around $7\pi/2$, to play a major role at lower energies and for the build up of a secondary cutoff at $\sim 9 U_p$, Figure 4.2i. While this second distinct minimum is not clearly visible in the first derivative of the experiment and the TDDFT calculations (red curves in Figures 4.2c,f), the broad shape of the minima in Figures 4.2c,f at high energy may be in fact a signature of the attenuation of the scattering at first revisit and the relevant contribution of the third revisit. In the case of parallel alignment, instead, the first rescattering event is strongly suppressed and most of the large-momentum electrons come from the third revisit at a phase of $7\pi/2$, depicted in the inset of Figure 4.3e; the fifth revisit also yields comparable momenta. As a result, the momentum cutoff is smaller, i. e., ~ 2.9 a. u., corresponding to a final kinetic energy of $\sim 9 U_p$. This is in good agreement with the experimentally observed reduced cutoff for parallel alignment, see the blue marker in Figure 4.2c and Figures 4.2f,i. These dynamics are mainly driven by the molecular potential: Here, the node of the HOMO along the laser polarisation imprints an angle on the electron emission at tunnelling. For OCS this angle was estimated to be $\sim 30^\circ$ with respect to the longitudinal Y axis by the TDDFT calculations. This angle prevents the electron from rescattering at the first revisit. However, then the Coulomb attraction of the ionised molecule forces the electron to stay in the interaction region and to recollide at later revisits. It is important to note that the angle of emission and the rescattering at the n th revisit are strongly correlated. Indeed, larger emission angles lead to later revisits. As the consequence, the photoelectron cutoff carries a clear signature of the electronic structure at tunnelling. This angular dependence imprinted in the momentum distribution of the initial electron wavepacket leads to the breakdown¹¹⁷ of the common product ansatz in QRS¹¹⁵, where the initial and the rescattered parts of the wavepacket are separated and only the latter is considered angularly dependent in the recollision frame.

Furthermore, the photoelectron cutoff in the molecular frame carries crucial time information: While the cutoff for perpendicular alignment is strongly shaped by electrons recolliding $3/4$ of an optical cycle after ionisation, as usually assumed, this is not true for parallel alignment: The cutoff is dominated by electrons revisiting the molecule much later, namely one or multiple optical cycles later. For a wavelength of 1300 nm this corresponds, at least, to a delay of ~ 4.3 fs and it linearly increases with the wavelength. Apart from the aforementioned effects of Coulomb focussing, it is also evident from Figures 4.3d,e that even-numbered revisits yield lower kinetic energies $< 8 U_p$ ⁷³. Since the time spent by the photoelectron before rescattering is usually exploited as the elementary delay step for time-resolved self-diffraction experiments⁷², the use of this lower range of photoelectron energy^{109,112} results in any time information being smeared out on much longer timescales. Furthermore, the analysis performed here demonstrated that this delay step strongly depends on the molecular-frame alignment and that the molecular potential sets a complex time–energy encoding in the electron dynamics. This molecular-frame clock for electron recollision could clearly be exploited to disentangle the structural dynamics with few-fs or even sub-fs temporal resolution. For instance, signals from the first (few) revisit order(s) could be selected in the experiment with near-single-cycle (few-cycle) laser pulses.

We demonstrated, experimentally and computationally, that the molecular frame determines the momentum distribution of high-energy rescattered electrons in strong-field ionisation. The basic

concept of molecular-frame strong-field ionisation is captured by considering the initial conditions imposed by the molecular potential in the dynamics of the photoelectron. Furthermore, from the analysis of the rescattering trajectories it is evident that the molecular interaction plays a crucial role in setting a clock for the emission and the dynamics of high-energy electrons. It highlights that the molecular frame has a strong impact on the relation between the photoelectron energy and the rescattering time. This finding redefines the delay step of time-resolved self-diffraction experiments and opens up a new perspective on strong-field-driven photoelectron–molecule collisions. These conclusions hold similarly for other observables related to electron recollision, e. g., high-harmonic-generation spectroscopy.

Our result represents an important benchmark for any self-diffraction measurement and represents a breakdown of the usual interpretation of LIED experiments^{72,109,112}. We note that in such experiments mid-infrared lasers ($\lambda \approx 3 \mu\text{m}$) are typically employed. Since the electron's excursion length grows with increasing laser wavelengths, we expect our findings to be even more relevant for actual LIED measurements.

Our study highlights the molecular-frame conditions as a crucial ingredient of self-diffraction experiments. This framework is general and can, in principle, be extended to any molecular system. Furthermore, the molecular-frame strong-field interaction was quantitatively modelled here by a fully-interacting-electron TDDFT calculation and, in conjunction, by a semiclassical single-active-electron theory. We exploited TDDFT to evaluate the contribution of different molecular orbitals to the ionisation-rescattering dynamics as a benchmark for the applicability of the semiclassical approach. We expect this double-sided theoretical framework to become more and more important with increasing molecular complexity, where modelling the photoelectron dynamics may go beyond the capabilities of a single-orbital picture. In general, this also opens the perspective to investigate electron-correlation-driven phenomena in molecular strong-field physics¹⁰⁷. Furthermore, the earliest moments of a strong-field interaction are intrinsically imprinted in the initial conditions of the photoelectron and in the final energy distribution. Thus, molecular-frame strong-field ionisation experiments, in principle, allow one to achieve a deeper understanding of electron tunnelling, for instance, regarding the tunnelling time, and to track the molecular potential in real-time.

5 Strong laser alignment of solvent–solute aggregates in the gas-phase³

5.1. Introduction

The properties of atoms and molecules are strongly dependent on their environment. The photochemical pathways and functions of biological chromophores are, for instance, strongly affected by hydrogen-bond interactions with the surrounding protein and solvent environment^{137–139}. Hydrogen bonds in general are of universal importance in chemistry and biochemistry and it is of great interest to bridge the gap between single isolated molecules and molecules in solvation.

Indole is the chromophore of the amino acid tryptophan and indole–H₂O corresponds to a model system of a chromophore “solvated” by a single water molecule. Indole’s intrinsic properties have been widely studied^{140–142}. Also the influence of water solvation on indole has been discussed extensively, since it has a strong influence on its electronic properties¹⁴³. This includes the energetics of the lowest electronically excited states, which interchange their order with the addition of water and other polar molecules¹⁴⁴. Its emission properties are regularly used in fluorescence studies of proteins, where spectral shifts are directly related to the chromophores’ environment¹⁴⁵. The indole–H₂O dimer has a well-defined structure^{146–148}, in which water is hydrogen bonded to the N–H moiety of the pyrrole-unit. The indole–H₂O binding energy was determined to 0.2 eV¹⁴⁹.

The rotational motion of molecules can be controlled by the torque exerted on their dipole moment that is induced by the interaction of the molecule’s polarisability with external electric fields. Intense laser light, providing electric-ac-field intensities on the order of 1 TW/cm² and above, can strongly align, and in consequence spatially fix, one or two molecular axes to the laboratory frame⁴². These aligned molecules serve as ideal samples, e. g., to image the structure and dynamics of complex molecules directly in the molecular frame. This includes time-resolved dynamics studies using molecular-frame angle-resolved photoelectron spectra (MF-ARPES)¹⁵⁰ or photoelectron holography^{151,152}. In addition, as most chemical reactivity depends on the relative orientation of the reactants, aligned molecules are well suited to study steric effects in chemical reactions. Further applications of aligned molecules range from attosecond-light-pulse and high-harmonic generation¹⁵³ over ultrafast electron or x-ray diffraction^{25,27,154,155} to quantum information processing¹⁵⁶. Time-resolved diffractive-imaging experiments are of utmost interest for the recording of so-called molecular movies, which is also especially interesting for large and complex molecules. The contrast in these experiments can be greatly increased if the molecules are fixed in space, e. g., strongly aligned, typically when $\langle \cos^2\theta_{2D} \rangle > 0.9$ ^{154,157}. Strong molecular alignment in combination with tomographic approaches to observe three-dimensional diffraction volumes has the potential to retrieve the bond angles of complex molecules¹⁵⁸. The structural dynamics of the indole–H₂O system could be extracted from ultrafast electron or x-ray diffraction experiments^{27,159} on the controlled system.

Strong alignment was achieved for linear, symmetric top, and asymmetric top molecules in the adiabatic¹⁶⁰, intermediate^{43,88}, and impulsive regimes¹⁶¹.⁴ Especially the combination with

³This chapter is based on the publication S. Trippel, J. Wiese, T. Mullins, and J. Küpper, “Communication: Strong laser alignment of solvent-solute aggregates in the gas-phase,” *J. Chem. Phys.* **148**, 101103 (2018). I contributed to this work by conducting the experiment together with S. Trippel.

⁴An adiabatic response of the system to the laser field is provided if the time scales of the laser pulse are longer than the rotational period of the molecule. The impulsive regime is achieved if the pulse duration of the laser is much

rotational-state selection^{33,50} has improved the achievable control dramatically, the recorded degree of alignment reaching values as high as $\langle \cos^2\theta_{2D} \rangle > 0.97$ ⁴⁷. For the imaging of complex chemical dynamics it is highly desirable to extend the range of directionally controlled molecular systems to molecular aggregates with weak intermolecular interactions, such as hydrogen-bonded solvent–solute clusters. These systems also serve as tests for the possibilities to laser-align large biomolecules without deterioration of the secondary structure^{157,162}. Besides the generation of weak rotational coherences, corresponding to very weak alignment, in spectroscopic investigations of hydrogen-bonded clusters and even very weakly bound molecule–rare-gas clusters^{147,163–165}, so far no alignment for such systems has been reported.

Here, we report strong three-dimensional laser alignment of the prototypical indole–H₂O cluster. This enables for the molecular-frame imaging (*vide supra*) of such complex, floppy, composite molecular systems. More specifically, we present experimental results concerning the long-pulse, quasi-adiabatic alignment of the spatially-separated indole–H₂O cluster and its strong-field ionisation (SFI) MF-ARPES.

5.2. Experimental setup

The experimental setup was described elsewhere⁸⁸. In brief, a pulsed molecular beam was provided by expanding a few millibar of indole and a trace of water seeded in 80 bar of helium through an Even-Lavie valve⁸⁹ operated at a temperature of 110 °C and at a repetition rate of 100 Hz, limited by pumping speed. Due to three-body collisions in the early phase of the expansion (indole)_m(H₂O)_n clusters were formed. Using the electrostatic deflector, the molecular beam was dispersed according to the species' and quantum states' dipole-moment-to-mass ratio^{33,50,166}.

The indole–H₂O clusters were 3D aligned by a moderately intense ($I_{\text{control}} \approx 10^{11}$ W/cm²), 485 ps long laser pulse inside a velocity-map imaging spectrometer (VMIS). The rise time in intensity (10–90 %) was 100 ps⁴³. The laser pulse was elliptically polarised with an aspect ratio of 3:1 in intensity, with the major axis along the laboratory Z axis. The angular confinement was probed through strong-field multiple ionisation by a linearly polarised, 30 fs laser pulse ($I_{\text{probe}} = 3 \times 10^{14}$ W/cm²), resulting in Coulomb explosion of the cluster. The resulting ions were velocity-mapped onto a position-sensitive detector. The alignment and probe laser pulses were provided by an amplified femtosecond laser system⁸⁸. The probe pulses had pulse energies of 200 μJ and a beam waist of $w_0 = 24$ μm. The alignment laser pulses had energies controlled between 0 and 7 mJ and a beam waist of $w_0 = 30$ μm. The alignment laser itself did not ionise the molecules.

For the MF-ARPES experiments, a circularly polarised 30 fs probe pulse centred at 800 nm with a peak intensity of $I_{\text{probe}} = 1.3 \times 10^{14}$ W/cm² was used, which places the ionisation process (at peak intensity) close to the tunnelling regime with a Keldysh parameter of $\gamma = 0.7$. The circular polarisation ensures that no recollisions of the electrons with the parent ions occur. Under these conditions, the cluster undergoes only single ionisation, as confirmed by ion time-of-flight mass spectrometry.

Figure 5.1 shows the measured horizontally integrated column density profiles of the undeflected and deflected molecular beam as a function of the vertical laser position. The profiles were measured *via* strong-field ionisation of the clusters and molecules in a VMIS. The individual profiles were obtained by gating the detector on the specific parent ion masses. The undeflected molecular beam column density profile, which has the same shape for all species, is shown as a black line, whereas the deflected molecular beam column density profiles for indole and indole–H₂O are plotted in red and blue, respectively. The indole–H₂O profile is multiplied by a factor of 20 with respect to the undeflected and deflected indole signal, which reflects the relative amount of this dimer formed in the supersonic expansion. A clear separation of indole and indole–H₂O clusters was observed¹⁶⁶.

shorter than the rotational period of the molecule.

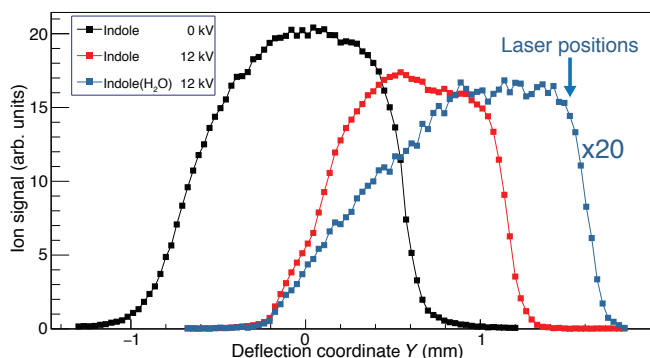


Figure 5.1: Molecular-beam and deflection profiles of indole and indole–H₂O.

Of the various species present in the molecular beam the indole–H₂O cluster possesses the largest dipole moment ($\mu = 4.4$ D)¹⁴⁸ and the largest dipole-moment-to-mass ratio, and, therefore, was deflected significantly more than the indole ($\mu = 1.96$ D) and water ($\mu = 1.86$ D) monomers^{166,167}. Similarly, higher-order clusters, (indole)_{*m*}(H₂O)_{*n*} ($m > 1 \vee n > 1$), were deflected significantly less. Thus, a pure sample of indole–H₂O was obtained and the blue arrow in Figure 5.1 marks the vertical position in the molecular beam where the alignment and MF-ARPES measurements were performed.

5.3. Results

The 2D momentum image for H₃O⁺ ions, following Coulomb explosion, for the alignment-field-free case is shown in Figure 5.2b. Clearly visible are two, a slow and a fast, ionic channels, assigned to the two Coulomb-explosion channels $C_8H_7N-H_2O \rightarrow C_8H_6N^+ + H_3O^+$ and $C_8H_7N-H_2O \rightarrow C_8H_6N^{2+} + H_3O^+$. The central part of the image was cut due to the presence of background signal in this region. The observed distribution is circularly symmetric as expected for the case of an isotropic sample and the probe-laser polarisation linear and perpendicular to the detector plane. Figure 5.2c shows the corresponding ion distribution when the molecules were 3D aligned by the elliptically polarised control laser with its major axis perpendicular to the detector plane. The pairs of red and cyan circles indicate the velocity ranges that were used to extract the degree of alignment for the two channels. This H₃O⁺ distribution was fairly directional and provided direct evidence of the alignment of the indole–H₂O clusters at the time of ionisation. The mean of the momentum distribution of the H₃O⁺ fragments was located in the molecular plane of the indole moiety due to the planarity of the indole–H₂O cluster. Measuring its transverse momentum distribution, therefore, directly linked the molecular plane of the indole moiety to the laboratory frame.

Figure 5.2a shows the experimentally derived degree of alignment $\langle \cos^2\theta_{2D} \rangle$ as a function of the peak intensity of the alignment pulse for the slow, $C_8H_7N-H_2O \rightarrow C_8H_6N^+ + H_3O^+$, and fast, $C_8H_7N-H_2O \rightarrow C_8H_6N^{2+} + H_3O^+$, channels in red and cyan, respectively. Without alignment laser a degree of alignment $\langle \cos^2\theta_{2D} \rangle = 0.5$ was observed. With increasing laser intensity, the degree of alignment increased. It saturated for both channels at relatively moderate intensities.

Figure 5.2d shows the integrated number of H₃O⁺ ions for the two channels within the corresponding velocity cuts as a function of the alignment-laser peak intensity. For the singly-charged-indole fragmentation channel the number of ions increased along with the laser peak intensity. In contrast, it decreased for the doubly-charged-indole fragmentation channel.

Figure 5.3a shows a sketch of the MF-ARPES measurements. Indole–H₂O clusters were aligned to the YZ-plane, as described above, and singly ionised by a circularly polarised probe laser, indicated by the red spiral. The emitted electrons were accelerated by the combined static electric field in the spectrometer and the laser field, and were projected onto a position-sensitive detector. Figure 5.3b shows the recorded MF-ARPES of the aligned indole–H₂O clusters. The electron emission is suppressed along the vertical direction, clearly seen as dips in the corresponding angular

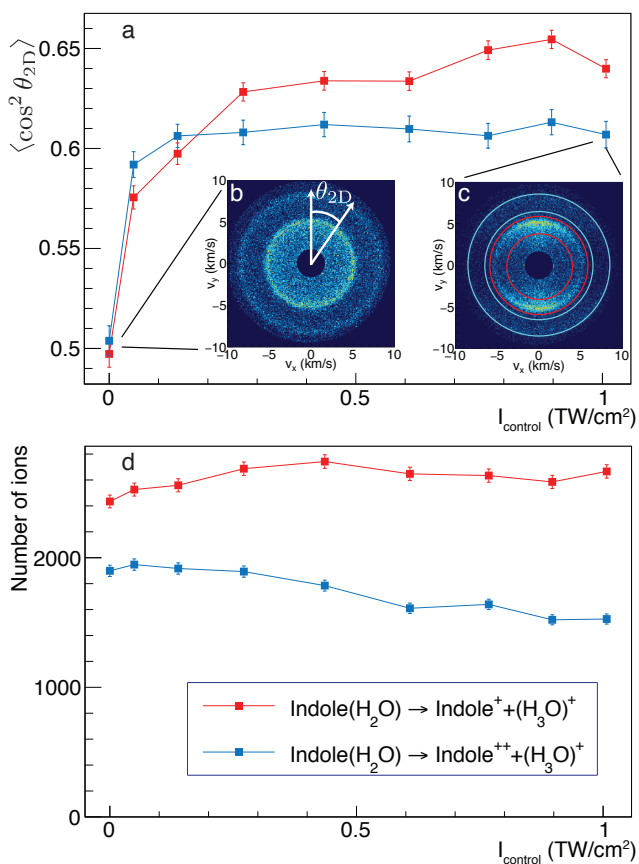


Figure 5.2: a) Observed degree of alignment of H_3O^+ as a function of the control-laser peak intensity for the fragmentation channels with singly (red) and doubly (cyan) charged indole fragments. The angle θ_{2D} is defined in b). Velocity maps b) without alignment laser and c) with alignment laser at a peak intensity of 1 TW/cm². Pairs of circles indicate the corresponding velocity cuts for the two channels. d) Number of ions for the singly (red) and doubly (cyan) indole-charge separation channel inside the velocity-selected areas.

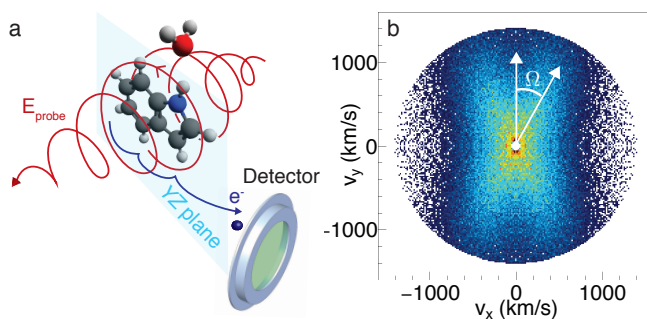


Figure 5.3: a) Schematic of the experimental setup showing the indole-H₂O cluster aligned to the YZ plane (cyan). The circularly polarised probe laser is indicated by the red spiral. b) Experimentally observed MF-ARPES of indole-H₂O.

distributions. The maximum in the off-the-nodal-plane angle in the electron emission¹⁵ occurs at an angle $\Omega = 22^\circ$ with respect to the YZ -plane.

5.4. Discussion

Indole–H₂O has a longest classical-rotation period of 484 ps. The control-laser pulse duration of 485 ps with a rising edge of about 100 ps places the alignment dynamics of the cluster into the intermediate regime between impulsive and adiabatic alignment⁴³. Different from observations for rotational-ground-state-selected carbonyl sulfide, no oscillations in the degree of alignment as a function of the delay between control laser and probe laser pulses were observed. While for every initial rotational state an oscillatory behaviour in the degree of alignment should be induced, these effects are averaged out due to the different phases of these oscillations for different initial states and the large number of initial rotational states present in the deflected part of the beam for larger molecules⁵⁰.

The observed power dependence of the degree of alignment for both channels in Figure 5.2a is similar to the typical dependence observed for a cold molecular beam⁴⁷. The degree of alignment increases strongly with increasing control-laser power until it reaches a plateau at relatively low control-laser intensities. It differs from experiments with good indicators for the degree of alignment in the actual degree of alignment of the plateau, which is given by $\langle \cos^2\theta_{2D} \rangle = 0.64$ and $\langle \cos^2\theta_{2D} \rangle = 0.61$ for the singly and doubly charged fragmentation channels, respectively. For a strongly aligned sample with good axial recoil a limit of $\langle \cos^2\theta_{2D} \rangle > 0.95$ is typically observed. On the other hand, a slow increase in the degree of alignment is usually observed as a function of the peak intensity of the alignment laser for a warm molecular beam⁶⁹. In that case, the degree of alignment does not reach the plateau region for laser intensities in the order of 1 TW/cm². Therefore, the saturation behaviour observed here is attributed to strong alignment of cold molecules and the poor representation of this alignment is attributed to nonaxial recoil in the molecular frame, likely due to complex, possibly slow, fragmentation dynamics leading to the formation of H₃O⁺.

Knowledge of the in-plane momentum distribution of the H₃O⁺ fragments in the molecular frame would, in addition, allow to determine the three-dimensional degree of alignment and orientation of the cluster by measuring the three-dimensional momentum vector. However, this is not trivial as this dynamics in the molecular frame is unknown and an analysis through complex quantum-chemical computations is beyond the scope of this publication. Moreover, as the measured degree of alignment was saturated at $\langle \cos^2\theta_{2D} \rangle = 0.64$, the directionality of this probe process is also not expected to be highly directional inside the molecular plane of the indole moiety. On the other hand, three-dimensional alignment is routinely obtained for a control-laser-pulse ellipticity of 3:1 if the one-dimensional alignment is strong^{46,168}.

The strong degree of planar alignment is supported by the recorded MF-ARPES, which contain information on the relative dipole moments, polarisabilities, molecular orbitals involved in the ionisation, and the laser-field-dependent ionisation potentials^{15,169}. The local minimum of electrons along the vertical direction results from suppression of electron emission in the nodal plane of the highest-occupied molecular orbitals (HOMO and HOMO–1)¹⁵. Instead, due to the symmetry of these π orbitals, the emission occurs off the nodal plane in the molecular frame. The suppression manifests itself by a dip along the vertical axis of the measured MF-ARPES, since the nodal plane of the molecule is strongly fixed to the laboratory frame (YZ plane). This feature appears typically, if the molecules are strongly aligned with a degree of alignment $\langle \cos^2\theta_{2D} \rangle \geq 0.9$. The measured opening angle $\Omega = 22^\circ \pm 2^\circ$ is in good agreement with the theoretical value of $\Omega_{\text{theo}} = 20^\circ$ obtained within the extended strong-field ionisation model¹⁵ using a computed ionisation potential of the cluster of $I_p = 7.71$ eV (MP2/6-311G^{**}). Rotating the major axis of the ellipse of the control-laser polarisation with respect to the detector allowed to retrieve the three-dimensional MF-ARPES of

indole–H₂O by tomographic reconstruction methods, similar to previous work for naphthalene⁸⁴. Preliminary analysis of this data further confirms this argument.

The limit of the measured degree of alignment for the slow channel is higher than for the fast channel. This is surprising, as the velocity for the doubly-charged-indole channel is faster and thus better axial recoil is expected. We attribute this behaviour to a change in the branching ratios of both channels as a function of the peak intensity of the alignment laser. The faster channel is suppressed in the strong field compared to the slow channel, see Figure 5.2d. This signal decrease might be attributed to the symmetry plane of the involved orbitals, which leads to a reduced ionisation probability when the molecular frame is fixed to the laboratory frame (*vide supra*). For the most-strongly-aligned molecules, situated and probed at the peak of the alignment laser intensity distribution, multiple ionisation is suppressed and they are preferentially observed in the slow channel. This leads to a faster saturation effect in the measured degree of alignment from the doubly-charged-indole channel as a function of the laser intensity. The degree of alignment deduced from the singly-charged-channel is still slightly increasing due to the actual increase in the degree of alignment.

One could speculate that the cluster might be destroyed by the control laser itself. A possible neutral destruction mechanism would lead to a reduction of the H₃O⁺ Coulomb explosion channels, as the pulse duration of the control laser is relatively long compared to a typical dissociation timescale. However, the constant number of H₃O⁺ fragments for the whole range of control-laser intensities indicates that the clusters are not destroyed by the alignment laser. This is consistent with a small probability expected for a transition of a bound state to the continuum wavefunction, which leads to a highly inefficient direct fragmentation of the cluster in the electronic ground state by the absorption of a single photon at the wavelength of the alignment laser. In addition, while electronically excited states of indole–H₂O could break the cluster by a charge transfer in the A''($\pi\sigma^*$) state¹⁴³, the three-photon transition probability to populate these states by the alignment laser is very small¹⁷⁰. Moreover, the laser-induced Stark effect, which is on the order of a few meV for the alignment laser intensity, is not relevant for breaking the intermolecular hydrogen bond in the cluster, which is bound by 0.2 eV.

5.5. Conclusions

Hydrogen-bound indole–H₂O clusters were strongly quasi-adiabatically aligned by moderately strong, elliptically polarised laser pulses. Alignment was observed in velocity-map images of H₃O⁺ fragments, albeit only a weak degree of alignment, $\langle \cos^2\theta_{2D} \rangle = 0.64$, could be deduced, which is attributed to nonaxial recoil in the underlying Coulomb explosion. Much stronger alignment, $\langle \cos^2\theta_{2D} \rangle \geq 0.9$, was deduced from a clearly visible nodal plane in the molecular-frame photoelectron angular distributions. This strong control opens up possibilities to study the photo-induced ultrafast chemical dynamics around the intermolecular hydrogen bond¹⁷¹ through the imaging of half-collisions in the molecular frame, which could provide unprecedented details on these intermolecular interactions.

The current results highlight that the determination of molecular axes through fragment recoil does not always lead to the correct determination of the degree of alignment in the laboratory frame. Reconstructing the MF-ARPES from the recoil frame distribution is, therefore, not possible for such systems. Our findings underline the advantage of active laser alignment, in which the laser polarisation fixes the molecular frame to the principal axes of polarisability. However, a possible influence of the alignment laser on the investigated dynamics has to be considered. Field-free alignment using shaped laser pulses could provide the best possible solution, yet the application to complex, asymmetric-top molecules is still an objective of current research⁵⁵.

6 Modelling strong-field tunnel ionisation of complex molecules⁵

6.1. Introduction

Strong-field ionisation is a versatile and powerful tool for the imaging of molecular structure, allowing simultaneous access to valence-electronic topology and atomic positions with sub-atomic-unit resolution in time and space¹⁸. A generalisation of the underlying imaging techniques, which were born in the field of atomic physics, to complex biomolecular targets promises deep insights into the biochemical machinery of life and this extension is the aim of the current work.

In strong-field ionisation experiments the desired structural information can be obtained in two complementary ways: through the observation of the photoelectron itself, which is discussed in detail below, or through the burst of light that is emitted when the electron recombines with the cation, referred to as high-harmonic generation. The latter was employed in many studies on atoms and molecules unravelling valence-orbital¹⁷² and atomic structure¹⁷³, but is not discussed further in this work.

This chapter focuses on the photoelectron wavepacket as it picks up molecular structural imprints during its formation and motion in the continuum. The entire strong-field process may descriptively be resolved into three stages, which are linked through the photoelectron's propagation in the combined time- and position-dependent field that is exerted by the laser and the cation:

(i) The photoelectron is born in the continuum. Its wavefunction is shaped by the ionisation potential⁵⁹ and the nodal geometry^{15,75,118,174} of the initial bound electronic state.

(ii) Upon propagation within close vicinity to the ionised target the photoelectron wavepacket picks up additional information about the cation through interaction with its electric potential. For circularly polarised laser pulses this encounter is essentially limited to early times right after birth in the continuum and, if the target molecule is chiral, results in photoelectron circular dichroism^{175–177}. For linear polarisation, however, the photoelectron is, in first instance, quickly driven away from the molecule yet might partly return at a later time. If the momentum at return is rather small, i. e., comparable to the initial momentum distribution at birth, the wavepacket may holographically interfere with another portion of itself that does not return to the cation. Those holographic interferences encode the tunnel exit position and the initial momentum distribution of the photoelectron^{62,110,114}. However, if the recollision occurs at the maximum of the kinetic energy, namely about three times the ponderomotive potential⁷³, the photoelectron may intrude deeply into the ionic field probing the instantaneous positions of the nuclei. This process includes only a temporally narrow slice of the initial wavepacket that returns after less than one optical cycle near a zero-crossing of the laser field. It is referred to as laser-induced electron diffraction^{19,20,71,72,112}.

(iii) After both, the decay of the laser field and the escape from the cation's Coulomb potential, are completed, the photoelectron wavepacket assumes its asymptotic form in momentum space. This is the stage one can readily access experimentally. It is highly desirable to extract unambiguous information about the target molecule that was imprinted onto the photoelectron from this detectable final momentum distribution. Although attempts of inversion recipes were formulated already, building

⁵This chapter is based on the publication J. Wiese, J. Onvlee, S. Trippel, and J. Küpper, "Strong-field ionization of complex molecules," arXiv:2003.02116 [physics] (2020), under review. My contributions to this work were the formulation of the presented strong-field ionisation model, the execution of all quantum-chemical and trajectory-based calculations, the analysis of both experimental and simulated data, and the preparation of the manuscript.

for example upon the quantitative rescattering theory¹¹⁵ for the evaluation of laser-induced electron diffraction experiments, they rely on severe approximations regarding the initial photoelectron wavepacket or its continuum motion. For instance, the returning electron's momentum distribution is frequently assumed to be free of any angular modulation. But since molecular systems may give rise to rather structured initial electron waves^{15,83,117,178}, the target-dependent formation and continuum motion of the photoelectron needs to be well understood in order to come up with a general inversion technique.

During the last twenty years numerous models have been brought into being, which elegantly tackle various different aspects of strong-field physics. The numerical evaluation of the time-dependent Schrödinger equation (TDSE)^{179,180} represents the most rigorous approach among them, but remains mostly restricted to atomic systems. Further approaches to tackle strong-field ionisation of complex molecules rely on the time-dependent density-functional theory^{75,130}. They can be efficiently applied for wavelengths up to the mid-infrared regime, but so far do not allow to track the photoelectron's dynamics in the continuum.

A broad class of models building upon the strong-field approximation (SFA) in the single-active electron picture allows for the treatment of more complex targets. Those SFA-based theories commonly divide the whole process into two steps corresponding to stage (i) and stages (ii+iii) described above. In the low-frequency limit, the initial continuum wavefunction can be described by means of quasistatic tunneling theories⁵⁹, which can be step-wise supplemented to grasp nonadiabatic behaviour during tunnelling¹⁸¹ and allow for the consideration of imprints from the initial bound electronic state^{15,174}. An alternative, wavelength-independent description of the early photoelectron wavefunction can be obtained through the sub-barrier Coulomb-corrected SFA¹⁸².

The very classical nature of the electron's motion in continuum⁶¹ has stimulated several studies that rely on its decomposition into many classical trajectories. A careful analysis of these trajectories can then help to gain an illustrative understanding of intricate strong-field phenomena¹⁸³. The two most important approaches to describe the electron's phase in the continuum are the frequently used Coulomb-corrected SFA^{62,182} and semiclassical time-dependent propagators⁶³.

We note that in the vast majority of published models the cation is approximated by a point charge during the continuum propagation of the freed electron.

Here, we introduce a novel and very efficient semiclassical simulation setup. Our approach builds upon the adiabatic tunnelling theory and allows for the consideration of structural imprints from the initially occupied valence orbital. The continuum propagation of the photoelectron wavepacket is treated through semiclassical trajectories that experience the detailed, quantum-chemically exact, field of the cation.

Due to its efficiency our model is ideally equipped for disentangling the structures of even highly complex molecules through strong-field ionisation. In conjunction with a strong-control experimental scheme, which enabled a well-defined ionisation study in the molecular frame, we present a combined experimental and computational survey on the strong-field ionisation of the prototypical biomolecular building block indole (C₈H₇N), which is the major ultraviolet-absorbing chromophore of proteins³⁰.

6.2. Semiclassical model

Our description of the strong-field ionisation process employs a two-step approach: Treating the photoelectron wavefunction at birth in the continuum through quasistatic tunnelling theory allows for the analytical description of the first step, which is explained in subsection 6.2.1. Subsequently, the final wavefunction is found by sampling the photoelectron's dynamics in the combined electric field of the laser and the polarisable cation on plane-wave quantum orbits, which is depicted in subsection 6.2.2, while subsection 6.2.3 illustrates the procedure to compose the probability density of the final wavefunction from the asymptotic trajectory properties.

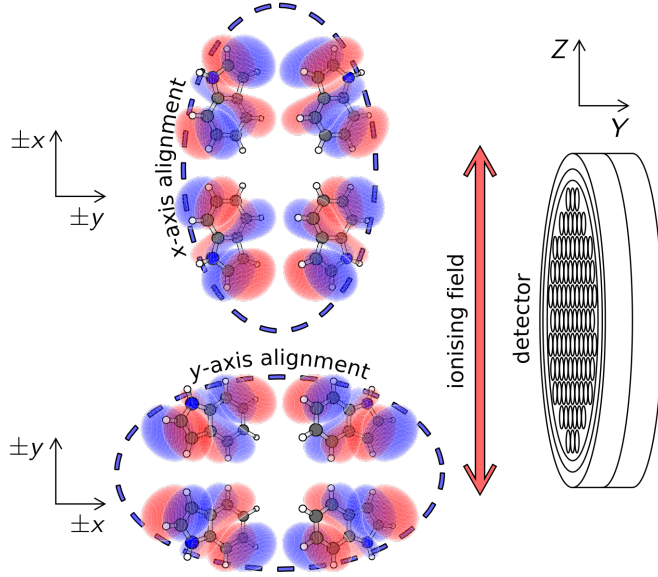


Figure 6.1: Indole molecules were three-dimensionally fixed in the laboratory frame according to two different alignments of their principal-polarisability frame, depicted on the left, with respect to the polarisation axis of the ionising laser field, depicted as double-headed red arrow. In the experiment, this was achieved through irradiation with a nonresonant laser field carrying elliptical polarisation, sketched by the blue ellipses. Both laser beams propagated collinearly along the X axis. The molecule's HOMO is shown in an isosurface representation for all four degenerate orientations.

We tested our model by simulating the photoelectron momentum distribution from metastable xenon at a wavelength of $7 \mu\text{m}$, which yielded excellent agreement with the published experimental and TDSE results⁶².

Throughout this chapter the reference coordinate frame will be set through the polarisation of the laser field, i. e., laboratory coordinate frame, with the Z axis corresponding to the polarisation axis. The molecular frame is assumed to be linked to the laboratory frame *via* the indole molecule's principal axes of polarisability, $\alpha_{xx} > \alpha_{yy} > \alpha_{zz}$. Two different molecular alignment configurations will be used, x -axis alignment with $(z, \pm y, \pm x) \rightarrow (X, Y, Z)$ and y -axis alignment with $(z, \pm x, \pm y) \rightarrow (X, Y, Z)$. Note, that the signs of x and y axes are not fixed, giving rise to four simultaneous orientations, while the sign of the z coordinate is insignificant as a result of the molecule's C_s point group. See Figure 6.1 for a scheme of all four orientations for both alignment cases in the laboratory coordinate frame.

6.2.1. Initial photoelectron wavefunction

The quasistatic Ammosov-Delone-Krainov (ADK) tunnelling theory⁵⁹, empirically extended to the barrier-suppression regime¹⁸⁴, yields the instantaneous ionisation rate w . In conjunction with the initial momentum distribution in the plane orthogonal to the polarisation axis, the probability density of the initial photoelectron wavefunction¹²³ can be obtained:

$$|\psi_0|^2 \propto w(t) \cdot \eta^2(t, p_X) \cdot \xi(t) \cdot e^{-\xi(t) \cdot (p_X^2 + p_Y^2)}. \quad (6.1)$$

$\xi = \sqrt{2I_p}/\epsilon$ is the ratio of the initial state's characteristic momentum, i. e., the square root of twice the ionisation potential I_p , and the instantaneous field strength ϵ . η represents the electronic-structure imprint of the ionised molecular orbital onto the momentum distribution of ψ_0 and can be acquired by linking the momentum in the bound state \vec{k} to the continuum momentum at the tunnel exit \vec{p} *via* the temporal saddle point equation¹²³:

$$\begin{aligned} k_X &= p_X \\ k_Y &= p_Y \\ k_Z &= p_Z + A_Z(t_s) = \pm i \sqrt{2I_p + p_X^2 + p_Y^2}. \end{aligned} \quad (6.2)$$

Here, $A_Z(t_s)$ is the Z component of the vector potential at the complex saddle-point time t_s . Subsequently, the corresponding molecular electronic structure factor can be reorganised to the form $\eta \cdot e^{i\Delta\phi_0}$, with η providing a momentum imprint onto ψ_0 and $\Delta\phi_0$ introducing an initial phase offset.

A simplified description of the highest occupied molecular orbital (HOMO) as a p_X orbital,

$$\begin{aligned}\psi_0 &\propto \frac{k_X}{\sqrt{k_X^2 + k_Y^2 + k_Z^2}} \\ &\propto \frac{p_X}{\sqrt{2I_p}} \cdot e^{-i\pi/2},\end{aligned}\tag{6.3}$$

results in a constant phase shift and a momentum imprint

$$\eta(t, p_X) = \frac{p_X}{\sqrt{2I_p(t)}}.\tag{6.4}$$

Within the scope of this model description it is sufficient to draw tuples of (t_0, p_{0X}, p_{0Y}) from $|\psi_0|^2$ to get complete sets of initial phase-space coordinates, since the tunnel exit \vec{r}_0 and p_{0Z} can be unambiguously inferred.

\vec{r}_0 is deduced from the field-direction model¹⁸⁵ and the corresponding momentum component along the polarisation axis, p_{0Z} , can be accessed with the aid of the adiabatic tunnelling theory embodying the first nonadiabatic correction¹⁸¹. Within the barrier-suppression regime the immanent excess energy is transformed into additional longitudinal momentum¹⁸⁵.

Finally, starting from the instant of birth, the plane-wave phases along the quantum orbits, which are employed to trace the wavefunction's dynamics, are given by⁶³

$$\phi(t_1) = -\vec{p}_0 \cdot \vec{r}_0 + I_p \cdot t_0 - \int_{t_0}^{t_1} \left(\frac{p^2(t)}{2} - \frac{2}{r(t)} \right) dt.\tag{6.5}$$

The second term of the integrand in the action integral of (6.5), $-2/r = V(\vec{r}) - \vec{r} \cdot \vec{\nabla} V(\vec{r})$, originates from a pure far-field description of the potential energy, $V = -1/r$. In order to also properly track the phases of those quantum trajectories that intrude deeply into the cationic potential, one would need to model both, $V(\vec{r})$ and $\vec{\nabla} V(\vec{r})$, in quantum-chemical detail. However, due to the large de Broglie wavelength of the photoelectron wavepacket under the present experimental conditions, *vide infra*, we approximate $V(\vec{r})$ by this coarse description without losing agreement with the experimental data.

6.2.2. Continuum propagation

In order to acquire the wavefunction's asymptotic probability density in momentum space, the classical equations of motion are numerically solved within the total combined electric field of the laser and the cation. For the sake of numerical efficiency, the ionic field $-\vec{\nabla} V(t, \vec{r})$ is computed at varying levels of accuracy, in three different spatial domains: At large distances from the centre of nuclear charge a multipole description of the electric field, including monopole, permanent dipole moment, and induced dipole moment, is employed, in close proximity to the nuclei the total electric field is approximated by an electric monopole with an atom-dependent effective charge, fully neglecting the field of the laser, and elsewhere the quantum-chemically exact electric field is utilised. See section 6.3 for the spatial boundaries of these domains.

In the close-proximity regime the application of Kepler's laws of orbital mechanics¹⁸⁶ to the resulting effective two-body problem allows for an analytical description of the orbital motion and provides the means to sort out trajectories that end up on stationary orbits around the ion. If

the total energy of such a two-body system is negative, recombination of electron and cation is assumed and the corresponding quantum orbit does not contribute to the asymptotic photoelectron wavefunction.

Starting from a quantum orbit's individual time of birth in the continuum, t_0 , the ordinary differential equations for position, momentum, and phase

$$\begin{aligned} d\vec{r} &= \vec{p} dt \\ d\vec{p} &= -\left(\vec{\epsilon}(t) - \vec{\nabla}V(t, \vec{r})\right) dt \\ d\phi &= -\left(\frac{p^2}{2} - \frac{2}{r}\right) dt \end{aligned} \quad (6.6)$$

are numerically integrated until the time when the laser field is fully decayed. The asymptotic momentum and the relative phase can then be obtained through Kepler's laws⁶³.

6.2.3. Asymptotic wavefunction

From the asymptotic momenta and relative phases of all available quantum orbits the probability density of the final photoelectron wavefunction in momentum space, $|\psi_\infty(\vec{p})|^2$, is then composed as follows. First, the momentum-space volume of interest is divided into bins in spherical energy coordinates:

$$\begin{aligned} U &= \frac{1}{2} (p_X^2 + p_Y^2 + p_Z^2) \\ \cos(\theta) &= \frac{p_Y}{\sqrt{2U}} \\ \tan(\varphi) &= \frac{p_X}{p_Z}. \end{aligned} \quad (6.7)$$

Subsequently, for each bin $(U_j, \theta_k, \varphi_\ell)$ the modulus of the coherent sum over all associated M_{jkl} asymptotic plane waves is computed:

$$|\psi_\infty(U_j, \theta_k, \varphi_\ell)|^2 = \left| \sum_{m=1}^{M_{jkl}} e^{i\phi_{jklm}} \right|. \quad (6.8)$$

Before generating the modulus of the bin-wise coherent sums, the complex-phase histogram may be coherently symmetrised to exploit the intrinsic symmetry of the photoelectron wavefunction; see section 6.3 for the detailed treatment of the three-dimensionally aligned indole molecule. After interpolation on a Cartesian momentum-space grid the asymptotic momentum map is then obtained through summation along the Y axis, which mimics the momentum projection in a velocity-map imaging spectrometer.

The use of spherical energy coordinates comes with three major advantages: (i) The curvatures of the bin edges resemble the shapes of the interference structures of $|\psi_\infty|^2$. (ii) The volume element scales with $p \cdot \sin(\theta)$, giving rise to larger bins with increasing radial momentum, which partly makes up for the smaller number of trajectories. (iii) The inherent energy coordinate allows for a straightforward emulation of focal-volume intensity averaging.

While (i) and (ii) result in a highly increased convergence of $|\psi_\infty|^2$ as a function of the number of samples, (iii) enables the efficient handling of a distribution of incident intensities as it is often encountered in strong-field experiments. Within a narrow range of incident intensities and in absence of electronic resonances the change of $|\psi_\infty|^2$ with respect to intensity is dominated by the ponderomotive shift of the nonresonant above-threshold ionisation (ATI) interferences⁹⁵. Those

Table 6.1: Field-free energies and irreducible representations of the four highest occupied molecular orbitals of indole. Energies were calculated at the MP2/aug-cc-pVTZ level of theory using GAMESS^{187,188}.

orbital	energy (eV)	χ
HOMO	-7.83	A''
HOMO-1	-8.24	A''
HOMO-2	-10.52	A''
HOMO-3	-12.78	A''

ATI structures represent a purely radial pattern with an energy spacing equal to the photon energy, $\hbar\omega$, between adjacent maxima. Thus, a small uncertainty in the ponderomotive energy due to focal-volume averaging can easily be emulated by introducing this uncertainty to the energy axis of $|\psi_\infty|^2$, which smears out the ATI pattern but leaves the angular structures unchanged.

6.3. Computational setup

Ionisation of the indole molecule was described as occurring from a single p_x orbital, which resembles HOMO and HOMO-1 both in energy and symmetry; see Table 6.1. Already for HOMO-2, 2.7 eV below the HOMO, the corresponding ADK tunnelling rate is roughly three orders of magnitude smaller. So contributions from all lower-lying orbitals were readily neglected.

The electric field of the ionising laser was defined as

$$\epsilon_z(t) = \begin{cases} \epsilon_0 \cdot \cos^2\left(\frac{\omega t}{2n}\right) \cdot \cos(\omega t) & \text{if } |\omega t| < n\pi \\ 0 & \text{otherwise} \end{cases} \quad (6.9)$$

with a cosine-square envelope that for $n = 44$ reproduced the full width at half maximum (FWHM) of the intensity envelope of the experimental pulses. A peak electric field of $\epsilon_0 = 2.9 \times 10^{-2}$ was utilised, corresponding to the larger of the two pulse energies employed in the experiment, *vide infra*.

The ionisation potential of the molecule was computed considering Stark shifts up to second order:

$$I_p(\vec{\epsilon}) = I_p^{(0)} - \Delta\vec{\mu} \cdot \vec{\epsilon} - \frac{1}{2} \vec{\epsilon}^T \Delta\alpha \vec{\epsilon}, \quad (6.10)$$

with the field-free ionisation potential $I_p^{(0)}$ and the differences of dipole moment $\Delta\vec{\mu}$ and static polarisability $\Delta\alpha$ between cationic and neutral species. These properties were computed using the GAMESS quantum chemistry software^{187,188} at the MP2/aug-cc-pVTZ level of theory, see appendix B.1 for details. Throughout the numerical treatment, the cation was frozen in the nuclear equilibrium geometry of the neutral molecule.

Samples of initial phase-space coordinates were generated through rejection sampling¹⁸⁹ from the probability density (6.1). The tunnel-exit positions and possible additional momentum offsets along the polarisation axis in the barrier-suppression regime were obtained based on quantum-chemistry calculations using Psi4¹⁹⁰ at the HF/aug-cc-pVTZ level of theory, following the field-direction model, see appendix B.2 for details. For the laser intensity utilised, the ionisation process was found to enter the barrier-suppression regime close to the peak electric field for the x -axis alignment case. In contrast, for y -axis alignment the tunnel exit tightly follows the simple description $\vec{r}_0 = -\vec{\epsilon} I_p / \epsilon^2$ ¹⁹¹ that considers the laser field to be quasistatic during tunnelling and ignores the Coulomb distortion of the barrier.

Within a $(60 a_0)^3$ cube, centred at the molecule's centre of nuclear charge, *ab initio* quantum chemistry calculations were used to describe the electric field of the cation, see appendix B.3. This detailed modelling of the ion's field is necessary, because the indole cation experiences strong polarisation in response to the laser-electric field. Such behaviour is expected to be general for molecules with π -conjugated electrons and, thus, makes this external-field-dependent description

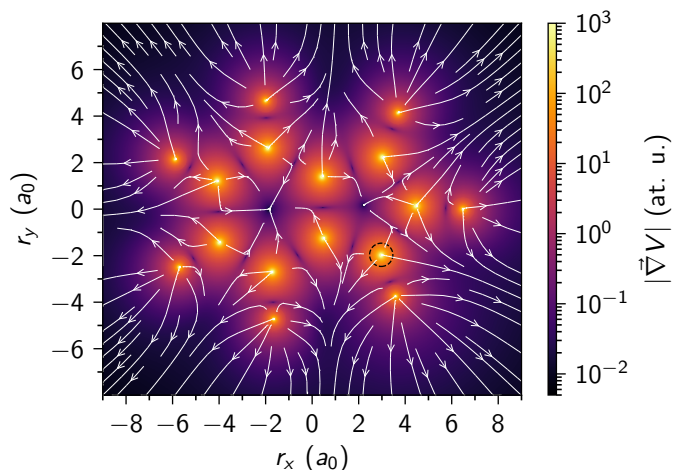


Figure 6.2: The quasistatic electric field exerted by the indole cation is shown for an external laser field $\vec{\epsilon} = 0$ for the slice in the molecular plane. Positions are specified with respect to the neutral molecule’s principal axes of polarisability. The field strength is mapped onto a logarithmic colour scale and field lines are depicted in white. The dashed black circle around the N atom illustrates the zone of influence for the two-body approximation that is employed within a radius of $0.5 a_0$ around the nuclei. For comparison, the peak electric field of the ionising laser was $\epsilon_0 = 2.9 \times 10^{-2}$.

indispensable for biomolecular systems. For both, the application of the field-direction model and the evaluation of the quasistatic field of the ion, quantum-chemical calculations were conducted beforehand for discrete positions and external fields, see appendix B.3 for details. Further values were obtained through interpolation in the semiclassical propagation setup.

At distances $< 0.5 a_0$ with respect to any of the molecule’s nuclei the total electric field was modelled using an electric monopole with an atom-dependent effective charge. For the H, C, and N atoms in indole effective charges of +1, +4 and +5 were used. These values were retrieved by finding the integer-charged monopoles that fitted the quantum-chemically exact field best on spherical surfaces with $0.5 a_0$ radius around the atomic centres. Figure 6.2 shows a slice through the total electric field that is exerted by the indole cation.

The equations of motion (6.6) were integrated following an embedded Runge-Kutta scheme with adaptive step size (Cash-Karp)¹⁹². For each alignment case roughly 5×10^9 nonrecombining quantum orbits were traced. Due to the use of the spherical energy coordinate system introduced in subsection 6.2.3 roughly 5×10^8 plane-wave samples sufficiently reconstructed all relevant radial and angular features of $|\psi_\infty|^2$.

To account for the coherent superposition of all four degenerate orientations in ψ_∞ the symmetry of ψ_∞ with respect to inversion of the X and Y axes was exploited *a posteriori* by coherently symmetrising the histogram of bin-wise coherent sums in (6.8). The X-axis symmetry is a result of the molecule’s C_s point group and the Y-axis inversion transforms two orientations into each other. The Z-axis symmetry of the aligned molecular ensemble could not be exploited in the same way, as the corresponding axis inversion would also flip the sign of the laser-electric field. As a consequence, for each of the two alignment scenarios two orientation cases were independently simulated and coherently added.

6.4. Experimental setup

The experimental setup was described in detail elsewhere^{33,75,88}. In brief, a cold molecular beam was created by supersonically expanding indole seeded in 95 bar of helium through an Even-Lavie valve³⁶, operated at a repetition rate of 100 Hz and heated to 110 °C. Using an electrostatic deflector an ultracold high-purity sample was obtained⁵⁰. Employing elliptically polarised laser pulses at a peak intensity of 1×10^{12} W/cm², which carried a saw-tooth temporal shape with a rise time of 500 ps, the molecular ensembles were aligned within the centre of a velocity-map imaging spectrometer (VMIS)¹²⁴. These alignment laser pulses, which were spectrally centred at 800 nm and had a polarisation ellipticity of 3:1 in intensity, allowed for the nonresonant, quasi-adiabatic fixation^{43,88} of the indole molecule’s principal axes of polarisability in the laboratory frame. Two

different alignment scenarios, Figure 6.1, could be realised by rotating the polarisation with a half-wave plate. The resulting degree of alignment was estimated to be $\langle \cos^2 \delta \rangle \approx 0.9$ ^{55,70}.

A second laser pulse, spectrally centred around 1300 nm with a duration of 70 fs (FWHM) and linear polarisation (ellipticity 200:1), singly ionised the molecules and photoelectron momentum maps were recorded using a high-energy VMIS. A position-sensitive detector, consisting of a microchannel-plate stack, a phosphor screen, and a high-frame-rate camera, was used for counting and two-dimensional momentum-mapping of individual electrons. To lower the impact of focal-volume averaging onto the incident-intensity distribution, intensity-difference photoelectron-momentum maps²⁹ were obtained using peak intensities of 2.5 and 3.0×10^{13} W/cm². The resulting range of the ponderomotive potential $\Delta U_p = 0.83 \hbar\omega = 0.79$ eV between these two peak intensities is still too large to resolve nonresonant ATI structures but represents a compromise between incident-intensity resolution and the amount of signal that is left in the intensity-difference momentum maps. The maximum kinetic energy at which the photoelectrons could re-encounter the cation⁷³, $3.17 U_p \approx 15$ eV, resulted in a minimum de Broglie wavelength of $\sim 6 a_0$, justifying the coarse description of the ion's potential energy in (6.5).

6.5. Results and Discussion

Figure 6.3 shows the calculated and measured asymptotic momentum maps. Each map exhibits an intense part in the centre (intensity ≥ 0.4 , yellow to orange colour), that overlaps with two relatively faint circular patterns (intensity < 0.4 , purple colour) centred on the polarisation axis at the peak vector potential, $|p_Z| = \epsilon_0/\omega \approx 0.83$.

Figures 6.3e,f show the experimentally obtained intensity-difference data sets, which clearly differ for the two alignment scenarios employed. This difference mainly manifests itself in the star-shaped angular structure of the intense central parts of the images. For the x-axis alignment case there is an angular local minimum along the polarisation axis, whereas the momentum map for y-axis alignment exhibits a maximum. Generally, the angular modulations are a lot less pronounced for y-axis alignment. Furthermore, both momentum maps show a few sharp radial maxima along the Z axis at momenta around ± 0.4 , which are easier to see in the linear-scale representation in Figure 6.4. The projected out-of-plane angles,

$$\Omega = \arctan \left(\frac{\langle |p_X| \rangle}{\langle |p_Z| \rangle} \right), \quad (6.11)$$

are 25° for x- and 24° for y-axis alignment.

The simulated asymptotic momentum distributions following irradiation through a laser pulse with a distinct temporal peak intensity are depicted in Figures 6.3a,b. The momentum maps for both alignment cases show rich radial and angular structure in the intense central parts. The radial ATI interference patterns are clearly dominant and are overall shifted in momentum between the two cases. In the high-intensity central parts of the images a star-like pattern is visible with an hourglass shape imprinted on it. Here, the projected out-of-plane angles for x- and y-axis alignment are 28° and 26° .

Figures 6.3c,d show the modelled asymptotic momentum maps with focal-volume averaging, assuming a range of the ponderomotive potential of $0.83 \hbar\omega$. Here, the ATI interferences are almost fully extinguished²⁹, which results in the star-like angular pattern becoming the dominant feature. The angles Ω are the same as those for the momentum maps at fixed laser intensity.

These phenomena in the momentum maps are linked to their respective individual sources within the complete molecular strong-field ionisation process: The inner, intense part of the asymptotic momentum distribution, which constitutes the majority of the total probability density, represents

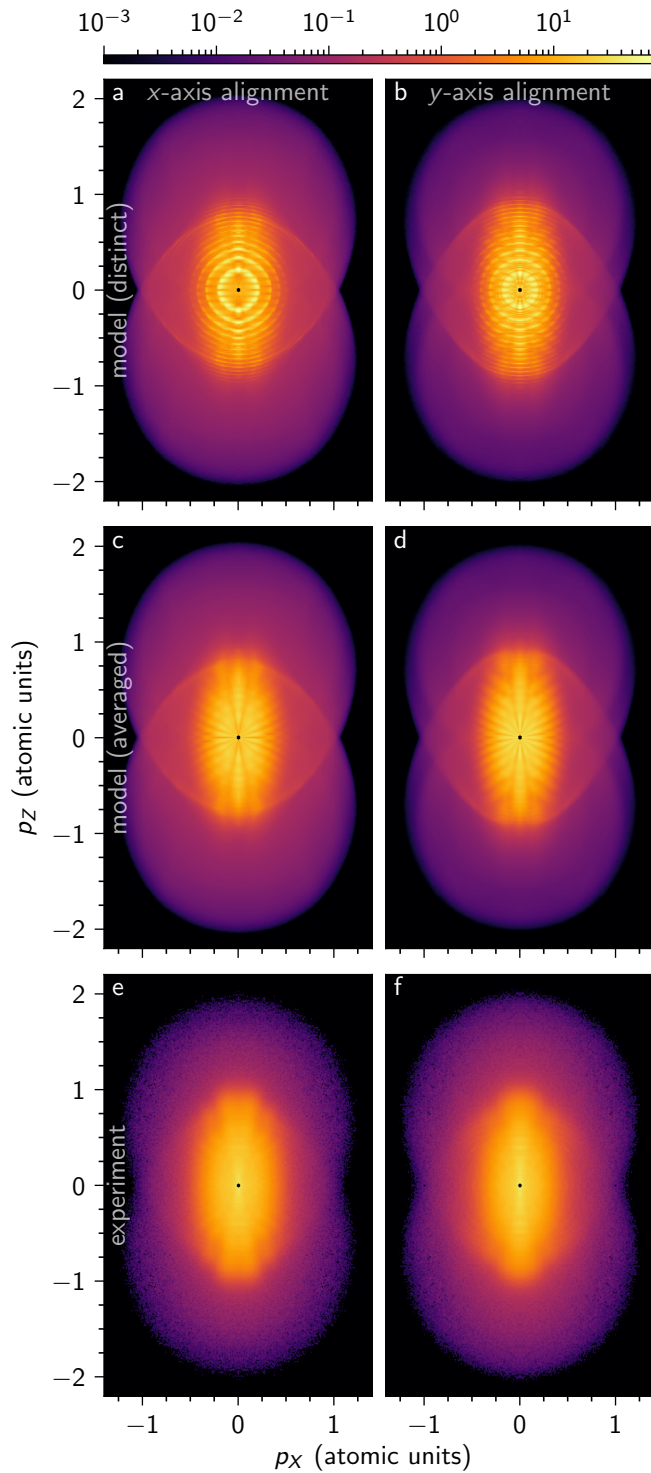


Figure 6.3: Asymptotic photoelectron momentum maps for the x-axis alignment case in the left and the y-axis alignment case in the right column. The top row shows momentum maps modelled for a distinct incident intensity and the middle row shows the corresponding maps with focal-volume intensity averaging; see text for details. The bottom row shows the experimental results. All images were normalised to their mean intensity and are displayed on a common logarithmic colour scale shown at the top. See Figure 6.4 for a zoom into the central part of the experimental data.

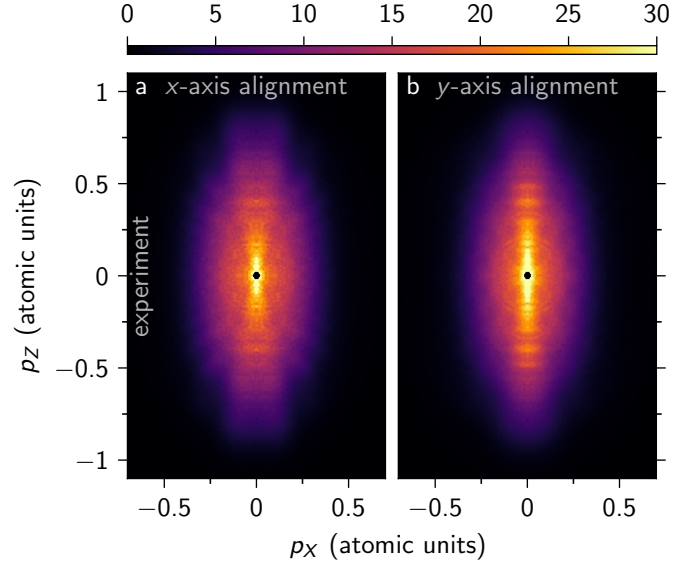


Figure 6.4: Experimentally obtained photoelectron-momentum maps for a) the x-axis alignment case and b) the y-axis alignment case. The images show a closeup of Figures 6.3e,f displayed on a common linear colour scale.

the fraction of the photoelectron wavefunction that leaves the molecule directly, i. e., without close interaction with the cationic potential. Its continuum motion is dominated by the electric field of the laser, giving rise to ATI interferences between adjacent optical cycles. However, the two rather faint, disc-like shapes in the momentum maps result from strong Coulomb interaction of a small fraction of the photoelectron wavefunction with the ionic potential upon return to the cation⁶¹. The outermost rings of these discs correspond to electron–cation recollisions at maximum momentum and carry information on the molecular geometry¹⁹³. Where the inner ellipse and the outer discs overlap in momentum space, holographic interferences can occur, which give rise to the star-like pattern observed here. This holographic fingerprint encodes both, the tunnel exit position and the initial momentum distribution of the photoelectron wavefunction⁶². The embedded hourglass, which is especially pronounced in the x-axis alignment case, results from the nodal plane imprinting onto the momentum distribution at birth and thus onto the holographic pattern.

Both the out-of-plane angle Ω and the absolute kinetic energies of the ATI interferences provide a sensitive probe of the alignment-dependent ionisation potential. While Ω is, for identical laser parameters, mainly determined by the initial transverse momentum distribution in (6.1), the energy of an ATI ring, $N\hbar\omega - I_p - U_p$ ⁹⁵, represents a direct link to the in-field ionisation threshold for a given number of absorbed photons N .

Due to their invariance towards laser-intensity averaging the sharp maxima in the radial distributions of the experimental momentum maps are ascribed to Freeman resonances, resonance-enhanced multiphoton ionization through Rydberg states^{29,93,95,97}. Conceptually, these electronic resonances cannot be grasped by our current semiclassical model.

The predictive strength of the present model, in comparison to the experimental data is very good. This is seen, for instance, by the agreement of the momentum maps from experiment and the semiclassical model incorporating the emulation of focal-volume averaging. All features encountered in the experimental data are qualitatively reproduced with comparable relative intensities. Furthermore, the trend in the out-of-plane angle is reflected by the simulations, predicting a larger angle for the x-axis alignment case, which can be ascribed to a stronger depression of the ionisation potential.

The hourglass shape in the x-axis alignment case bears the only structural deviation in a modelled momentum map with respect to its experimental counterpart: From the semiclassical simulation a local maximum in the angular distribution along the polarisation axis is predicted, while in experiment a local minimum is observed. This discrepancy is attributed to the nonperfect linear polarisation of

the experimentally used laser pulses: A decreasing degree of linearity lowers the return probability to the cation and thus the peculiarity of the holographic pattern, which carries a maximum along the polarisation axis. However, the imprint of the HOMO's nodal plane, giving rise to a minimum along the polarisation axis, remains at least as pronounced. In the limit of circular polarisation the node will be maximally distinct^{15,83}, while the holographic pattern will be fully suppressed. Although the description of initial in-polarisation-plane momenta by means of the adiabatic tunnelling theory, including the first-order nonadiabatic correction, was established for elliptical polarisation shapes close to circular¹⁹⁴, so far there is no equivalent theoretical framework that tackles just slightly elliptical polarisation shapes. In future experimental studies special attention should be paid to optimising the linearity of the laser field. This would facilitate the comparison with simulation results and moreover maximise the recollision probability with the cation, which would increase the quality of holographic structures and imprints from laser-induced electron diffraction.

6.6. Conclusions

We unravelled the strong-field photoelectron imaging of the prototypical biomolecule indole using a combined experimental and computational approach. Strongly controlled molecules and an experimental technique suppressing laser-intensity-volume averaging enabled the recording of photoelectron momentum distributions directly in the molecular frame and for a well-defined, narrow spectrum of incident intensities. As a numerical counterpart we developed a novel, highly efficient semiclassical model that builds upon the adiabatic tunnelling theory. Both procedures revealed holographic structures in the asymptotic momentum distributions that were found to sensitively depend on the direction of the ionising field's polarisation axis in the molecular frame.

Based on the very good agreement between experiment and theory we are confident to have identified all essential molecular properties that shape the photoelectron wavepacket as it is born at the tunnel exit. Owing to the quantum-chemically exact treatment of the cation during the subsequent continuum dynamics our model is ideally suited for studies of highly complex molecular structures through strong-field ionisation and laser-induced electron diffraction. It allows to describe electron-diffractive imaging of biomolecules on femtosecond time scales while offering the opportunity to fully follow the photoelectron's motion along semiclassical trajectories. Our model description takes account of the cation's laser-induced polarisation and gives rise to a significantly faster convergence of the asymptotic photoelectron wavefunction than previously described models⁶³ due to the use of a spherical energy coordinate system. Furthermore, we sketched a clear path that leads to the simplified emulation of focal-volume averaging, enabling a direct comparison with common experimental data.

The applicability of our model is only limited by the feasibility of the quantum-chemical computation of the molecular ion and the validity of the single-active electron approximation. However, the simultaneous ionisation from multiple orbitals could be added easily and would come without any additional numerical expense.

Furthermore, our model could be used to simulate experiments involving circular polarisation, for example measurements of strong-field photoelectron circular dichroism, employing the corresponding framework of the adiabatic tunnelling theory with the first-order nonadiabatic correction¹⁹⁴.

The scattering of electrons at the quantum-chemically exact potential with the Kepler-law approximation would also be useful for trajectory-based descriptions of conventional electron diffraction off molecules, especially in the low-energy-electron diffraction (LEED) regime¹⁹⁵.

7 Disentangling strong-field multiphoton ionisation of a complex molecule through photoelectron tomography⁶

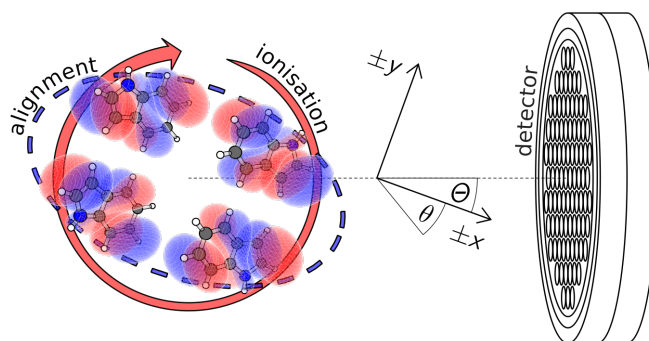
7.1. Introduction

A photoelectron that is carefully extracted and recorded may encode a variety of profound details about the atomic or molecular target it was emitted from. By thorough choice of the exact route of ionisation an experimenter can therefore determine the property of the quantum system that he or she desires to interrogate. For instance, ionising a molecule in a two-colour scheme with controllable wavelengths may provide the precise energy levels of rotational, vibrational and electronic state manifolds, if the employed laser radiation is sufficiently narrow-band¹⁹⁶. For strong-field ionisation, however, ultrashort intense laser pulses are utilised, reaching the electric field strengths that prevail within the molecule⁵⁷. In this regime, the electron is freed by a severe distortion of the binding potential well, while the exact central wavelength of the laser carrier is not crucial. There are two coexisting mechanisms that can release the electron into the continuum: by multiple rebounds off the shaking potential walls, referred to as strong-field multiphoton ionisation, or *via* tunnelling through the barrier that follows the deformation by the laser field⁵⁶. While for a given target the former effect gains importance with increasing laser frequency, giving rise to a faster motion of the distorted potential, the latter becomes dominant at high laser intensities that result in lower barrier heights^{56,57}. In the tunnelling-dominated regime the molecular electronic wavefunction can adiabatically adapt to the perturbation induced by the external laser field, which allows for an analytical prediction of the photoelectron's properties when it is born in the continuum^{59,60}. However, for ionisation occurring along the multiphoton channel, which is especially likely in the presence of resonances with excited states, the molecular system's response time is on the order of the laser-carrier period. This gives rise to classical dynamics that are believed to be rather chaotic⁵⁶. Owing to the broad spectra, that stringently follow the use of ultrashort laser pulses, such resonant excited states are ubiquitous in strong-field ionisation. The fundamental differences in the pre-escape electronic dynamics and, therefore, in the formation of the nascent photoelectron for resonant and nonresonant ionisation are still widely obscure to the scientific community. Yet many state-of-the-art imaging techniques crucially rely on strong-field ionisation, for example, tackling molecular-orbital imaging^{15,83,172} and the measurement of interatomic distances on femtosecond timescales through laser-induced electron diffraction (LIED)^{19,20,71,72,112}. Thus, it is highly desirable to illuminate and control the individual impact of resonant and nonresonant ionisation pathways for the target molecule of choice.

Here, we separate and unravel these two essential, coexisting channels of strong-field ionisation through a detailed and precise analysis of the three-dimensional molecular-frame photoelectron momentum distribution emitted from the prototypical biomolecular building block indole (C₈H₇N).

⁶This chapter is based on the manuscript J. Wiese, S. Trippel, and J. Küpper, "Disentangling strong-field multiphoton ionization of a complex molecule through photoelectron tomography," in preparation. I contributed to this work by conducting the experiment, setting up and performing the tomographic reconstruction procedures, analysing and interpreting the experimental data, and by writing the manuscript.

Figure 7.1: The indole molecule's principal polarisability frame was aligned to the laboratory frame by irradiation of elliptically polarised laser pulses, shown as blue ellipse. Ionisation occurred through circularly polarised pulses, sketched as red circle, with the arrow head indicating the helicity. Tomographic measurements were realised by the mutual rotation of both polarisation shapes about the laser beams' mutual propagation axis. The angle between the detector normal and the molecular-frame x axis defines the tomographic angle Θ and the in-molecular-plane angle θ describes the direction within the xy plane. Both angles are measured in the sense of the ionising field's helicity. The indole molecule's atomic centres and its HOMO are shown as ball-and-stick model and isosurface representation for all four degenerate orientations.



7.2. Experimental setup

The experimental setup was described in detail elsewhere^{33,88}. In brief, a cold molecular beam was created by supersonically expanding indole seeded in 95 bar of helium through an Even-Lavie valve³⁶, which was operated at a repetition rate of 100 Hz and heated to 110 °C. Using an electrostatic deflector^{33,37} an ultracold high-purity sample of indole was obtained.

The molecules were aligned by elliptically polarised laser pulses spectrally centred at 800 nm, with a saw-tooth temporal shape with a rise time of 500 ps, a peak intensity of 1×10^{12} W/cm², and a polarisation ellipticity of 3:1 in intensity. The resulting quasi-adiabatic three-dimensional alignment fixed the molecule's principal axes of polarisability in the laboratory frame^{43,45,88}, but not their directions. Therefore, we retain four simultaneously present orientations with an estimated degree of alignment of $\langle \cos^2 \delta \rangle \approx 0.9$ ^{55,70}, see Figure 7.1. The exact in-polarisation-plane angle Θ between the molecule's principal-polarisability frame and the laboratory frame was determined *via* Coulomb-explosion imaging, see subsection 2.2.2.

The aligned molecules were ionised by circularly polarised (ellipticity 1.06) laser pulses, also spectrally centred at 800 nm with a duration of 70 fs (full width at half maximum) and a peak intensity of 1.5×10^{13} W/cm². The polarisations of alignment and ionisation laser were mutually rotated about their common propagation axis by a half-wave plate to realise tomographic angles $0^\circ \leq \Theta < 180^\circ$ with 2° steps. Accordingly, the tomographic measurement of the three-dimensional momentum distribution comprised 90 two-dimensional projections that were recorded by means of a velocity-map imaging spectrometer (VMIS)^{88,124}. In total, roughly 6.3×10^7 electrons were individually detected within 5.1×10^7 shots.

Reconstruction of the full three-dimensional momentum distribution was carried out employing an algebraic reconstruction technique⁶⁴ described in subsection 2.2.1. The resulting photoelectron momentum distribution (PEMD) is the subject of the current chapter.

7.3. Results and discussion

The reconstructed three-dimensional PEMD is dominated by radial structure, resembling a spherical wave that alternates between minima and maxima as a function of radial momentum p , see the two slices in Figure 7.2. These oscillations constitute above-threshold ionisation (ATI) interferences and

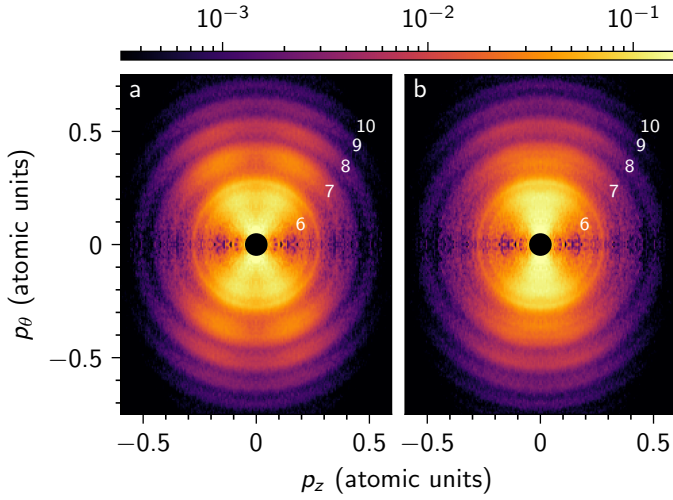


Figure 7.2: Slices through the reconstructed photoelectron momentum distribution at in-plane angles a) $\theta = 110^\circ$ and b) $\theta = 200^\circ$. The images show the first five ATI channels following the absorption of 6...10 photons. p_θ is the in-plane momentum at angle θ . Both slices are displayed on a common logarithmic colour scale. The intense part in the centre of the three-dimensional distribution is not displayed, since it does not carry useful information.

their maxima are centred at⁹⁵

$$p(N) = \sqrt{2(N\hbar\omega - I_p - U_p)}. \quad (7.1)$$

N and ω represent the number of absorbed photons and the central circular frequency of the laser field, whereas $I_p \approx 7.5$ eV is the vertical ionization energy of indole and $U_p = 0.9$ eV is the ponderomotive potential of an electron in the circularly polarised electric field at the peak intensity. The PEMD exhibits five broad radial peaks, which we assign to the absorption of $N = 6 \dots 10$ photons based on (7.1).

Regarding its angular shape the momentum distribution comprises two superimposed bodies that differ with respect to the in-plane angle θ , defined in Figure 7.1, and the out-of-plane angle

$$\phi = \arctan \left(\frac{|p_z|}{\sqrt{p_x^2 + p_y^2}} \right) \quad (7.2)$$

that describes the angle out of both the molecular plane and the laser polarisation plane. Centred around $\theta = 110^\circ$ the first contribution emerges, see Figure 7.2a, which carries a node within the molecular plane, at $p_z = 0$, while in the second one at $\theta \approx 200^\circ$, Figure 7.2b, such a nodal imprint is absent.

On top of the relatively broad ATI structures there are sharp radial features imprinted. For instance, the 6-photon channel obviously carries two of these sharp features, at $p \approx 0.2, 0.25$, and the 7-photon channel bears another one at $p \approx 0.35$, which is especially visible in Figure 7.2b. We ascribe the first sub-unit of the momentum distribution, which peaks at $\theta = 110^\circ$, to nonresonant multiphoton ionisation and the second sub-unit, which peaks around $\theta = 200^\circ$ and comprises the sharp radial features, to resonance-enhanced multiphoton ionisation (REMPI) through electronically excited $1\pi\pi^*$ states¹⁹⁷, respectively.

Although the nonresonant and the resonant part of the PEMD overlap both in radial momentum and in-plane angle, they can be widely separated by exploiting their different occurrences at small out-of-plane angles. In Figure 7.3, the photoelectron kinetic energy spectra are plotted as a function of θ for $\phi \geq 7^\circ$ and for $\phi < 7^\circ$. At large out-of-plane angles, shown in Figure 7.3a, the spectra are dominated by nonresonant ionisation, resulting in in-plane-angle maxima around $110^\circ(290^\circ)$, whereas at small out-of-plane angles, shown in Figure 7.3b, almost exclusively contributions from resonant ionisation occur that peak at in-plane angles of $20^\circ(200^\circ)$. This separation in θ can be especially appreciated for the second and third ATI channel, while for the first one nonresonant and

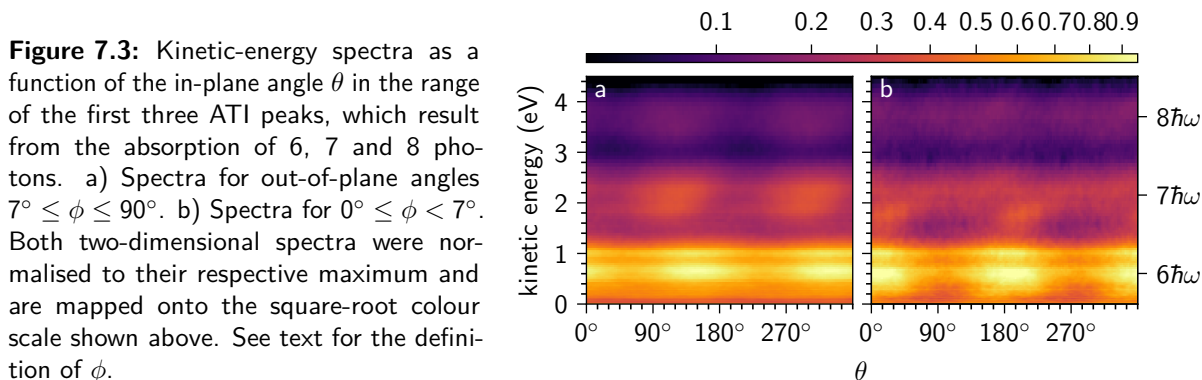
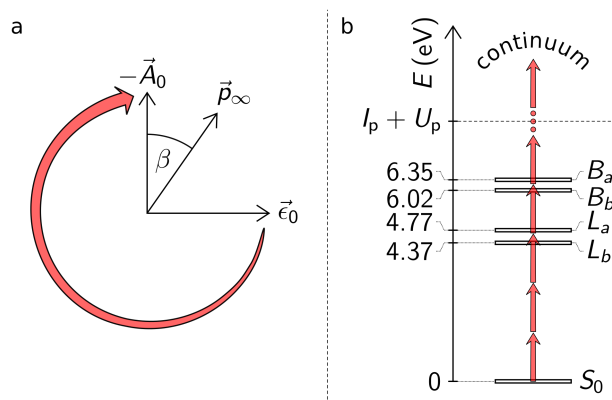


Figure 7.4: a) Illustration of the relation between the laser-electric field vector at the instant of ionisation, $\vec{\epsilon}_0$, and the asymptotic photoelectron momentum \vec{p}_∞ : In absence of Coulomb attraction from the cation, the final momentum would point in the direction of the negative vector potential, $-\vec{A}_0$, representing a rotation of 270° along the helicity of the field, sketched as red arrow, with respect to $\vec{\epsilon}_0$. The Coulomb force, however, gives rise to an additional angle β between \vec{p}_∞ and $-\vec{A}_0$ that depends on position and momentum of the photoelectron as it is born in the continuum. b) Sketch of the vertical energy structure of indole with respect to its electronic ground state S_0 . Field-free experimental energies of the L and B states were taken from¹⁹⁷. Each red arrow corresponds to the energy quantum of an 800-nm photon.



resonant ionisation contributions still overlap significantly.

Owing to the very classical nature of the photoelectron's motion in the continuum⁶¹, the in-plane component of the electron's final momentum \vec{p}_∞ can be linked to the laser-electric field vector at the instant of ionisation $\vec{\epsilon}_0$. The total time- and position-dependent force that acts on the photoelectron wavepacket is exerted by both the laser-electric field and the cation, with the former contribution being the dominant one. The laser field alone would give rise to a final in-plane electron momentum, that has an angle of 270° to $\vec{\epsilon}_0$ in the sense of the ionising field's helicity¹⁵. The Coulomb attraction with the molecular cation, however, increases this mapping relation by an angle β ⁸³, which depends on the initial position and momentum of the wavepacket as it is born in the continuum. This straightforward relation between asymptotic momentum and instantaneous electric field, which is sketched in Figure 7.4a, can be employed to gain deeper insight into the ionisation mechanism that underlies a certain portion of the final PEMD. In the present case, we observed an angle $\beta \approx 20^\circ$ and a total mapping angle of roughly 290° for all resonant and nonresonant photoelectron portions. Thus, we can attribute the nonresonant part of the PEMD at $\theta = 110^\circ$ to ionisation occurring when the electric field vector is aligned along the molecule's x axis and the resonant contribution at 200° to ionisation with the field being parallel to the y axis.

The emergence of nonresonant and resonant ionisation pathways can be unravelled through an analysis of the angular dependence of the Stark-shifted ionisation potential of indole. During one optical cycle the electric field vector $\vec{\epsilon}$ of the circularly polarised ionisation laser samples all directions in the plane of the molecule. Considering Stark shifts up to second order the molecular ionisation

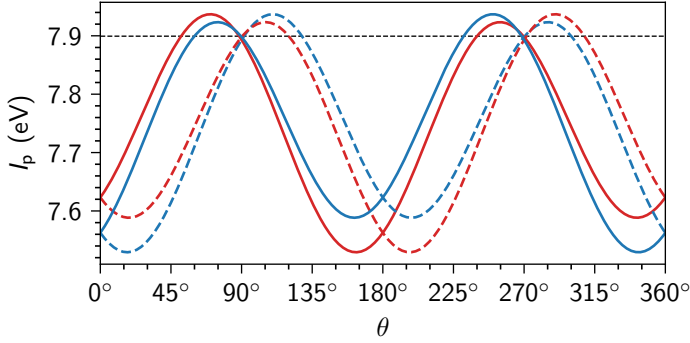


Figure 7.5: Ionisation potentials for all four orientations of indole as a function of the in-plane angular orientation of the laser-electric field vector. Stark shifts were considered up to second order. The field-free ionisation potential $I_p^{(0)} = 7.9$ eV⁹⁶ is marked as dashed black line.

T_{res} (eV)	m	n	$m\hbar\omega_{\text{res}}$ (eV)	$\pi\pi^*$ state
0.65	3	3	4.7	L_b
	4	2	6.3	(B_a)
1.0	3	3	4.9	L_a
	4	2	6.5	
1.75	3	4	4.5	
	4	3	6.0	B_b

Table 7.1: Possible assignments of photoelectron kinetic energies T_{res} to pairs of $\pi\pi^*$ -state energies that could be trespassed in an $(m+n)$ -REMPI process. The actual state in resonance possesses an energy of $m\hbar\omega_{\text{res}}$ with respect to the electronic ground state of indole. Each kinetic energy peak may be due to the resonant transition of either an L or a B state. See Figure 7.4b for the experimentally measured field-free energies of the four $\pi\pi^*$ states.

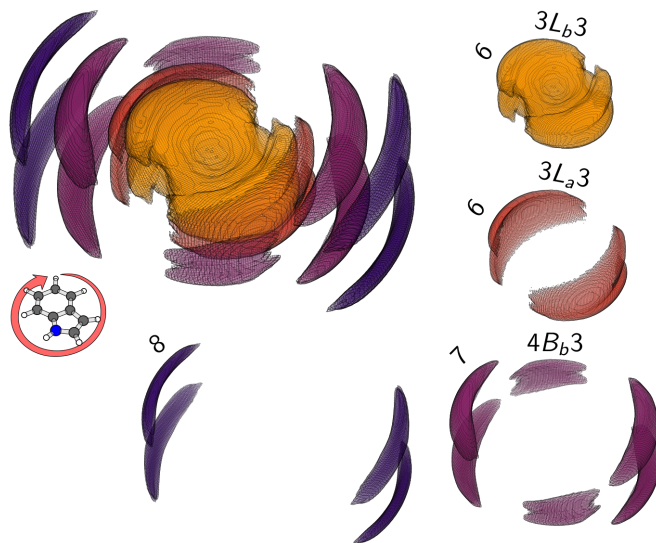
potential can be described through perturbation theory as

$$I_p(\vec{\epsilon}) = I_p^{(0)} - \Delta\vec{\mu} \cdot \vec{\epsilon} - \frac{1}{2}\vec{\epsilon}^T \Delta\alpha \vec{\epsilon}, \quad (7.3)$$

with the field-free ionisation potential $I_p^{(0)}$ and the differences of dipole moment $\Delta\vec{\mu}$ and static polarisability $\Delta\alpha$ between cation and neutral species; hyperpolarisability contributions are negligible in this intensity regime. The field-free vertical ionisation potential is $I_p^{(0)} = 7.9$ eV⁹⁶ and $\Delta\vec{\mu}$ and $\Delta\alpha$ were computed using the GAMESS quantum chemistry software^{187,188} at the MP2/aug-cc-pVTZ level of theory, see appendix B.1 for details. Figure 7.5 depicts the ionisation potentials of the four simultaneously present orientations of indole within one optical cycle of the ionising laser field. For all orientations the ionisation potential exhibits broad minima close to 0° and 180° , which give rise to maxima in the nonresonant ionisation probability and, thus, result in final in-plane photoelectron momenta around 290° and 110° . If the electric-field vector is pointing along the y axis, at 90° and 270° , the neutral molecule and the cation experience identical Stark shifts for all four orientations and I_p assumes its field-free value. This is due to the μ_y and α_{yy} components being very similar for cation and neutral molecule. We presume that also the $\pi\pi^*$ states in resonance undergo similar Stark shifts in this field configuration¹⁹⁸, which leads to equal photoelectron kinetic energies for all orientations and, thus, makes the resonances visible.

Now we inspect the resonant part of the momentum distribution to assign the electronically excited states in resonance. The first four excited singlet states of indole that are accessible through “dipole-allowed” transitions from the electronic ground state are commonly labelled L_b , L_a , B_b , and B_a ¹⁹⁹, although this nomenclature is only approximate for indole. Figure 7.4b illustrates the field-free energies of these four states in the Franck-Condon region. The resonant features of the PEMD can be seen best in Figure 7.3b at $\theta \approx 200^\circ$. Within the first ATI channel, there are two pronounced resonances at 0.65 eV and at 1.0 eV. The former shows a progression of weak echoes at 2.2 eV and 3.8 eV, corresponding to a period of the photon energy $\hbar\omega = 1.55$ eV. A third resonance appears in the second ATI channel around 1.75 eV; here the kinetic energy increases with in-plane angle. For all these cases a certain frequency ω_{res} within the spectrum of the ionisation laser resonantly populates a $\pi\pi^*$ state with m photons, followed by ionisation through n additional photons and resulting in a

Figure 7.6: Isosurface representation of the reconstructed molecular-frame PEMD showing contributions that followed the absorption of 6, 7 and 8 photons. We labelled the contributions following an $(m+n)$ -REMPI process through an excited state S as mSn . The two innermost isosurfaces render the $3L_b3$ resonant channel at a density level of 1.0×10^{-1} , shown in yellow, and the $3L_a3$ resonant channel at 7.3×10^{-2} , shown in orange. Both surfaces also contain admixtures of the 6-photon nonresonant channel. The $4B_b3$ resonant and the 7-photon nonresonant channel at 2.6×10^{-2} are both shown in purple and the 8-photon nonresonant channel at 9.2×10^{-3} is shown in dark blue. Compare Figure 7.2 for the density scale. The sketched molecule relates the isosurfaces' orientation to the polarisability frame and the red arrow depicts the helicity of the ionising field. For the sake of simplicity only one out of four orientations is shown.



kinetic energy $T_{\text{res}} = (m+n)\hbar\omega_{\text{res}} - I_p^{(0)} - U_p$. In the field-free vertical energy structure of indole the pair of B states lies one photon energy above the L -state pair. Consequently, either an L or a B state may be in resonance for each of the three cases and the specific resonantly excited $\pi\pi^*$ states cannot unambiguously be identified from the photoelectron's kinetic energy alone. Table 7.1 shows the two possible assignments of resonant-state energies to each of the three sharp peaks in kinetic energy. However, the resonant line at 1.75 eV is special due to its in-plane-angle-dependent kinetic energy. We ascribe this behaviour to the resonant transition through an excited state with a relatively shallow potential, which leads to a significant change in the nascent photoelectron's spatial distribution as a function of the exact incident frequency ω_{res} . With decreasing initial distance from the cation the Coulomb attraction grows, resulting in larger angles β . This suggests that the photoelectron line at 1.75 eV is due to intermediate excitation of the B_b state, presuming that the more loosely bound B states also possess shallower potentials than the L states. Correspondingly, we allocate the resonances at 0.65 eV and 1.0 eV to the L_b and the L_a states, respectively. The photoelectron line at 0.65 eV might in addition also contain a contribution from the B_a state.

Further insight into the ionisation pathways can be obtained from the nodal structure in the PEMD. Figure 7.6 shows isosurface representations of all resonant and nonresonant contributions that follow the absorption of 6, 7 and 8 photons. The illustration clearly conveys that resonant and nonresonant parts of the photoelectron wavepacket are emitted from the molecule in roughly orthogonal directions, i. e., they arise at different times within one optical cycle with a phase shift of $\pi/2$. All nonresonant contributions exhibit a distinct minimum in the polarisation plane, which we attribute to the imprint of the nodal plane in the HOMO that coincides with the molecular plane^{15,83}. It represents a pronounced manifestation of molecular orbital structure. While for the 6-photon ATI channel the resonant part of the PEMD overlaps with the nonresonant one, they are clearly separated for the 7-photon channel. Especially from the latter case it is evident that the resonant contribution does not carry a distinct nodal-plane imprint, in contrast to the equivalent nonresonant ionisation pathway with the same number of photons. Note, that all electronic states involved, the ground states of the neutral molecule and the cation as well as the excited L and B states, possess the same irreducible representation A'' , i. e., they all carry a node in the molecular plane. We ascribe this suppression of orbital nodal structure to an increased degree of diabaticity during resonance-enhanced ionisation: Upon passage through a resonant state, the response of the

molecule's electronic wavefunction to the external field slows down to the level or below of the laser carrier period of 2.7 fs. This results in rather chaotic ionisation dynamics⁵⁶ that we hold responsible for the washed-out nodal imprints in the photoelectron's momentum distribution.

This observation will help to gain control over molecular strong-field ionisation processes, empowering experimenters to shape the photoelectron wavepacket to fit their needs by setting the alignment of the molecular frame or the frequency of the ionising laser. An adiabatic and nonresonant ionisation route is advisable for the imaging of orbital structure, whereas experiments with linear polarisation, that rely on a return of the photoelectron to the cation like LIED and high-harmonic generation, could benefit from a suppression of nodal structure by deliberately driving ionisation through a resonant excited state⁷⁵.

7.4. Conclusions

Three-dimensional photoelectron-momentum imaging has been conducted in the molecular frame of the prototypical biomolecule indole. In the tomographically measured photoelectron momentum distribution, contributions from resonant and nonresonant multiphoton ionisation could be clearly separated and traced back to their respective instants of ionisation within the optical cycle of the laser carrier. Thus, we could shine some light on the emergence of competing resonant and nonresonant strong-field ionisation pathways: While the resonant part of the photoelectron wavepacket revealed the energy levels of three trespassed $\pi\pi^*$ states and gave insight into the shapes of these states' electronic potentials, the nonresonant contribution was found to reliably probe the nodal structure of the ground-state highest occupied molecular orbital. We attribute the absence, or at least strong suppression, of such nodal-plane imprints for all observed resonant ionisation channels to the onset of diabaticity and chaotic dynamics during the ionisation process.

Our findings are highly relevant for strong-field-ionisation surveys that aim at either the imaging of valence-electronic topology or the measurement of interatomic distances through LIED. In the former case, the resonant transition through any intermediate state should be avoided in order to obtain the clearest possible image of the nodal structure. However, for molecular-frame LIED experiments it would be advantageous to suppress the nodal imprints in the nascent photoelectron wavepacket by carefully controlling the exact ionisation pathway. In LIED experiments the freed photoelectron is accelerated in a linearly polarised laser field and steered back to recollide with the cation, giving rise to an elastic scattering signal that can be used to measure interatomic distances. Thus, a controlled suppression of nodal structure would lead to two major benefits: It would increase the probability for the electron to return to the ionic target, resulting in an amplified scattering signal, and it would facilitate the interpretation of the diffraction pattern due to a reduced complexity of the recolliding electron wavepacket.

Moreover, our work demonstrates that molecular-frame tomographic photoelectron imaging employing circular polarisation is a powerful tool to investigate the properties of electronically excited states. Since it offers access to the time of ionisation within the laser cycle and provides information about the shape of electronic potentials, it is ideally suited for the interrogation of ultrafast molecular dynamics in a pump-probe scheme.

8

Conclusions and outlook

The purpose of this doctoral work was to follow and decipher the signatures of various kinds of molecular structure as they emerge during the interaction with an intense laser field in the course of strong-field photoelectron imaging. The corresponding efforts were undertaken in order to approach the ultimate goal of realising the *quantum molecular movie*.

In brief, the previous chapters describe the accomplishment of the following objectives. As reported in chapter 3, a method could be introduced to refine strong-field ionisation imaging in general, purifying the measured photoelectron momentum images of carbonyl sulfide (OCS) and thereby granting access to the strong-field ionisation of this molecule in quantum-mechanical detail. The study depicted in chapter 4 unravelled the dynamics of photoelectron–molecule collisions during strong-field ionisation of laser-aligned OCS molecules, illuminating the impact of molecular-orbital nodal structure and providing crucial input for the realisation and interpretation of time-resolved laser-induced electron diffraction (LIED) experiments. In chapter 5, it is demonstrated how to obtain a pure and strongly controlled sample of indole–H₂O, enabling molecular-frame photoelectron imaging of this prototypical snippet of a solvated protein. The last two surveys, presented in chapters 6 and 7, shed light on strong-field ionisation of complex molecules through both experimental and computational investigations on molecular-frame photoelectron imaging of indole. It is examined how the structural complexity of this molecule affects both the initial ionisation step and the subsequent photoelectron–molecule collisions. Furthermore, the differences in the encoding of structural information for resonant and nonresonant ionisation pathways are illuminated, advancing the understanding and control of valence-electron and self-diffractive imaging of complex molecules.

In the following, a more detailed summary of the achieved objectives throughout this work is presented along with a prospect of possible future extensions.

8.1. Molecular strong-field photoelectron imaging

In chapter 3, experimentally acquired three-dimensional photoelectron momentum distributions (PEMDs) are presented that were recorded after strong-field ionisation of OCS at various, finely spaced laser peak intensities. A theoretical description of intensity focal-volume averaging for pulsed laser beams is introduced, which was fully developed within this doctoral work and which provided the framework to extract the molecule's response to distinct incident intensities. It is demonstrated that such incident-intensity resolved photoelectron measurements are essential to draw reliable conclusions about the strong-field ionised molecular target. Thereby, contributions from nonresonant above-threshold ionisation (ATI) and resonance-enhanced multiphoton ionisation (REMPI) through *Rydberg states* could be clearly separated and individually analysed.

Owing to the intensity-difference approach employed, the nonresonant photoelectron signals could be assigned to their respective numbers of absorbed photons and the dominant orbital angular momentum quantum numbers were deduced. This allowed to confirm the validity of an empirical rule, that relates the initial state's angular momentum and the minimum photon expense to ionise an ac-Stark shifted atomic system to the observable dominant photoelectron momentum, for the molecular target OCS. In addition, the *closing* of ionisation channels with increasing incident intensity could be clearly demonstrated, an effect that is obscured in common strong-field studies due to focal-volume intensity averaging.

The resonant features in the photoelectron spectra could be unambiguously identified as Freeman

resonances, i. e., photoelectron emission following REMPI through Rydberg states that experience ponderomotive Stark shifts and, thus, lead to intensity-independent final kinetic energies. The observation of this determining property was made possible by acquisition of the incident-intensity resolved PEMDs and enabled the robust reallocation of the resonance lines to Rydberg states, emending a previously published experimental survey, which assigned the same photoelectron lines to valence–valence transitions.

In chapter 4, a study is presented that sheds light onto the influence of molecular-orbital nodal structure on the photoelectron dynamics in linearly polarised laser fields. Strong-field ionisation of OCS through mid-infrared radiation is investigated experimentally and with a twofold theoretical approach. By laser-aligning the molecule in two different geometries with respect to the ionising laser field a strong alignment-dependence of the freed photoelectron’s recollision dynamics could be discovered.

In such a linearly polarised multicycle laser pulse, a photoelectron wavepacket from strong-field ionisation undergoes periodic oscillations, following the intense laser-electric field. This oscillatory motion gives rise to the photoelectron revisiting the molecular cation at multiple times. At each of these revisits, the electron may elastically scatter off the molecule, leading to imprints of the target’s interatomic distances in the final PEMD, if the recollision occurs at a sufficiently high momentum. In principle, such LIED experiments can provide molecular structural information with sub-atomic-unit resolution in time and space. Yet special attention must be paid, since each revisit is associated with a different time interval between ionisation and recollision. Ideally, the diffraction pattern from the first revisit is to be used for molecule imaging, because it arises at the shortest possible time after ionisation – roughly 3/4 of an optical cycle – and only this one results in a maximum final momentum, which makes its separation from contributions at later revisits possible.

Supported by trajectory-based semiclassical simulations, which were fully set up and conducted in the frame of this doctoral work, we could demonstrate that the probability for a high-momentum recollision at the first possible revisit is severely influenced by the nodal structure that is imprinted from the ionised molecular orbital onto the momentum distribution of the nascent photoelectron wavepacket. This finding constitutes a crucial aspect that must be considered in both static and time-resolved strong-field experiments that rely on recollision with the molecular ion. Thus, it is highly relevant for the determination of molecular structure by means of LIED, high-harmonic-generation spectroscopy and strong-field photoelectron holography.

In chapter 6, molecular-frame photoelectron imaging of the complex molecule indole is disentangled, with the aim to extend strong-field diffractive imaging to biomolecular targets. Ionisation of this prototypical biomolecule was approached through a combined experimental and theoretical treatment. The experiment employed both three-dimensional laser alignment and the acquisition of intensity-difference PEMDs as introduced in chapter 3, jointly resulting in a high-control experimental survey. Two different alignment scenarios were realised, which allowed for the investigation of molecular-frame-dependent target properties influencing the ionisation process.

The theoretical counterpart, which was fully developed during this doctoral work, is a novel and very efficient strong-field ionisation model building upon the adiabatic tunnelling theory and employing time-dependent semiclassical propagators. Direct comparison with the high-control experimental data allowed to identify the essential molecular properties that shape the phase-space distribution of the nascent photoelectron. The subsequent continuum dynamics of the electron were simulated using a detailed, quantum-chemically exact representation of the molecular ion in conjunction with an approximate orbital-mechanics description close to the nuclei. This treatment allows to properly model the photoelectron’s motion in close proximity to the complex molecular ion, which is crucial for the dynamics right after birth at the tunnel exit as well as for possible recollisions at later times. Such detail was found to be indispensable for modelling strong-field ionisation of complex molecules and is also unprecedented for trajectory-based ionisation models.

We are confident that this twofold approach, and in particular the detailed description of the

molecular ion in the introduced semiclassical model, will advance the imaging of molecular structure and dynamics to tackle even highly complex targets through LIED.

In chapter 7, strong-field ionisation of indole is disentangled through three-dimensional photoelectron imaging in the molecular frame. By means of tomographic imaging, the PEMD following a circularly polarised ionising field could be accessed in its full dimensionality, enabling the clear separation of REMPI and nonresonant ionisation pathways. It could be demonstrated that these resonant and nonresonant portions of the photoelectron wavepacket arise at different times within the ionising laser's optical cycle and leave in different directions within the molecular frame. The achieved angular resolution in the molecular frame and the sub-laser-cycle temporal resolution allowed for an in-depth glimpse at the fundamentals of molecular strong-field ionisation. While the nonresonant ionisation channels proved to reliably project the nodal structure of the highest occupied molecular orbital, the resonant ones were found to result in rather structureless photoelectron contributions. We attributed the absence – or at least strong suppression – of orbital nodal structure in the REMPI channels to the onset of diabatic ionisation dynamics: Upon passage through a resonant electronic state the electron motion slows down to the level of the laser-carrier period (2.7 fs), leading to chaotic dynamics that wash out structure imprints from the ionised orbital in the nascent photoelectron.

Our findings shine new light onto the complexity of strong-field ionisation in molecules and can be used to control the ionisation process in order to serve the specific aims of future molecule-imaging experiments. For imaging valence-electronic topology it is advisable to avoid the resonant transition of any higher-lying electronic state, resulting in the clearest possible image of orbital nodal structure. For LIED experiments, however, it could be advantageous to deliberately drive ionisation through one or several resonant states. This would increase the probability of the electron to recollide with the cation – due to the suppression of nodal structure along the laser polarisation axis – and could possibly lead to a less structured electron wavepacket at the moment of recollision, which would facilitate the process of retrieving interatomic distances from the resulting asymptotic PEMD. Moreover, tomographic photoelectron imaging with circular polarisation is shown to be a promising tool for the investigation of molecular dynamics, since it provides a wholistic view on valence-electronic structure, simultaneously displaying molecular-orbital nodes and energy levels of resonantly trespassed states.

Future studies could build upon several results achieved in this doctoral work to advance the field of molecular strong-field imaging. A major objective is the detailed understanding and technical improvement of LIED experiments tackling complex molecules and chemical reactions. On one hand, the unambiguous retrieval of all atomic coordinates has to be made viable for molecular targets that feature many different interatomic distances. Yet with a growing complexity of the atomic skeleton also the resulting photoelectron in such self-diffraction experiments will carry more and more structure, as could be demonstrated for indole in chapters 6 and 7. As a consequence, the relationship between a complex recolliding electron wavepacket and the arising diffraction pattern needs to be thoroughly investigated both in theory and experiment. On the other hand, LIED surveys would strongly benefit from a higher degree of control over the electron-ion recollision step. This includes controlling both the birth of the photoelectron – by setting the actual ionisation pathway – and its subsequent motion in the continuum until recollision. While an example for the former is given in chapter 7, the careful alignment of the molecular frame with respect to the ionising field, the latter could be achieved by adding another laser field of different colour or even by applying elaborate pulse-shaping schemes. This could potentially increase the probability for high-momentum recollisions with the target by orders of magnitude and, thus, bring even time-resolved LIED experiments into reach. For both, unravelling the self-diffraction process and finding appropriate schemes to shape the photoelectron's continuum motion, a detailed strong-field ionisation model such as the semiclassical simulation setup introduced in chapter 6 is indispensable.

Two possible molecular systems for such time-resolved LIED studies could be OCS and the indole-H₂O cluster, whose creation at high purity is demonstrated in chapter 5. The light-induced

dissociation of OCS at wavelengths in the ultraviolet regime²⁰⁰ could be employed to set up a simple test case for the interrogation of transient interatomic distances. The indole–H₂O system, moreover, could be utilised to check, under which conditions the relative motion of two distinct molecular moieties, i. e., indole and water, can be followed through strong-field self-diffractive imaging. Dissociation of the intermolecular hydrogen bond can be triggered by irradiation with ultraviolet light¹⁷⁰ and its observation on a femtosecond time scale promises deep insights into the fundamentals of biochemical reactions³⁰.

Furthermore, strong-field ionisation studies employing circular polarisation could be conducted in order to illuminate the structure and dynamics of biomolecular building blocks. For instance, photoelectron circular dichroism measurements could be unravelled in conjunction with the semiclassical strong-field model introduced in chapter 6, shining light on the imprinting of chiral structure onto the photoelectron wavepacket at and right after its birth in the continuum. Moreover, time-resolved photoelectron tomography experiments, imaging transient electronic structure, might reveal unseen details about the laser-triggered hydrogen-bond fission of the indole–H₂O cluster.

8.2. Further experimental campaigns

In addition to the studies presented above, I took part in several experimental campaigns with miscellaneous methods and objectives. While some of these campaigns were also carried out in the laboratories of the Controlled Molecule Imaging (CMI) group, most of them were conducted at synchrotron or free-electron laser facilities such as PETRA III²⁰¹, FLASH²⁰², the European XFEL, FERMI²⁰³ and LCLS²⁰⁴. They either served technical goals, like the access to molecular-frame information or the realisation of elaborate particle-detection schemes, or tackled molecular-physics surveys on laser-induced dissociation dynamics or the properties of microsolvated prototypical biomolecules. In the following, the outcomes of the individual campaigns will be briefly summarised in chronological order.

In an experimental survey conducted at the coherent x-ray imaging (CXI) beamline²⁰⁵ at LCLS in 2014, we three-dimensionally aligned 2,5-diiodothiophene (C₄H₂I₂S) molecules using the uncompressed output pulses of the in-house laser system. Employing Coulomb-explosion imaging (CEI), we could demonstrate the implementation of strongly aligned gas-phase samples at the full repetition rate of the free-electron laser⁴⁴. Furthermore, the equilibrium distance between the molecule's two iodine atoms could be determined through x-ray diffractive imaging²⁰⁶.

In the same year, a further study was performed in a laser laboratory of the CMI group that demonstrated the realisation of pure and three-dimensionally laser-aligned indole–H₂O clusters⁴⁵. Such highly controlled prototypes of solvated biomolecules represent ideal test cases to study the nature of hydrogen bonds directly in the molecular frame. Moreover, we made visible a nodal plane of the highest occupied molecular orbital through photoelectron momentum imaging and demonstrated that Coulomb explosion of the molecule follows nonaxial recoil. This experiment is described in detail in chapter 5.

Another campaign, accomplished in 2014 at the FLASH free-electron laser, dealt with the molecules iodomethane (CH₃I) and 2,6-difluoriodobenzene (C₆H₃F₂I), and employed CEI following inner-shell ionisation. We achieved adiabatic laser alignment and mixed-field orientation of the two molecules⁶⁶, which was imaged through the Pixel Imaging Mass Spectrometry (PI_mMS) camera^{207,208}. Moreover, the C–I bonds in both molecules were homolytically cleaved by irradiation with ultraviolet laser pulses. Observation of the subsequent dissociation dynamics revealed distance-dependent electron transfer from the methyl/phenyl moiety to the departing, multiply charged iodine atom and indicated ultrafast charge rearrangement in the phenyl radical²⁰⁹. Furthermore, a thorough post-analysis, taking into account the timing and diagnostics data of the FLASH facility, yielded an increased temporal resolution by eliminating the arrival-time jitter of the free-electron

laser pulses²¹⁰.

In 2015, I was part of an experimental team that realised photoion-coincidence measurements from core-shell ionisation of iodomethane after irradiation with extreme-ultraviolet laser pulses, which were generated with a novel high-harmonic-generation source with very high photon flux²¹¹ at the university of Jena.

A further campaign was carried out at the variable polarisation beamline P04²¹² at the PETRA III synchrotron facility in the same year. Indole molecules were inner-shell ionised at the carbon and nitrogen 1s orbitals, and the two-dimensional momentum projections of the resulting photoelectrons and -ions were recorded in coincidence. This yielded access to the molecular frame through recoil-frame reconstruction and enabled the acquisition of fragmentation-channel-resolved photoelectron spectra, which revealed photoelectron-impact self-ionisation²¹³.

Another two collaborative experiments were conducted at the FLASH free-electron laser in 2015. The ultraviolet-induced dissociation dynamics of various halomethanes were investigated through CEI after multiple ionisation by either intense near-infrared or extreme-ultraviolet laser pulses^{214–216}.

In 2016 at beamline P04 at PETRA III, we realised the acquisition of photoelectron-photoion coincidence spectra of spatially separated samples of indole and indole-H₂O after site-specific ionisation at the carbon, nitrogen and oxygen 2s edges. The data analysis is still ongoing.

Carried out at the low density matter (LDM) beamline²¹⁷ at the FERMI free-electron laser in 2016, our team could realise the field-free alignment of OCS molecules⁶⁷. The impulsive-alignment dynamics of the linear rotor were triggered using the synchronised pump laser of the beamline and were probed *via* Coulomb explosion after irradiation with the seeded free-electron laser.

In the same year, I also took part in an experimental campaign that aimed at investigating the dissolution dynamics of indole-H₂O following absorption of ultraviolet laser light. The process was supposed to be probed through site-specific inner-shell ionisation by x-ray pulses provided by the LCLS at the AMO beamline²¹⁸. Unfortunately, the experiment had to be aborted due to a machine failure of the free-electron laser.

Two further molecular-physics surveys were carried out at the FLASH facility in 2016. One tackled the fragmentation dynamics of the dications of the polycyclic aromatic hydrocarbons pyrene (C₁₆H₁₀) and phenanthrene (C₁₄H₁₀), which were initiated through extreme-ultraviolet radiation from the free-electron laser and probed with ultraviolet laser light. The other one dealt with the ultraviolet-induced ring-opening dynamics of 2(5H)-thiophenone (C₄H₄OS) probed through Coulomb explosion following inner-shell ionisation. The data sets of both surveys are still being analysed.

In 2017, we made a second – this time successful – attempt to capture the dissolution dynamics of indole-H₂O at the AMO beamline at LCLS. Analysis of the recorded data is still in progress.

I furthermore participated in an experimental campaign, conducted in a laser laboratory of the CMI group in 2018, that demonstrated a general route to achieve strong three-dimensional and field-free alignment of generic asymmetric-top molecules using picosecond pulse-shaping⁵⁵. Indole could be subjected to high spatial control through a slow, quasi-adiabatic ramp-up of the laser-electric field followed by a rapid truncation that left the molecule aligned under field-free conditions. We recorded the revival dynamics of the created rotational wavepacket and acquired momentum tomograms of several ionic fragments that resulted from Coulomb explosion after strong-field ionisation. Moreover, the achieved degree of alignment could be estimated by relating the experimental data *via* a simplified Coulomb-explosion model to rotational-dynamics calculations.

A further experiment could be realised in a laser laboratory of the CMI group in 2019, which tackled the fragmentation of pure pyrrole and pyrrole-H₂O samples upon strong-field ionisation at various laser peak intensities. Usage of the event-driven Timepix3 camera²¹⁹ enabled the acquisition of four-dimensional ion data, i. e., time of flight and three-dimensional velocity, for each laser shot. It could be shown that the presence of hydrogen-bonded water protects the pyrrole ring from breaking apart after both single and double ionisation, which occurs at moderately high laser

intensities²²⁰. At the highest intensities investigated, however, the water moiety was found to provoke enhanced ionisation, leading to an increased fragmentation compared to ionisation of the plain pyrrole molecule²²¹.

Lastly, I took part in a campaign at the small quantum systems (SQS) beamline at the European XFEL in 2019, which aimed at investigating the dissolution dynamics of pyrrole-H₂O upon irradiation with infrared laser light. The dissociation process was supposed to be observed through time-resolved photoion-photoion coincidence imaging following inner-shell ionisation by the free-electron laser at various photon energies. Although we managed to detect several delay-dependent signals in the time-of-flight ion spectra, the survey had to be aborted prematurely owing to a technical issue in the free-electron-laser infrastructure. The study is planned to be resumed in November 2020.

Appendices

A Photoelectron-dynamics calculations for OCS⁷

A.1. Numerical quantum-dynamics simulations

Numerical simulations of the full laser-induced electron diffraction (LIED) dynamics have been performed from first-principles within the time-dependent density functional theory (TDDFT)¹²⁸ framework as implemented in the real-space real-time Octopus code²²². In TDDFT, the dynamics of an interacting many-electron system is cast into the manageable problem of a fictitious non-interacting system under the effect of a time-dependent potential such that the non-interacting and the interacting systems have the same time-dependent density.

Since core electrons are expected to play a marginal role in the experiment we consider only valence electrons and account for inner-shell electrons by the effect of norm-conserving Troullier-Martins pseudopotentials. To obtain a good description of ionisation, we employed a local density approximation (LDA) functional with the average density self-interaction correction (ADSIC)²²³, which corrects the asymptotic decay and provides a first and second ionisation energy of 11.65 eV and 15.69 eV, in good agreement with experimental values²²⁴. During the simulations the nuclei are held fixed in the equilibrium positions, $r_{C-S} = 156.1$ pm and $r_{C-O} = 115.6$ pm.

The TDDFT equations are discretised in real-space with a Cartesian grid of spacing 0.4 a. u. with a cylindrical shape of radius 50 a. u. and length 260 a. u. aligned along the laser-polarisation direction. The solution of the electron dynamics is obtained by using a discretised real-time evolution with a time step of 0.08 a. u.. The calculations are performed with a 30 fs laser pulse. Complex absorbing boundaries of varying thicknesses, 40 a. u. from the caps of the cylinder and 10 a. u. on the radial borders, are placed at the edges of the simulation box to prevent spurious reflections²²⁵.

The photoelectron spectrum is calculated by collecting the flux of the photoionisation current through a spherical surface of radius 40 a. u. with the tSURFF method^{129,130}. This approach gives access to the momentum resolved photoelectron probability $I(\mathbf{p})$ from which, by integrating along the direction perpendicular to the detector, it is possible to obtain the angular distribution of the experiment: $I(p_X, p_Y) = \int dp_Z I(\mathbf{p})$.

The nonperfect molecular alignment in the laboratory frame is accounted for by sampling the relative angle θ between the laser polarisation and the molecular axis from 0° to 90° in steps of 10° , as shown in Figure A.1. This procedure requires a separate simulation for each θ . The photoelectron spectra for a given configuration, parallel or perpendicular, are obtained by averaging the photoelectron distributions $I_\theta(\mathbf{p})$ with weights $n_\theta(\theta - \theta^{\parallel/\perp}) = \exp(-\sin(\theta - \theta^{\parallel/\perp})^2/(2\sigma^2))$, $\sigma^2 = 1 - \langle \cos^2\theta_{2D} \rangle$, and $\langle \cos^2\theta_{2D} \rangle = 0.9$.

Furthermore, to account for the rotation of the molecule about the polarisation axis for parallel alignment we impose cylindrical symmetry of the photoelectron distribution about Y by averaging over ϕ : $\bar{I}_\phi(\mathbf{p}) = (2\pi)^{-1} \int_0^{2\pi} d\phi R_\phi(I(\mathbf{p}))$ with the operator R_ϕ of rotation in the X, Z plane. The final spectrum is obtained as follows:

$$\bar{I}^{\parallel/\perp}(p_X, p_Y) = \int dp_Z \int d\theta n(\theta - \theta^{\parallel/\perp}) \bar{I}_{\phi, \theta}(\mathbf{p}). \quad (\text{A.1})$$

⁷This appendix is based on the supplementary information of the publication A. Trabattoni, J. Wiese, U. De Giovannini, J.-F. Olivieri, T. Mullins, J. Onvlee, S.-K. Son, B. Frusteri, A. Rubio, S. Trippel, and J. Küpper, "Setting the photoelectron clock through molecular alignment", Nature Comm. **11**, 2546 (2020).

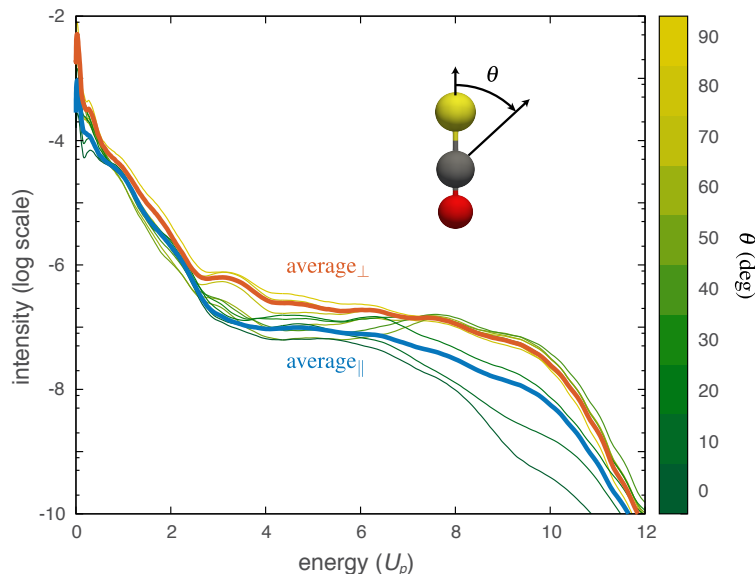


Figure A.1: Simulated photoelectron spectra as a function of the angle θ between the laser polarisation and the molecular axis. The averaged spectra for a parallel and perpendicular alignment with a degree of alignment of $\langle \cos^2 \theta_{2D} \rangle = 0.9$ are reported with thick lines.

To account for experimental background in the simulations, a constant offset of 2×10^{-8} was added to the energy distributions, see Figure A.2. For comparison, the spectra for perfectly aligned configurations are reported in Figure A.3. We point out that the background correction shifts the numerically obtained cutoffs to lower energy, but does not affect the general behaviour nor the difference of the cutoffs between the parallel and perpendicular configurations.

From the numerical simulations the crucial role of the usually neglected electron–electron interaction for correctly describing the cutoff region in the parallel configuration became evident. Figure A.4a shows the decomposed contributions of the Kohn-Sham HOMO and HOMO–1 orbitals, which highlight their distinct contributions to two distinct cutoffs, which are strongly separated in intensity. In particular, the faint $10 U_p$ cutoff for the parallel case actually appears to be uniquely determined by the HOMO–1, which does not have a node along the molecular axis, whereas contributions from the HOMO were strongly suppressed by the presence of a node along the molecular axis, i. e., parallel to the laser-polarisation axis. Second, the independent particle simulation obtained by propagating the system with the Hartree, exchange, and correlation potentials frozen, mimicking the widely used single-active electron model, presents a qualitatively different picture, see Figure A.4b. In particular the contribution of the HOMO–1 is highly overestimated and for the parallel alignment the $10 U_p$ cutoff is restored, in clear contradiction with the experiment. These results also confirm the importance of the coherent interaction between different orbitals in strong-field ionisation²²⁶.

A.2. Semiclassical trajectory simulations

Semiclassical trajectory simulations were carried out employing a simplified MO-ADK (molecular-orbital Ammosov-Delone-Krainov) approach, to create the initial wavepacket, in conjunction with a classical continuum propagation in the combined laser-electric and Coulomb field of the cation.

A.2.1. Initial electron wavepacket

In general, the phase-space distribution of the initial electron wavepacket was created in a similar fashion as described before¹⁵. The ionisation probability in dependence of the instantaneous electric field was obtained through the quasistatic ADK tunnelling theory supplemented by an empirical extension to the barrier-suppression regime¹⁸⁴. Electric-field dependent ionisation potentials, $I_p(\vec{\epsilon})$,

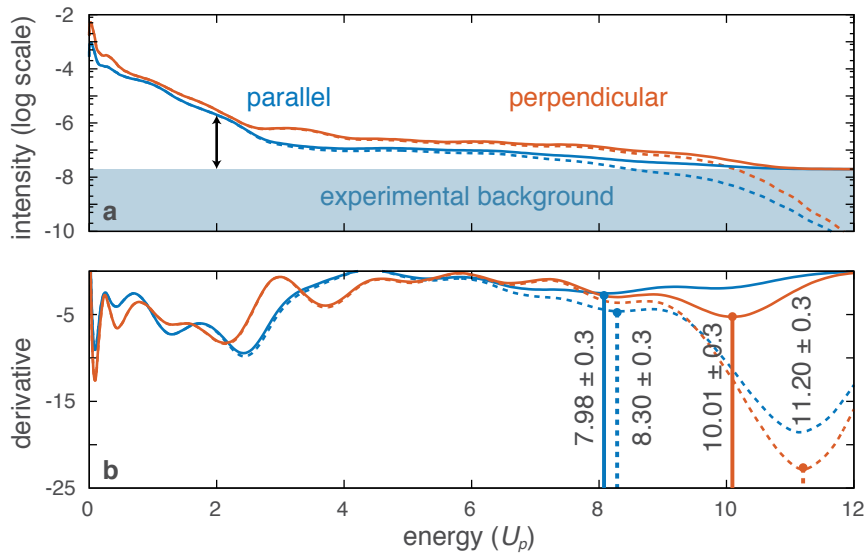


Figure A.2.: Effect of the experimental background in the simulated photoelectron spectra. **a:** Simulated photoelectron distributions, for parallel and perpendicular alignment, averaged over θ according to the degree of alignment in the experiment $I_{\parallel/\perp}(E)$ (dashed lines). A constant, 2×10^{-8} , is added to the simulated data to account for the experimental background level (solid lines), i. e., to match the experimental contrast from 2 to 12 U_p . **b:** Derivatives of the photoelectron distributions. Regardless of the presence of the background the cutoffs for the parallel and perpendicular configurations present an observable difference which is in qualitative agreement with the results of Figure 4.2 in chapter 4.

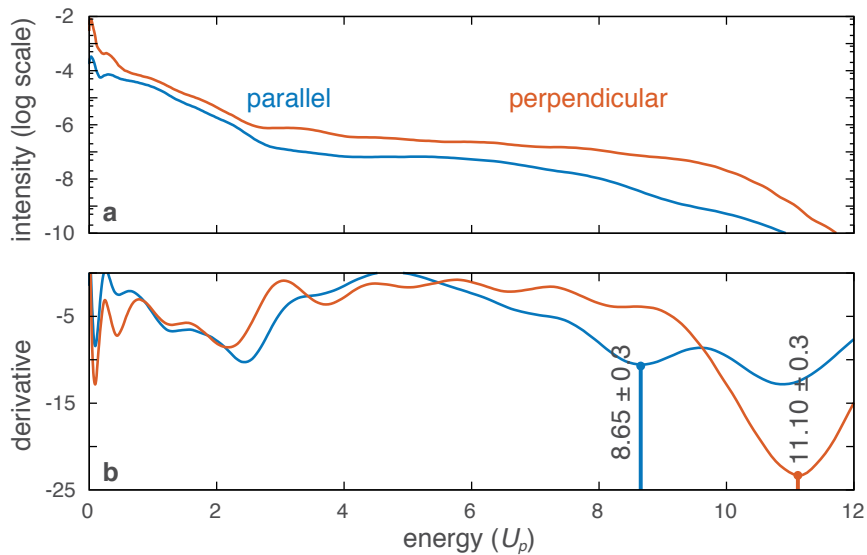


Figure A.3.: Same as Figure A.2 for perfect alignment and no experimental background correction.

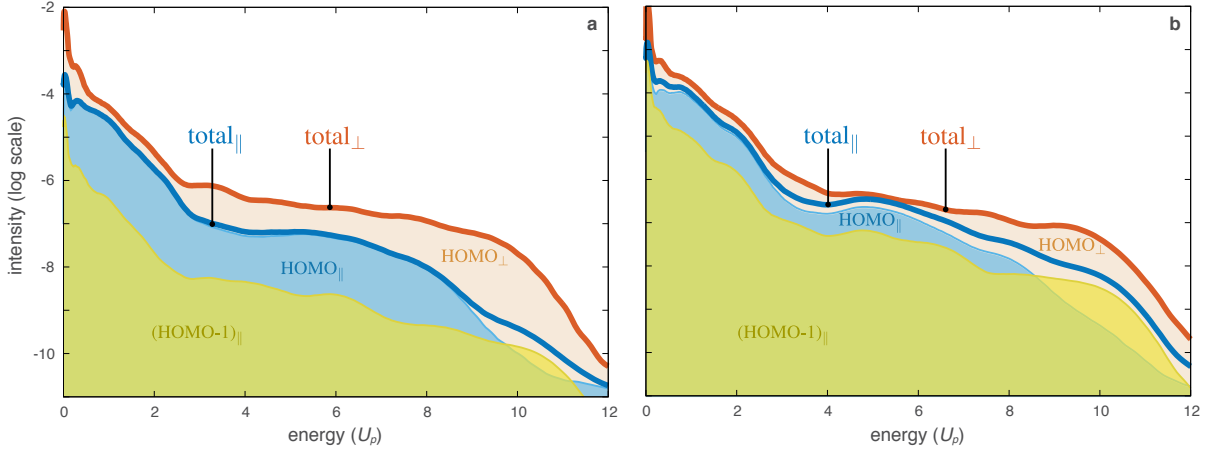


Figure A.4.: Role of electron–electron interaction and orbital contribution to the total photoelectron spectrum for perfect alignment. **a:** Spectra obtained with the fully-interacting-electrons TDDFT equations. **b:** Spectra for the non-interacting-electrons simulation obtained by freezing the Hartree exchange and correlation potentials to the neutral ground state potentials.

were computed through second-order perturbation theory

$$I_p(\vec{\epsilon}) = I_p^{(0)} - \Delta\vec{\mu} \cdot \vec{\epsilon} - \frac{1}{2} \vec{\epsilon}^T \Delta\alpha \vec{\epsilon}, \quad (\text{A.2})$$

assuming that ionisation occurs exclusively from the HOMO, as supported by the TDDFT results. $I_p^{(0)}$ is the field-free ionisation potential, $\Delta\vec{\mu}$ and $\Delta\alpha$ are the differences of dipole moment and polarisability tensor between cationic and neutral species, respectively. Here, the measured field-free ionisation potential of $I_p^{(0)} = 11.19$ eV²²⁴ was used in combination with calculated neutral and cationic dipole moments and polarisabilities¹⁵. In Figure A.5 the resulting time-of-birth distribution of a typical electron wavepacket is shown.

The classical tunnel exit was composed as $\vec{r}_0 = -\vec{\epsilon} I_p / \epsilon^2$ ¹⁸⁰. The initial momentum distribution in the plane transverse to the electric field vector at the instance of ionisation was modelled according to the atomic ADK tunnelling theory with additional imprint of the initial electronic state's nodal structure. The initial momentum component along the electric field vector was obtained through the nonadiabatic tunnelling theory¹⁸¹. For the parallel-alignment case the nodal line of the HOMO along the molecular axis imprints onto the momentum distribution at birth. Accordingly, the initial transverse momentum distribution for the parallel alignment case was described as

$$\omega_{\parallel}(p_{0,x}, p_{0,z}) \propto (p_{0,x}^2 + p_{0,z}^2) \cdot e^{-\frac{\sqrt{2I_p}}{\epsilon}(p_{0,x}^2 + p_{0,z}^2)}. \quad (\text{A.3})$$

For the perpendicular alignment case the nodal plane orthogonal to the molecular axis imprints onto the initial momentum distribution. Since it splits the HOMO's electron density unequally with a ratio of 85:15¹⁵, its imprint was described as a nodal plane with a damped peculiarity

$$\beta = 1 - \frac{|\varrho_+ - \varrho_-|}{\varrho_+ + \varrho_-}, \quad (\text{A.4})$$

with ϱ_{\pm} representing the integral electron densities on the two sides of the nodal plane. Hence, the distribution of initial transverse momenta for the perpendicular alignment case was set up as

$$\omega_{\perp}(p_{0,x}, p_{0,z}) \propto |p_{0,z}|^{2\beta} \cdot e^{-\frac{\sqrt{2I_p}}{\epsilon}(p_{0,x}^2 + p_{0,z}^2)}. \quad (\text{A.5})$$

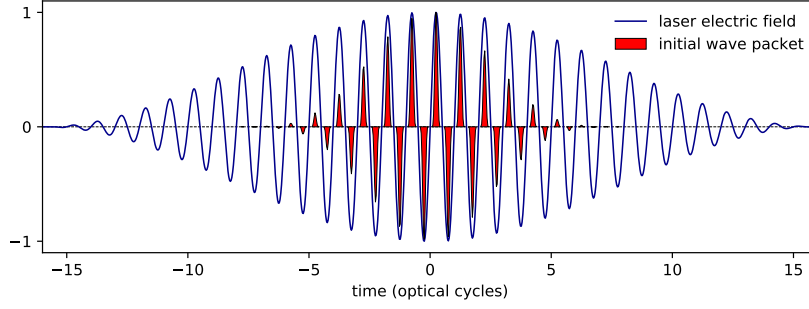


Figure A.5.: Time-of-birth distribution of an electron wavepacket for OCS at perpendicular alignment as obtained from the quasistatic ADK tunnelling theory. The distribution shown was normalised with respect to its maximum and multiplied with the sign of the instantaneous electric field. The electric field is displayed in units of ϵ_0 .

Figure A.6 illustrates exemplary transverse momentum distributions for both alignment cases.

A.2.2. Classical propagation

The electron wavepacket at birth into the continuum was sampled from the initial phase-space distribution through rejection sampling¹⁸⁹, expanded as a coherent superposition of partial plane waves and, subsequently, propagated in the combined electric laser and the cation's Coulomb field. The singly charged cation was represented by a point charge $+e$.

The asymptotic electron phase after exposure to the combined electric field of laser and point charge was obtained through⁶³

$$\phi_\infty = -\vec{p}_0 \cdot \vec{r}_0 + I_p \cdot t_0 - \int_{t_0}^{\infty} \left(\frac{p^2}{2} - \frac{2}{r} \right) dt. \quad (\text{A.6})$$

At short distances between the electron and the point charge, $r < r_{2b}$, the laser-electric field becomes negligible and the description of the electron motion reduces to a two-body problem. Here, the threshold distance, r_{2b} , was chosen such that the corresponding Coulomb field is 1000 times larger than the peak electric field of the laser. Accordingly, for the experimental peak electric field of $\epsilon_0 \approx 0.048$ a. u. this threshold distance becomes $r_{2b} = 1/\sqrt{1000\epsilon_0} \approx 0.14$ a. u.. The motion of the electron within the spherical volume of radius r_{2b} around the point charge could then be described conveniently as a Kepler orbit. This approximation allows for direct computation of the electron's properties at its symmetric exit point from the sphere: Its position and momentum vector at exit as well as its time of flight between entry and exit of this sphere can be computed fully analytically. The phase accumulated during its passage through the sphere is accessible through low-effort numerical integration. In Figure A.7 a typical trajectory of an electron is shown as it performs a swing-by around the point charge.

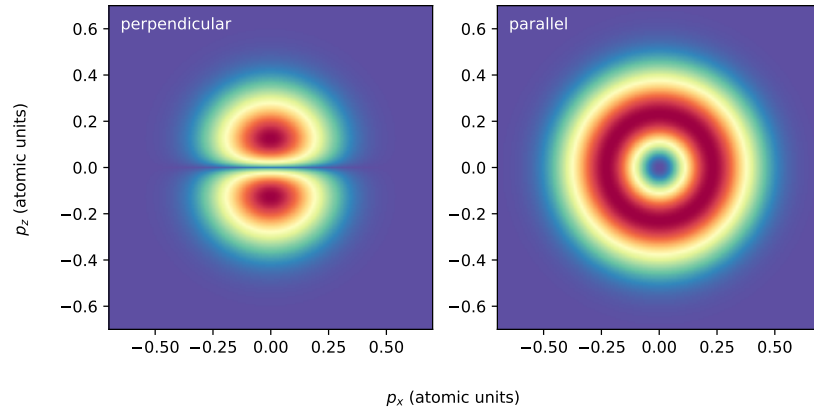


Figure A.6.: Transverse initial momentum distributions assuming the field-free ionisation potential and peak electric field.

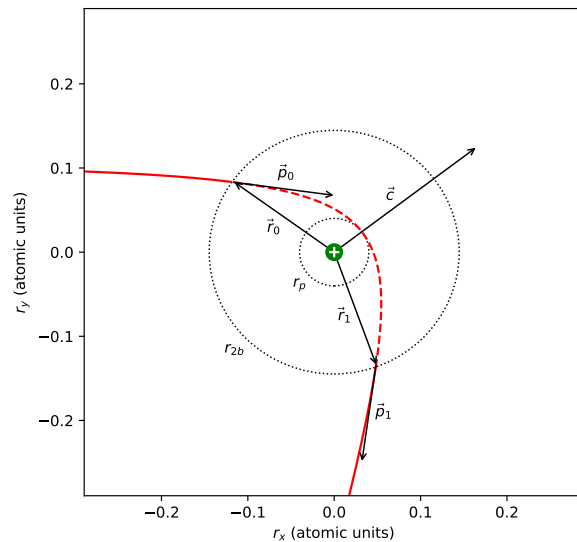


Figure A.7: Example trajectory in the combined laser-electric and Coulomb field of a point charge $+e$ (green dot), numerically propagated for $r > r_{2b}$ (solid red line) and analytically approximated for $r \leq r_{2b}$ by means of a pure two-body interaction (dashed red line). By deduction of the orbital centre \vec{c} and the distance at closest approach, the periapsis r_p , the symmetric exit position \vec{r}_1 , the corresponding momentum vector \vec{p}_1 , and the time spent within the sphere can be obtained analytically.

B Quantum-chemistry calculations for indole

B.1. Equilibrium geometry and electrostatic properties

The equilibrium geometry of the neutral indole molecule in its electronic ground state, the field-free ionisation potential, and the permanent dipole moments and polarisability tensors of the neutral and singly charged indole species were computed using GAMESS^{187,188} at the MP2/aug-cc-pVTZ level of theory. For the sake of comparability all molecular-frame dependent quantities in this section are given in the principal-axes-of-inertia frame, marked with a prime. However, all semiclassical computations in chapter 6 were performed in the principal-axes-of-polarisability frame of the neutral species, which relates to the inertial coordinate system by a rotation of $\sim 1^\circ$ within the molecular plane. Table B.1 lists the atomic coordinates in the resulting equilibrium geometry, which is in excellent agreement with previously performed calculations at CC2/cc-pVTZ level of theory²²⁷. The field-free ionisation potential was calculated as the difference of the field-free total energies of cation and neutral molecule $I_p^{(0)} = U_c^{(0)} - U_n^{(0)} = 8.29$ eV and is in reasonable agreement with the experimentally measured vertical ionisation energy of 7.9 eV⁹⁶. The permanent dipole moments of the neutral and cation ground states are

$$\vec{\mu}'_n = \begin{pmatrix} 0.5804 \\ -0.5776 \\ 0 \end{pmatrix} \text{ at. u.} = \begin{pmatrix} 1.475 \\ -1.468 \\ 0 \end{pmatrix} \text{ D}$$

$$\vec{\mu}'_c = \begin{pmatrix} 0.5043 \\ -0.5838 \\ 0 \end{pmatrix} \text{ at. u.} = \begin{pmatrix} 1.282 \\ -1.484 \\ 0 \end{pmatrix} \text{ D.}$$

$\vec{\mu}'_n$ is in excellent agreement with experimental observations^{148,228} and quantum-chemistry calculations performed at the CC2/cc-pVTZ level of theory²²⁷. The corresponding static polarisability tensors are

$$\alpha'_n = \begin{pmatrix} 135.2 & 1.678 & 0 \\ 1.678 & 104.0 & 0 \\ 0 & 0 & 59.43 \end{pmatrix} \text{ at. u.} = \begin{pmatrix} 20.04 & 0.2487 & 0 \\ 0.2487 & 15.41 & 0 \\ 0 & 0 & 8.808 \end{pmatrix} 10^{-3} \text{ nm}^3$$

$$\alpha'_c = \begin{pmatrix} 240.9 & 38.56 & 0 \\ 38.56 & 105.3 & 0 \\ 0 & 0 & 49.55 \end{pmatrix} \text{ at. u.} = \begin{pmatrix} 35.70 & 5.717 & 0 \\ 5.717 & 15.61 & 0 \\ 0 & 0 & 7.344 \end{pmatrix} 10^{-3} \text{ nm}^3.$$

The isotropic polarisability of the neutral species, $\text{tr}(\alpha'_n)/3 = 14.75 \cdot 10^{-3} \text{ nm}^3$, is in good agreement with previous quantum chemistry results²²⁹.

Table B.1: Calculated equilibrium geometry of the neutral indole molecule in its electronic ground state. The coordinates are given in the principal-axes-of-inertia frame. All atoms lie in the $z' = z = 0$ plane. The same atomic coordinates were used for the description of the indole cation during the semiclassical computations presented in chapter 6.

atom	$x' (a_0)$	$y' (a_0)$
H	-1.63636368	-4.70545460
H	3.58872958	-3.72370591
C	-1.70598994	-2.67828958
N	2.97003095	-1.96352911
H	-5.69874287	-2.47547107
C	0.48927801	-1.23389474
C	-3.96874576	-1.41779943
H	6.47657970	0.01897324
C	4.46491778	0.14961937
C	0.43239953	1.40456632
C	-4.06841347	1.22748802
C	3.02186149	2.24100201
H	-5.87322058	2.15064840
C	-1.89699453	2.63858746
H	3.69143191	4.14478991
H	-1.98733273	4.66494838

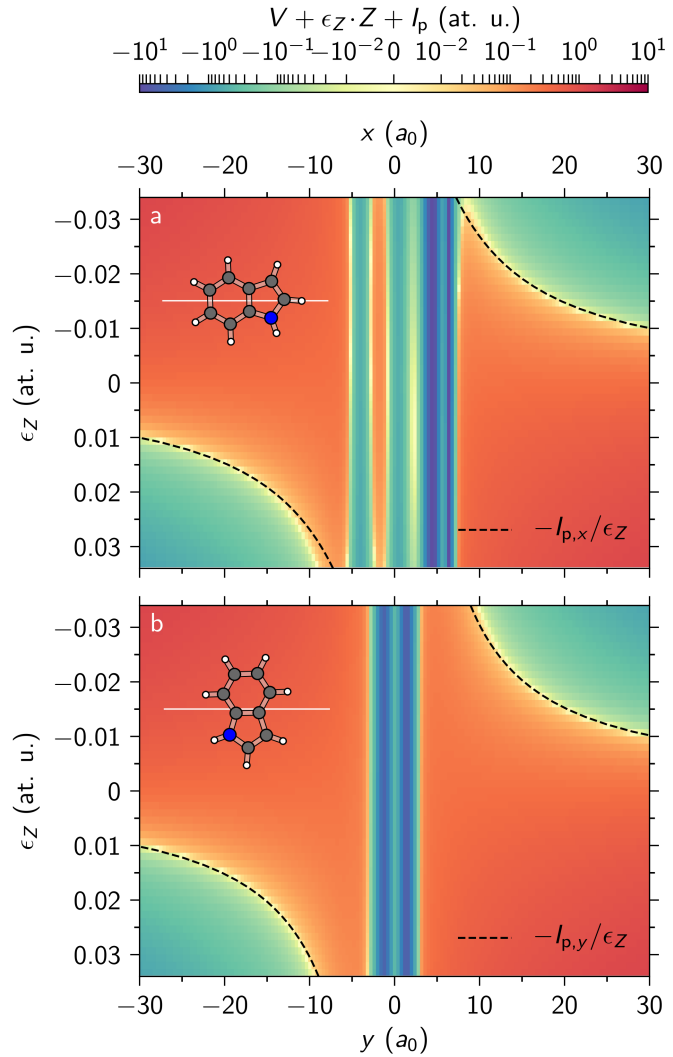


Figure B.1: The sum of quasistatic molecular potential, laser potential, and ionisation energy is shown for a) x -axis and b) y -axis alignment; each panel depicts a single orientation. Only positions on the one principal polarisability axis were evaluated that coincided with the polarisation axis, which is depicted as white line within the corresponding molecule sketch. The deep potential wells near the centre of nuclear charge reflect the proximity to the closest nuclei. For comparison, the respective tunnel exit positions for a quasistatic laser-electric field and neglecting the Coulomb distortion of the barrier¹⁹¹ are shown as dashed black lines.

B.2. Field-direction model

The tunnel-exit positions used for the semiclassical calculations in chapter 6 were obtained with the aid of the field-direction model¹⁸⁵ at the HF/aug-cc-pVTZ level of theory using Psi4¹⁹⁰. The quasistatic electric potential of the neutral indole molecule, $V(\vec{r})$, was computed along the alignment-dependent molecular axis that coincided with the polarisation axis of the ionising laser field. That is, only positions on the x axis were evaluated for the x -axis alignment case and only positions on the y axis for y -axis alignment. In both cases the sampling line was chosen to cross the molecule's centre of nuclear charge. Position and external electric field were sampled in intervals of $\Delta r = 0.5 a_0$ and $\Delta \epsilon = 1.4 \times 10^{-3}$. Subsequently, the sum of quasistatic potential, laser potential, and field-dependent ionisation energy, $V(\vec{r}) + \epsilon_Z \cdot Z + I_p(\vec{r})$, was examined, which assumes a value of 0 at the tunnel exit. Figure B.1 illustrates the corresponding results for the two alignment scenarios. The actual tunnel-exit position used in the semiclassical computations was eventually determined by finding the root of $V(\vec{r}) + \epsilon_Z \cdot Z + I_p(\vec{r})$ at the given instantaneous laser-electric field, which appears as a yellow seam in Figure B.1. For the x -axis alignment case and $\epsilon_Z \approx -3 \times 10^{-2}$ the maximum of the potential barrier was found to be suppressed below 0, i. e., in the barrier-suppression regime. For these cases the barrier maximum was used as tunnel exit position and the energy difference to 0 was assumed to be transformed into additional longitudinal momentum opposing the direction of the instantaneous laser-electric field¹⁸⁵.

B.3. Cationic electric field

The external-field-dependent cationic field of the indole molecule employed in chapter 6, $-\vec{\nabla} V(\vec{r}, \vec{r})$, was calculated at the HF/aug-cc-pVTZ level of theory using Psi4¹⁹⁰. Positions were sampled in intervals of $\Delta r = 0.2 a_0$ and the laser-electric field was sampled in steps of $\Delta \epsilon = 2.8 \times 10^{-3}$ over a $(60 a_0)^3$ cube centred at the cation's centre of nuclear charge.

Bibliography

- [1] E. A. Ponomarenko, E. V. Poverennaya, E. V. Ilgisonis, M. A. Pyatnitskiy, A. T. Kopylov, V. G. Zgoda, A. V. Lisitsa, and A. I. Archakov, "The size of the human proteome: The width and depth," *Int. J. Anal. Chem.* **2016**, 1 (2016).
- [2] A. Radzicka and R. Wolfenden, "A proficient enzyme," *Science* **267**, 90 (1995).
- [3] C. K. Mathews, K. E. van Holde, D. R. Appling, and S. J. Anthony-Cahill, *Biochemistry*, 4th ed. (Pearson Education).
- [4] M.-R. Mihailescu and I. M. Russu, "A signature of the T \rightarrow R transition in human hemoglobin," *PNAS* **98**, 3773 (2001).
- [5] J. Als-Nielsen and D. McMorrow, *Elements of Modern X-ray Physics* (John Wiley & Sons, Chichester, West Sussex, United Kingdom, 2001).
- [6] L. S. Taylor, "The phase retrieval problem," *IEEE Trans. Antennas Propag.* **29**, 386 (1981).
- [7] L. D. Landau and E. M. Lifshitz, *The Classical Theory of Fields*, 3rd ed., Course of Theoretical Physics, Vol. 2 (Pergamon Press, Headington Hill Hall, Oxford, 1971).
- [8] J. D. Watson and F. H. C. Crick, "Molecular structure of nucleic acids: A structure for deoxyribose nucleic acid," *Nature* **171**, 737 (1953).
- [9] V. Ramakrishnan, "Unraveling the structure of the ribosome (Nobel lecture)," *Angew. Chem. Int. Ed.* **49**, 4355 (2010).
- [10] W. Kühlbrandt, D. N. Wang, and Y. Fujiyoshi, "Atomic model of plant light-harvesting complex by electron crystallography," *Nature* **367**, 614 (1994).
- [11] A. H. Zewail, "Laser femtochemistry," *Science* **242**, 1645 (1988).
- [12] H. N. Chapman, C. Caleman, and N. Timneanu, "Diffraction before destruction," *Phil. Trans. R. Soc. B* **369**, 20130313 (2014).
- [13] R. Neutze, R. Wouts, D. van der Spoel, E. Weckert, and J. Hajdu, "Potential for biomolecular imaging with femtosecond x-ray pulses," *Nature* **406**, 752 (2000).
- [14] T. Bredtmann, M. Ivanov, and G. Dixit, "X-ray imaging of chemically active valence electrons during a pericyclic reaction," *Nat. Commun.* **5**, 5589 (2014).
- [15] L. Holmegaard, J. L. Hansen, L. Kalthøj, S. L. Kragh, H. Stapelfeldt, F. Filsinger, J. Küpper, G. Meijer, D. Dimitrovski, M. Abu-samaha, C. P. J. Martiny, and L. B. Madsen, "Photoelectron angular distributions from strong-field ionization of oriented molecules," *Nat. Phys.* **6**, 428 (2010), arXiv:1003.4634 [physics].
- [16] M. Kübel, Z. Dube, A. Y. Naumov, D. M. Villeneuve, P. B. Corkum, and A. Staudte, "Spatiotemporal imaging of valence electron motion," *Nat. Commun.* **10**, 1 (2019).
- [17] T. Bayer, D. Gräfin, S. Kerbstadt, D. Pengel, K. Eickhoff, L. Englert, and M. Wollenhaupt, "Time-resolved 3D imaging of ultrafast spin-orbit wave packet dynamics," *New J. Phys.* **21**, 033001 (2019).
- [18] P. B. Corkum and F. Krausz, "Attosecond Science," *Nat. Phys.* **3**, 381 (2007).
- [19] E. T. Karamatskos, G. Goldsztejn, S. Raabe, P. Stammer, T. Mullins, A. Trabattoni, R. R. Johansen, H. Stapelfeldt, S. Trippel, M. J. J. Vrakking, J. Küpper, and A. Rouzée, "Atomic-resolution imaging of carbonyl sulfide by laser-induced electron diffraction," *J. Chem. Phys.* **150**, 244301 (2019), arXiv:1905.03541 [physics].
- [20] M. G. Pullen, B. Wolter, A.-T. Le, M. Baudisch, M. Hemmer, A. Senftleben, C. D. Schroter, J. Ullrich, R. Moshhammer, C. D. Lin, and J. Biegert, "Imaging an aligned polyatomic molecule with laser-induced electron diffraction," *Nat. Commun.* **6**, 7262 (2015).
- [21] X. Liu, K. Amini, T. Steinle, A. Sanchez, M. Shaikh, B. Belsa, J. Steinmetzer, A.-T. Le, R. Moshhammer, T. Pfeifer, J. Ullrich, R. Moszynski, C. D. Lin, S. Gräfe, and J. Biegert,

- "Imaging an isolated water molecule using a single electron wave packet," *J. Chem. Phys.* **151**, 024306 (2019).
- [22] Y. Ito, C. Wang, A.-T. Le, M. Okunishi, D. Ding, C. D. Lin, and K. Ueda, "Extracting conformational structure information of benzene molecules via laser-induced electron diffraction," *Struct. Dyn.* **3**, 034303 (2016).
- [23] P. M. Paul, E. S. Toma, P. Breger, G. Mullot, F. Augé, P. Balcou, H. G. Muller, and P. Agostini, "Observation of a train of attosecond pulses from high harmonic generation," *Science* **292**, 1689 (2001).
- [24] P. Peng, C. Marceau, and D. Villeneuve, "Attosecond imaging of molecules using high harmonic spectroscopy," *Nat. Rev. Phys.* **1**, 144 (2019).
- [25] C. J. Hensley, J. Yang, and M. Centurion, "Imaging of isolated molecules with ultrafast electron pulses," *Phys. Rev. Lett.* **109**, 133202 (2012).
- [26] J. Yang, V. Makhija, V. Kumarappan, and M. Centurion, "Reconstruction of three-dimensional molecular structure from diffraction of laser-aligned molecules," *Struct. Dyn.* **1**, 044101 (2014).
- [27] J. Küpper, S. Stern, L. Holmegaard, F. Filsinger, A. Rouzée, A. Rudenko, P. Johnsson, A. V. Martin, M. Adolph, A. Aquila, S. Bajt, A. Barty, C. Bostedt, J. Bozek, C. Caleman, R. Coffee, N. Coppola, T. Delmas, S. Epp, B. Erk, L. Foucar, T. Gorkhover, L. Gumprecht, A. Hartmann, R. Hartmann, G. Hauser, P. Holl, A. Hömke, N. Kimmel, F. Krasniqi, K.-U. Kühnel, J. Maurer, M. Messerschmidt, R. Moshhammer, C. Reich, B. Rudek, R. Santra, I. Schlichting, C. Schmidt, S. Schorb, J. Schulz, H. Soltau, J. C. H. Spence, D. Starodub, L. Strüder, J. Thøgersen, M. J. J. Vrakking, G. Weidenspointner, T. A. White, C. Wunderer, G. Meijer, J. Ullrich, H. Stapelfeldt, D. Rolles, and H. N. Chapman, "X-ray diffraction from isolated and strongly aligned gas-phase molecules with a free-electron laser," *Phys. Rev. Lett.* **112**, 083002 (2014), arXiv:1307.4577 [physics].
- [28] T. Kierspel, *Imaging structure and dynamics using controlled molecules*, Dissertation, Universität Hamburg, Hamburg, Germany (2016).
- [29] J. Wiese, J.-F. Olivieri, A. Trabattoni, S. Trippel, and J. Küpper, "Strong-field photoelectron momentum imaging of OCS at finely resolved incident intensities," *New J. Phys.* **21**, 083011 (2019), arXiv:1904.07519 [physics].
- [30] S. K. Pal, J. Peon, and A. H. Zewail, "Biological water at the protein surface: Dynamical solvation probed directly with femtosecond resolution," *PNAS* **99**, 1763 (2002).
- [31] R. W. Boyd, *Nonlinear Optics*, 3rd ed. (Academic Press, Inc., 6277 Sea Harbor Drive Orlando, FL, United States, 2008).
- [32] Y.-P. Chang, F. Filsinger, B. Sartakov, and J. Küpper, "CMIISTARK: Python package for the Stark-effect calculation and symmetry classification of linear, symmetric and asymmetric top wavefunctions in dc electric fields," *Comp. Phys. Comm.* **185**, 339 (2014), current version available from GitHub, arXiv:1308.4076 [physics].
- [33] Y.-P. Chang, D. A. Horke, S. Trippel, and J. Küpper, "Spatially-controlled complex molecules and their applications," *Int. Rev. Phys. Chem.* **34**, 557 (2015), arXiv:1505.05632 [physics].
- [34] R. Escribano, B. Mate, F. Ortigoso, and J. Ortigoso, "Fringe-field effects on the time evolution of pendular states," *Phys. Rev. A* **62**, 023407 (2000).
- [35] T. E. Wall, S. K. Tokunaga, E. A. Hinds, and M. R. Tarbutt, "Nonadiabatic transitions in a Stark decelerator," *Phys. Rev. A* **81**, 033414 (2010).
- [36] U. Even, "The Even-Lavie valve as a source for high intensity supersonic beam," *Eur. Phys. J. Techn. Instrumen.* **2**, 17 (2015).
- [37] J. S. Kienitz, K. Długołęcki, S. Trippel, and J. Küpper, "Improved spatial separation of neutral molecules," *J. Chem. Phys.* **147**, 024304 (2017), arXiv:1704.08912 [physics].
- [38] T. Kierspel, D. A. Horke, Y.-P. Chang, and J. Küpper, "Spatially separated polar samples of the *cis* and *trans* conformers of 3-fluorophenol," *Chem. Phys. Lett.* **591**, 130 (2014), arXiv:1312.4417 [physics].

- [39] D. A. Horke, S. Trippel, Y.-P. Chang, S. Stern, T. Mullins, T. Kierspel, and J. Küpper, "Spatial separation of molecular conformers and clusters," *J. Vis. Exp.* (83), e51137 (2014).
- [40] H. Bieker, J. Onvlee, M. Johny, L. He, T. Kierspel, S. Trippel, D. A. Horke, and J. Küpper, "Pure molecular beam of water dimer," *J. Phys. Chem. A* **123**, 7486 (2019), arXiv:1904.08716 [physics].
- [41] M. Johny, J. Onvlee, T. Kierspel, H. Bieker, S. Trippel, and J. Küpper, "Spatial separation of pyrrole and pyrrole-water clusters," *Chem. Phys. Lett.* **721**, 149–152 (2019), arXiv:1901.05267 [physics].
- [42] H. Stapelfeldt and T. Seideman, "Colloquium: Aligning molecules with strong laser pulses," *Rev. Mod. Phys.* **75**, 543 (2003).
- [43] S. Trippel, T. Mullins, N. L. M. Müller, J. S. Kienitz, J. J. Omiste, H. Stapelfeldt, R. González-Férez, and J. Küpper, "Strongly driven quantum pendulum of the carbonyl sulfide molecule," *Phys. Rev. A* **89**, 051401(R) (2014), arXiv:1401.6897 [quant-ph].
- [44] T. Kierspel, J. Wiese, T. Mullins, J. Robinson, A. Aquila, A. Barty, R. Bean, R. Boll, S. Boutet, P. Bucksbaum, H. N. Chapman, L. Christensen, A. Fry, M. Hunter, J. E. Koglin, M. Liang, V. Mariani, A. Morgan, A. Natan, V. Petrovic, D. Rolles, A. Rudenko, K. Schnorr, H. Stapelfeldt, S. Stern, J. Thøgersen, C. H. Yoon, F. Wang, S. Trippel, and J. Küpper, "Strongly aligned molecules at free-electron lasers," *J. Phys. B* **48**, 204002 (2015), arXiv:1506.03650 [physics].
- [45] S. Trippel, J. Wiese, T. Mullins, and J. Küpper, "Communication: Strong laser alignment of solvent-solute aggregates in the gas-phase," *J. Chem. Phys.* **148**, 101103 (2018), arXiv:1801.08789 [physics].
- [46] J. J. Larsen, K. Hald, N. Bjerre, H. Stapelfeldt, and T. Seideman, "Three dimensional alignment of molecules using elliptically polarized laser fields," *Phys. Rev. Lett.* **85**, 2470 (2000).
- [47] L. Holmegaard, J. H. Nielsen, I. Nevo, H. Stapelfeldt, F. Filsinger, J. Küpper, and G. Meijer, "Laser-induced alignment and orientation of quantum-state-selected large molecules," *Phys. Rev. Lett.* **102**, 023001 (2009), arXiv:0810.2307 [physics].
- [48] B. Friedrich and D. Herschbach, "Alignment and trapping of molecules in intense laser fields," *Phys. Rev. Lett.* **74**, 4623 (1995).
- [49] J. Wiese, J. Onvlee, S. Trippel, and J. Küpper, "Strong-field ionization of complex molecules," (2020), under review, arXiv:2003.02116 [physics].
- [50] F. Filsinger, J. Küpper, G. Meijer, L. Holmegaard, J. H. Nielsen, I. Nevo, J. L. Hansen, and H. Stapelfeldt, "Quantum-state selection, alignment, and orientation of large molecules using static electric and laser fields," *J. Chem. Phys.* **131**, 064309 (2009), arXiv:0903.5413 [physics].
- [51] M. Muramatsu, M. Hita, S. Minemoto, and H. Sakai, "Field-free molecular orientation by an intense nonresonant two-color laser field with a slow turn on and rapid turn off," *Phys. Rev. A* **79**, 011403(R) (2009).
- [52] T. Seideman, "On the dynamics of rotationally broad, spatially aligned wave packets," *J. Chem. Phys.* **115**, 5965 (2001).
- [53] E. T. Karamatskos, S. Raabe, T. Mullins, A. Trabatttoni, P. Stammer, G. Goldsztejn, R. R. Johansen, K. Długołęcki, H. Stapelfeldt, M. J. J. Vrakking, S. Trippel, A. Rouzée, and J. Küpper, "Molecular movie of ultrafast coherent rotational dynamics of OCS," *Nat. Commun.* **10**, 3364 (2019), arXiv:1807.01034 [physics].
- [54] A. Chatterley, E. T. Karamatskos, C. Schouder, L. Christiansen, A. V. Jörgensen, T. Mullins, J. Küpper, and H. Stapelfeldt, "Switched wave packets with spectrally truncated chirped pulses," *J. Chem. Phys.* **148**, 221105 (2018), arXiv:1803.03953 [physics].
- [55] T. Mullins, E. T. Karamatskos, J. Wiese, J. Onvlee, A. Yachmenev, A. Rouzée, S. Trippel, and J. Küpper, "Toward three-dimensional field-free alignment of arbitrary asymmetric top molecules," (2020), in preparation.

- [56] M. Y. Ivanov, M. Spanner, and O. Smirnova, "Anatomy of strong field ionization," *J. Mod. Opt.* **52**, 165 (2005).
- [57] L. Keldysh, "Ionization in the field of a strong electromagnetic wave," *J. Exp. Theor. Phys.* **20**, 1307 (1965).
- [58] T. Schultz and M. Vrakking, eds., *Attosecond and XUV Physics: Ultrafast Dynamics and Spectroscopy*, 1st ed. (Wiley-VCH, Boschstr. 12, 69469 Weinheim, Germany, 2014).
- [59] M. V. Ammosov, N. B. Delone, and V. P. Krainov, "Tunnel ionization of complex atoms and of atomic ions in an alternating electromagnetic field," *Soviet Physics - JETP* **64**, 1191 (1986).
- [60] A. M. Perelomov, V. S. Popov, and M. V. Terentev, "Ionization of atoms in an alternating electric field," *Soviet Physics - JETP* **23**, 924 (1966).
- [61] P. B. Corkum, "Plasma perspective on strong-field multiphoton ionization," *Phys. Rev. Lett.* **71**, 1994 (1993).
- [62] Y. Huismans, A. Rouzee, A. Gijsbertsen, J. H. Jungmann, A. S. Smolkowska, P. S. W. M. Logman, F. Lepine, C. Cauchy, S. Zamith, T. Marchenko, J. M. Bakker, G. Berden, B. Redlich, A. F. G. Van Der Meer, H. G. Muller, W. Vermin, K. J. Schafer, M. Spanner, M. Y. Ivanov, O. Smirnova, D. Bauer, S. V. Popruzhenko, and M. J. J. Vrakking, "Time-resolved holography with photoelectrons," *Science* **331**, 61 (2011).
- [63] N. I. Shvetsov-Shilovski, M. Lein, L. B. Madsen, E. Räsänen, C. Lemell, J. Burgdörfer, D. G. Arbó, and K. Tókési, "Semiclassical two-step model for strong-field ionization," *Phys. Rev. A* **94**, 013415 (2016).
- [64] A. C. Kak and M. Slaney, *Principles of Computerized Tomographic Imaging* (IEEE, New York, NY, USA, 1988).
- [65] J. S. Kienitz, S. Trippel, T. Mullins, K. Długołęcki, R. González-Férez, and J. Küpper, "Adiabatic mixed-field orientation of ground-state-selected carbonyl sulfide molecules," *Chem. Phys. Chem.* **17**, 3740 (2016), arXiv:1607.05615 [physics].
- [66] K. Amini, R. Boll, A. Lauer, M. Burt, J. W. L. Lee, L. Christensen, F. Brauße, T. Mullins, E. Savelyev, U. Ablíkım, N. Berrah, C. Bomme, S. Düsterer, B. Erk, H. Höppner, P. Johnsson, T. Kierspel, F. Krečinić, J. Küpper, M. Müller, E. Müller, H. Redlin, A. Rouzée, N. Schirmel, J. Thøgersen, S. Techert, S. Toleikis, R. Treusch, S. Trippel, A. Ulmer, J. Wiese, C. Vallance, A. Rudenko, H. Stapelfeldt, M. Brouard, and D. Rolles, "Alignment, orientation, and Coulomb explosion of difluoroiodobenzene studied with the pixel imaging mass spectrometry (PIImMS) camera," *J. Chem. Phys.* **147**, 013933 (2017), arXiv:1706.08376 [physics].
- [67] M. Di Fraia, P. Finetti, R. Richter, K. C. Prince, J. Wiese, M. Devetta, M. Negro, C. Vozzi, A. G. Ciriolo, A. Pusala, A. Demidovich, M. B. Danailov, E. T. Karamatskos, S. Trippel, J. Küpper, and C. Callegari, "Impulsive laser-induced alignment of OCS molecules at FERMI," *Phys. Chem. Chem. Phys.* **19**, 19733 (2017), arXiv:1808.07281 [physics].
- [68] P. Herwig, K. Zawatzky, M. Grieser, O. Heber, B. Jordon-Thaden, C. Krantz, O. Novotný, R. Repnow, V. Schurig, D. Schwalm, Z. Vager, A. Wolf, O. Trapp, and H. Kreckel, "Imaging the absolute configuration of a chiral epoxide in the gas phase," *Science* **342**, 1084 (2013).
- [69] V. Kumarappan, C. Z. Bisgaard, S. S. Viftrup, L. Holmegaard, and H. Stapelfeldt, "Role of rotational temperature in adiabatic molecular alignment," *J. Chem. Phys.* **125**, 194309 (2006).
- [70] V. Makhija, X. Ren, and V. Kumarappan, "Metric for three-dimensional alignment of molecules," *Phys. Rev. A* **85**, 033425 (2012).
- [71] T. Zuo, A. D. Bandrauk, and P. B. Corkum, "Laser-induced electron diffraction: a new tool for probing ultrafast molecular dynamics," *Chem. Phys. Lett.* **259**, 313 (1996).
- [72] C. I. Blaga, J. Xu, A. D. DiChiara, E. Sistrunk, K. Zhang, P. Agostini, T. A. Miller, L. F. DiMauro, and C. D. Lin, "Imaging ultrafast molecular dynamics with laser-induced electron diffraction," *Nature* **483**, 194 (2012).

- [73] G. G. Paulus, W. Becker, W. Nicklich, and H. Walther, "Rescattering effects in above threshold ionization: a classical model," *J. Phys. B* **27**, L703 (1994).
- [74] E. Karamatskos, *Molecular-Frame Angularly-Resolved Photoelectron Spectroscopy*, Dissertation, Universität Hamburg, Hamburg, Germany (2019).
- [75] A. Trabattoni, J. Wiese, U. De Giovannini, J.-F. Olivieri, T. Mullins, J. Onvlee, S.-K. Son, B. Frusteri, A. Rubio, S. Trippel, and J. Küpper, "Setting the photoelectron clock through molecular alignment," *Nat. Commun.* **11**, 2546 (2020), arXiv:1802.06622 [physics].
- [76] S. Hankin, D. Villeneuve, P. Corkum, and D. Rayner, "Intense-field laser ionization rates in atoms and molecules," *Phys. Rev. A* **64**, 013405 (2001).
- [77] N. A. Hart, J. Strohaber, G. Kaya, N. Kaya, A. A. Kolomenskii, and H. A. Schuessler, "Intensity-resolved above-threshold ionization of xenon with short laser pulses," *Phys. Rev. A* **89**, 1393 (2014).
- [78] Y. Shao, M. Li, M. M. Liu, X. Sun, X. Xie, P. Wang, Y. Deng, C. Wu, Q. Gong, and Y. Liu, "Isolating resonant excitation from above-threshold ionization," *Phys. Rev. A* **92**, 2008 (2015).
- [79] J. Yu, W. Hu, X. Li, P. Ma, L. He, F. Liu, C. Wang, S. Luo, and D. Ding, "Contribution of resonance excitation on ionization of OCS molecules in strong laser fields," *J. Phys. B* **50**, 235602 (2017).
- [80] M. Li, P. Zhang, S. Luo, Y. Zhou, Q. Zhang, P. Lan, and P. Lu, "Selective enhancement of resonant multiphoton ionization with strong laser fields," *Phys. Rev. A* **92**, 1945 (2015).
- [81] V. Schyja, T. Lang, and H. Helm, "Channel switching in above-threshold ionization of xenon," *Phys. Rev. A* **57**, 3692 (1998).
- [82] T. Marchenko, H. G. Muller, K. J. Schafer, and M. J. J. Vrakking, "Electron angular distributions in near-threshold atomic ionization," *J. Phys. B* **43**, 095601 (2010).
- [83] D. Dimitrovski, J. Maurer, H. Stapelfeldt, and L. B. Madsen, "Strong-field ionization of three-dimensionally aligned naphthalene molecules: orbital modification and imprints of orbital nodal planes," *J. Phys. B* **48**, 245601 (2015).
- [84] J. Maurer, D. Dimitrovski, L. Christensen, L. B. Madsen, and H. Stapelfeldt, "Molecular-frame 3D photoelectron momentum distributions by tomographic reconstruction," *Phys. Rev. Lett.* **109**, 123001 (2012).
- [85] M. A. Walker, P. Hansch, and L. D. Van Woerkom, "Intensity-resolved multiphoton ionization: Circumventing spatial averaging," *Phys. Rev. A* **57**, R701 (1998).
- [86] P. Wang, A. M. Sayler, K. D. Carnes, B. D. Esry, and I. Ben-Itzhak, "Disentangling the volume effect through intensity-difference spectra: application to laser-induced dissociation of H_2^+ ," *Opt. Lett.* **30**, 664 (2005).
- [87] J. Strohaber, A. A. Kolomenskii, and H. A. Schuessler, "Reconstruction of ionization probabilities from spatially averaged data in N dimensions," *Phys. Rev. A* **82**, 013403 (2010).
- [88] S. Trippel, T. Mullins, N. L. M. Müller, J. S. Kienitz, K. Długołęcki, and J. Küpper, "Strongly aligned and oriented molecular samples at a kHz repetition rate," *Mol. Phys.* **111**, 1738 (2013), arXiv:1301.1826 [physics].
- [89] U. Even, J. Jortner, D. Noy, N. Lavie, and N. Cossart-Magos, "Cooling of large molecules below 1 K and He clusters formation," *J. Chem. Phys.* **112**, 8068 (2000).
- [90] C. Bordas, F. Paulig, H. Helm, and D. L. Huestis, "Photoelectron imaging spectrometry: Principle and inversion method," *Rev. Sci. Instrum.* **67**, 2257 (1996).
- [91] C. E. Rallis, T. G. Burwitz, P. R. Andrews, M. Zohrabi, R. Averin, S. De, B. Bergues, B. Jochim, A. V. Voznyuk, N. Gregerson, B. Gaire, I. Znakovskaya, J. McKenna, K. D. Carnes, M. F. Kling, I. Ben-Itzhak, and E. Wells, "Incorporating real time velocity map image reconstruction into closed-loop coherent control," *Rev. Sci. Instrum.* **85**, 113105 (2014).
- [92] D. D. Hickstein, R. Yurchak, D. Dhruvajyoti, C.-Y. Shih, and S. T. Gibson, "PyAbel (v0.7): A Python package for Abel transforms," (2016).

- [93] R. R. Freeman, P. H. Bucksbaum, H. Milchberg, S. Darack, D. Schumacher, and M. E. Geusic, "Above-threshold ionization with subpicosecond laser pulses," *Phys. Rev. Lett.* **59**, 1092 (1987).
- [94] P. A. Korneev, S. V. Popruzhenko, S. P. Goreslavski, T.-M. Yan, D. Bauer, W. Becker, M. Kübel, M. F. Kling, C. Rödel, M. Wünsche, and G. G. Paulus, "Interference carpets in above-threshold ionization: From the Coulomb-free to the Coulomb-dominated regime," *Phys. Rev. Lett.* **108**, 223601 (2012).
- [95] R. R. Freeman and P. H. Bucksbaum, "Investigations of above-threshold ionization using subpicosecond laser pulses," *J. Phys. B* **24**, 325 (1991).
- [96] P. J. Linstrom and W. G. Mallard, eds., *NIST Chemistry WebBook, NIST Standard Reference Database Number 69* (National Institute of Standards and Technology, Gaithersburg MD, 20899, 2017).
- [97] T. R. O'Brian, J.-B. Kim, G. Lan, T. J. McIlrath, and T. B. Lucatorto, "Verification of the ponderomotive approximation for the ac Stark shift in Xe Rydberg levels," *Phys. Rev. A* **49**, R649 (1994).
- [98] Y. Tanaka, A. S. Jursa, and F. J. LeBlanc, "Higher ionization potentials of linear triatomic molecules. II. CS₂, COS, and N₂O," *J. Chem. Phys.* **32**, 1205 (1960).
- [99] K. Sunanda, B. N. Rajasekhar, P. Saraswathy, and B. N. Jagatap, "Photo-absorption studies on carbonyl sulphide in 30,000–91,000 cm⁻¹ region using synchrotron radiation," *J. Quant. Spectrosc. Radiat. Transf.* **113**, 58 (2012).
- [100] C. Cossart-Magos, M. Jungen, R. Xu, and F. Launay, "High resolution absorption spectrum of jet-cooled OCS between 64 000 and 91 000 cm⁻¹," *J. Chem. Phys.* **119**, 3219 (2003).
- [101] A. Rudenko, K. Zrost, C. D. Schröter, V. L. B. De Jesus, B. Feuerstein, R. Moshhammer, and J. Ullrich, "Resonant structures in the low-energy electron continuum for single ionization of atoms in the tunnelling regime," *J. Phys. B* **37**, L407 (2004).
- [102] D. G. Arbó, S. Yoshida, E. Persson, K. I. Dimitriou, and J. Burgdörfer, "Interference oscillations in the angular distribution of laser-ionized electrons near ionization threshold," *Phys. Rev. Lett.* **96**, 143003 (2006).
- [103] Z. Chen, T. Morishita, A.-T. Le, M. Wickenhauser, X. M. Tong, and C. D. Lin, "Analysis of two-dimensional photoelectron momentum spectra and the effect of the long-range Coulomb potential in single ionization of atoms by intense lasers," *Phys. Rev. A* **74**, 053405 (2006).
- [104] D. G. Arbó, K. I. Dimitriou, E. Persson, and J. Burgdörfer, "Sub-Poissonian angular momentum distribution near threshold in atomic ionization by short laser pulses," *Phys. Rev. A* **78**, 1418 (2008).
- [105] P. B. Corkum, M. Y. Ivanov, and J. S. Wright, "Subfemtosecond processes in strong laser fields," *Annu. Rev. Phys. Chem.* **48**, 387 (1997).
- [106] F. Calegari, D. Ayuso, A. Trabattoni, L. Belshaw, S. De Camillis, S. Anumula, F. Frassetto, L. Poletto, A. Palacios, P. Decleva, J. B. Greenwood, F. Martín, and M. Nisoli, "Ultrafast electron dynamics in phenylalanine initiated by attosecond pulses," *Science* **346**, 336 (2014).
- [107] F. Lépine, M. Y. Ivanov, and M. J. J. Vrakking, "Attosecond molecular dynamics: fact or fiction?" *Nat. Photon.* **8**, 195 (2014).
- [108] P. M. Kraus, B. Mignolet, D. Baykusheva, A. Rupenyan, L. Horný, E. F. Penka, G. Grassi, O. I. Tolstikhin, J. Schneider, F. Jensen, L. B. Madsen, A. D. Bandrauk, F. Remacle, and H. J. Wörner, "Measurement and laser control of attosecond charge migration in ionized iodoacetylene," *Science* **350**, 790 (2015).
- [109] B. Wolter, M. G. Pullen, A. T. Le, M. Baudisch, K. Doblhoff-Dier, A. Senftleben, M. Hemmer, C. D. Schroter, J. Ullrich, T. Pfeifer, R. Moshhammer, S. Gräfe, O. Vendrell, C. D. Lin, and J. Biegert, "Ultrafast electron diffraction imaging of bond breaking in di-ionized acetylene," *Science* **354**, 308 (2016).

- [110] S. G. Walt, B. N. Ram, M. Atala, N. I. Shvetsov-Shilovski, A. von Conta, D. Baykusheva, M. Lein, and H. J. Wörner, "Dynamics of valence-shell electrons and nuclei probed by strong-field holography and rescattering," *Nat. Commun.* **8**, 15651 (2017).
- [111] H. Fuest, Y. H. Lai, C. I. Blaga, K. Suzuki, J. Xu, P. Rupp, H. Li, P. Wnuk, P. Agostini, K. Yamazaki, M. Kanno, H. Kono, M. F. Kling, and L. F. DiMauro, "Diffractive imaging of C₆₀ structural deformations induced by intense femtosecond midinfrared laser fields," *Phys. Rev. Lett.* **122**, 053002 (2019).
- [112] K. Amini, M. Sclafani, T. Steinle, A.-T. Le, A. Sanchez, C. Müller, J. Steinmetzer, L. Yue, J. R. M. Saavedra, M. Hemmer, M. Lewenstein, R. Moshhammer, T. Pfeifer, M. G. Pullen, J. Ullrich, B. Wolter, R. Moszynski, F. J. G. de Abajo, C. D. Lin, S. Gräfe, and J. Biegert, "Imaging the Renner–Teller effect using laser-induced electron diffraction," *PNAS* **116**, 8173 (2019).
- [113] P. Eckle, A. N. Pfeiffer, C. Cirelli, A. Staudte, R. Dörner, H. G. Muller, M. Büttiker, and U. Keller, "Attosecond ionization and tunneling delay time measurements in helium," *Science* **322**, 1525 (2008).
- [114] M. Meckel, A. Staudte, S. Patchkovskii, D. M. Villeneuve, P. B. Corkum, R. Dörner, and M. Spanner, "Signatures of the continuum electron phase in molecular strong-field photoelectron holography," *Nat. Phys.* **10**, 594 (2014).
- [115] Z. Chen, A.-T. Le, T. Morishita, and C. D. Lin, "Quantitative rescattering theory for laser-induced high-energy plateau photoelectron spectra," *Phys. Rev. A* **79**, 033409 (2009).
- [116] J. Xu, C. I. Blaga, K. Zhang, Y. H. Lai, C. D. Lin, T. A. Miller, P. Agostini, and L. F. DiMauro, "Diffraction using laser-driven broadband electron wave packets," *Nat. Commun.* **5**, 4635 (2014).
- [117] F. Schell, T. Bredtmann, C.-P. Schulz, S. Patchkovskii, M. J. J. Vrakking, and J. Mikosch, "Molecular orbital imprint in laser-driven electron recollision," *Sci. Adv.* **4**, eaap8148 (2018).
- [118] M. Lein, "Antibonding molecular orbitals under the influence of elliptically polarized intense light," *J. Phys. B* **36**, L155 (2003).
- [119] H. Niikura, F. Légaré, R. Hasbani, A. D. Bandrauk, M. Y. Ivanov, D. M. Villeneuve, and P. B. Corkum, "Sub-laser-cycle electron pulses for probing molecular dynamics," *Nature* **417**, 917 (2002).
- [120] M. Busuladžić, A. Gazibegović-Busuladžić, D. B. Milošević, and W. Becker, "Angle-resolved high-order above-threshold ionization of a molecule: Sensitive tool for molecular characterization," *Phys. Rev. Lett.* **100**, 203003 (2008).
- [121] M. G. Pullen, B. Wolter, A. T. Le, M. Baudisch, M. Sclafani, H. Pires, C. D. Schröter, J. Ullrich, R. Moshhammer, T. Pfeifer, C. D. Lin, and J. Biegert, "Influence of orbital symmetry on diffraction imaging with rescattering electron wave packets," *Nat. Commun.* **7**, 11922 (2016).
- [122] N. Suárez, A. Chacón, M. F. Ciappina, B. Wolter, J. Biegert, and M. Lewenstein, "Above-threshold ionization and laser-induced electron diffraction in diatomic molecules," *Phys. Rev. A* **94**, 043423 (2016).
- [123] M.-M. Liu, M. Li, C. Wu, Q. Gong, A. Staudte, and Y. Liu, "Phase structure of strong-field tunneling wave packets from molecules," *Phys. Rev. Lett.* **116**, 163004 (2016).
- [124] A. T. J. B. Eppink and D. H. Parker, "Velocity map imaging of ions and electrons using electrostatic lenses: Application in photoelectron and photofragment ion imaging of molecular oxygen," *Rev. Sci. Instrum.* **68**, 3477 (1997).
- [125] W. Becker and D. B. Milošević, "Above-threshold ionization for very low electron energy," *J. Phys. B* **48**, 151001 (2015).
- [126] W. Becker, F. Grasbon, R. Kopold, D. B. Milošević, G. G. Paulus, and H. Walther, "Above-threshold ionization: From classical features to quantum effects," *Adv. Atom. Mol. Opt. Phys.* **48**, 35 (2002).

- [127] C. T. L. Smeenk, L. Arissian, A. V. Sokolov, M. Spanner, K. F. Lee, A. Staudte, D. M. Villeneuve, and P. B. Corkum, "Alignment dependent enhancement of the photoelectron cutoff for multiphoton ionization of molecules," *Phys. Rev. Lett.* **112**, 253001 (2014), arXiv:1304.6942 [physics].
- [128] M. A. L. Marques, N. T. Maitra, F. Nogueira, E. K. U. Gross, and A. Rubio, *Fundamentals of Time-Dependent Density Functional Theory*, Lecture Notes in Physics (Springer Verlag, 2011).
- [129] L. Tao and A. Scrinzi, "Photo-electron momentum spectra from minimal volumes: the time-dependent surface flux method," *New J. Phys.* **14**, 013021 (2012).
- [130] P. Wopperer, U. De Giovannini, and A. Rubio, "Efficient and accurate modeling of electron photoemission in nanostructures with TDDFT," *Eur. Phys. J. D* **90**, 1307 (2017).
- [131] T. F. Gallagher, "Above-threshold ionization in low-frequency limit," *Phys. Rev. Lett.* **61**, 2304 (1988).
- [132] P. B. Corkum, N. H. Burnett, and F. Brunel, "Above-threshold ionization in the long-wavelength limit," *Phys. Rev. Lett.* **62**, 1259 (1989).
- [133] J. Daněk, M. Klaiber, K. Z. Hatsagortsyan, C. H. Keitel, B. Willenberg, J. Maurer, B. W. Mayer, C. R. Phillips, L. Gallmann, and U. Keller, "Interplay between Coulomb-focusing and non-dipole effects in strong-field ionization with elliptical polarization," *J. Phys. B* **51**, 114001 (2018).
- [134] A. N. Pfeiffer, C. Cirelli, A. S. Landsman, M. Smolarski, D. Dimitrovski, L. B. Madsen, and U. Keller, "Probing the longitudinal momentum spread of the electron wave packet at the tunnel exit," *Phys. Rev. Lett.* **109**, 083002 (2012).
- [135] J.-W. Geng, W.-H. Xiong, X.-R. Xiao, L.-Y. Peng, and Q. Gong, "Nonadiabatic electron dynamics in orthogonal two-color laser fields with comparable intensities," *Phys. Rev. Lett.* **115**, 193001 (2015).
- [136] J. Tian, X. Wang, and J. Eberly, "Numerical detector theory for the longitudinal momentum distribution of the electron in strong field ionization," *Phys. Rev. Lett.* **118**, 213201 (2017).
- [137] I. Tatischeff, R. Klein, T. Zemb, and M. Duquesne, "Solvent interactions with the indole chromophore," *Chem. Phys. Lett.* **54**, 394 (1978).
- [138] P. Song and F.-C. Ma, "Intermolecular hydrogen-bonding effects on photophysics and photochemistry," *Int. Rev. Phys. Chem.* **32**, 589 (2013).
- [139] D. A. Horke, H. M. Watts, A. D. Smith, E. Jager, E. Springate, O. Alexander, C. Cacho, R. T. Chapman, and R. S. Minns, "Hydrogen bonds in excited state proton transfer," *Phys. Rev. Lett.* **117**, 163002 (2016).
- [140] G. Berden, W. L. Meerts, and E. Jalviste, "Rotationally resolved ultraviolet spectroscopy of indole, indazole, and benzimidazole: Inertial axis reorientation in the $S_1(^1L_b) \leftarrow S_0$ transitions," *J. Chem. Phys.* **103**, 9596 (1995).
- [141] J. Küpper, D. W. Pratt, L. Meerts, C. Brand, J. Tatchen, and M. Schmitt, "Vibronic coupling in indole: II. experimental investigation of the $^1L_a-^1L_b$ interaction using rotationally resolved electronic spectroscopy," *Phys. Chem. Chem. Phys.* **12**, 4980 (2010).
- [142] R. Livingstone, O. Schalk, A. E. Boguslavskiy, G. Wu, L. Therese Bergendahl, A. Stolow, M. J. Paterson, and D. Townsend, "Following the excited state relaxation dynamics of indole and 5-hydroxyindole using time-resolved photoelectron spectroscopy," *J. Chem. Phys.* **135**, 194307 (2011).
- [143] A. L. Sobolewski and W. Domcke, "Photoinduced charge separation in indole-water clusters," *Chem. Phys. Lett.* **329**, 130 (2000).
- [144] H. Lami and N. Glasser, "Indole solvatochromism revisited," *J. Chem. Phys.* **84**, 597 (1986).
- [145] J. T. Vivian and P. R. Callis, "Mechanisms of tryptophan fluorescence shifts in proteins," *Biophys J* **80**, 2093 (2001).

- [146] T. M. Korter, D. W. Pratt, and J. Küpper, "Indole-H₂O in the gas phase. Structures, barriers to internal motion, and S₁ ← S₀ transition moment orientation. Solvent reorganization in the electronically excited state," *J. Phys. Chem. A* **102**, 7211 (1998).
- [147] S. Blanco, J. Lopez, J. Alonso, P. Ottaviani, and W. Caminati, "Pure rotational spectrum and model calculations of indole-water," *J. Chem. Phys.* **119**, 880 (2003).
- [148] C. Kang, T. M. Korter, and D. W. Pratt, "Experimental measurement of the induced dipole moment of an isolated molecule in its ground and electronically excited states: Indole and indole-H₂O," *J. Chem. Phys.* **122**, 174301 (2005).
- [149] M. Mons, I. Dimicoli, B. Tardivel, F. Piuzzi, V. Brenner, and P. Millié, "Site dependence of the binding energy of water to indole: Microscopic approach to the side chain hydration of tryptophan," *J. Phys. Chem. A* **103**, 9958 (1999).
- [150] J. Hansen, H. Stapelfeldt, D. Dimitrovski, M. Abu-Samha, C. Martiny, and L. Madsen, "Time-resolved photoelectron angular distributions from strong-field ionization of rotating naphthalene molecules," *Phys. Rev. Lett.* **106**, 073001 (2011).
- [151] F. Krasniqi, B. Najjari, L. Strüder, D. Rolles, A. Voitkiv, and J. Ullrich, "Imaging molecules from within: Ultrafast angstrom-scale structure determination of molecules via photoelectron holography using free-electron lasers," *Phys. Rev. A* **81**, 033411 (2010).
- [152] A. Landers, T. Weber, I. Ali, A. Cassimi, M. Hattass, O. Jagutzki, A. Nauert, T. Osipov, A. Staudte, M. H. Prior, H. Schmidt-Böcking, C. L. Cocke, and R. Dörner, "Photoelectron diffraction mapping: Molecules illuminated from within," *Phys. Rev. Lett.* **87**, 013002 (2001).
- [153] R. Velotta, N. Hay, M. Mason, M. Castillejo, and J. Marangos, "High-order harmonic generation in aligned molecules," *Phys. Rev. Lett.* **87**, 183901 (2001).
- [154] F. Filsinger, G. Meijer, H. Stapelfeldt, H. Chapman, and J. Küpper, "State- and conformer-selected beams of aligned and oriented molecules for ultrafast diffraction studies," *Phys. Chem. Chem. Phys.* **13**, 2076 (2011), arXiv:1009.0871 [physics].
- [155] J. Yang, M. Guehr, X. Shen, R. Li, T. Vecchione, R. Coffee, J. Corbett, A. Fry, N. Hartmann, C. Hast, K. Hegazy, K. Jobe, I. Makasyuk, J. Robinson, M. S. Robinson, S. Vetter, S. Weathersby, C. Yoneda, X. Wang, and M. Centurion, "Diffractive imaging of coherent nuclear motion in isolated molecules," *Phys. Rev. Lett.* **117**, 153002 (2016).
- [156] E. A. Shapiro, I. Khavkine, M. Spanner, and M. Y. Ivanov, "Strong-field molecular alignment for quantum logic and quantum control," *Phys. Rev. A* **67**, 013406 (2003).
- [157] A. Barty, J. Küpper, and H. N. Chapman, "Molecular imaging using x-ray free-electron lasers," *Annu. Rev. Phys. Chem.* **64**, 415 (2013).
- [158] E. Wolf, "Three-dimensional structure determination of semi-transparent objects from holographic data," *Opt. Comm.* **1**, 153 (1969).
- [159] S. T. Park, A. Gahlmann, Y. He, J. S. Feenstra, and A. H. Zewail, "Ultrafast electron diffraction reveals dark structures of the biological chromophore indole," *Angew. Chem. Int. Ed.* **47**, 9496 (2008).
- [160] J. J. Larsen, H. Sakai, C. P. Safvan, I. Wendt-Larsen, and H. Stapelfeldt, "Aligning molecules with intense nonresonant laser fields," *J. Chem. Phys.* **111**, 7774 (1999).
- [161] F. Rosca-Pruna and M. J. J. Vrakking, "Experimental observation of revival structures in picosecond laser-induced alignment of I₂," *Phys. Rev. Lett.* **87**, 153902 (2001).
- [162] J. C. H. Spence and R. B. Doak, "Single molecule diffraction," *Phys. Rev. Lett.* **92**, 198102 (2004).
- [163] L. L. Connell, S. M. Ohline, P. W. Joireman, T. C. Corcoran, and P. M. Felker, "Rotational coherence spectroscopy of 1-naphthol-(water)₂ clusters: Structural evidence for a cyclic hydrogen-bonded trimer," *J. Chem. Phys.* **94**, 4668 (1991).
- [164] C. Riehn, "High-resolution pump-probe rotational coherence spectroscopy - rotational constants and structure of ground and electronically excited states of large molecular systems," *Chem. Phys.* **283**, 297 (2002).

- [165] G. Galinis, C. Cacho, R. T. Chapman, A. M. Ellis, M. Lewerenz, L. G. M. Luna, R. S. Minns, M. Mladenović, A. Rouzée, E. Springate, I. C. E. Turcu, M. J. Watkins, and K. von Haeften, "Probing the structure and dynamics of molecular clusters using rotational wave packets," *Phys. Rev. Lett.* **113**, 043004 (2014), arXiv:1402.5401 [physics].
- [166] S. Trippel, Y.-P. Chang, S. Stern, T. Mullins, L. Holmegaard, and J. Küpper, "Spatial separation of state- and size-selected neutral clusters," *Phys. Rev. A* **86**, 033202 (2012), arXiv:1208.4935 [physics].
- [167] D. A. Horke, Y.-P. Chang, K. Długołęcki, and J. Küpper, "Separating para and ortho water," *Angew. Chem. Int. Ed.* **53**, 11965 (2014), arXiv:1407.2056 [physics].
- [168] I. Nevo, L. Holmegaard, J. H. Nielsen, J. L. Hansen, H. Stapelfeldt, F. Filsinger, G. Meijer, and J. Küpper, "Laser-induced 3D alignment and orientation of quantum state-selected molecules," *Phys. Chem. Chem. Phys.* **11**, 9912 (2009), arXiv:0906.2971 [physics].
- [169] T. Kjeldsen, C. Bisgaard, L. Madsen, and H. Stapelfeldt, "Influence of molecular symmetry on strong-field ionization: Studies on ethylene, benzene, fluorobenzene, and chlorofluorobenzene," *Phys. Rev. A* **71**, 013418 (2005).
- [170] H. Lippert, V. Stert, L. Hesse, C. P. Schulz, I. V. Hertel, and W. Radloff, "Ultrafast photoinduced processes in indole-water clusters," *Chem. Phys. Lett.* **376**, 40 (2003).
- [171] A. Peralta Conde, V. Ovejas, R. Montero, F. Castaño, and A. Longarte, "Influence of solvation on the indole photophysics: Ultrafast dynamics of indole-water clusters," *Chem. Phys. Lett.* **530**, 25 (2012).
- [172] J. Itatani, J. Levesque, D. Zeidler, H. Niikura, H. Pépin, J. C. Kieffer, P. B. Corkum, and D. M. Villeneuve, "Tomographic imaging of molecular orbitals," *Nature* **432**, 867 (2004).
- [173] T. Kanai, S. Minemoto, and H. Sakai, "Quantum interference during high-order harmonic generation from aligned molecules," *Nature* **435**, 470 (2005).
- [174] M. Spanner, O. Smirnova, P. B. Corkum, and M. Y. Ivanov, "Reading diffraction images in strong field ionization of diatomic molecules," *J. Phys. B* **37**, L243 (2004).
- [175] C. Lux, M. Wollenhaupt, T. Bolze, Q. Liang, J. Koehler, C. Sarpe, and T. Baumert, "Circular dichroism in the photoelectron angular distributions of camphor and fenchone from multiphoton ionization with femtosecond laser pulses," *Angew. Chem. Int. Ed.* **51**, 5001 (2012).
- [176] I. Dreisigacker and M. Lein, "Photoelectron circular dichroism of chiral molecules studied with a continuum-state-corrected strong-field approximation," *Phys. Rev. A* **89**, 053406 (2014).
- [177] M. H. M. Janssen and I. Powis, "Detecting chirality in molecules by imaging photoelectron circular dichroism," *Phys. Chem. Chem. Phys.* **16**, 856 (2014).
- [178] M. Paul, L. Yue, and S. Gräfe, "Imprints of the molecular electronic structure in the photoelectron spectra of strong-field ionized asymmetric triatomic model molecules," *Phys. Rev. Lett.* **120**, 233202 (2018).
- [179] D. Bauer and P. Koval, "QPROP: A Schrödinger-solver for intense laser-atom interaction," *Comp. Phys. Comm.* **174**, 396 (2006).
- [180] X.-B. Bian, Y. Huismans, O. Smirnova, K.-J. Yuan, M. J. J. Vrakking, and A. D. Bandrauk, "Subcycle interference dynamics of time-resolved photoelectron holography with midinfrared laser pulses," *Phys. Rev. A* **84**, 043420 (2011).
- [181] M. Li, J.-W. Geng, M. Han, M. M. Liu, L.-Y. Peng, Q. Gong, and Y. Liu, "Subcycle nonadiabatic strong-field tunneling ionization," *Phys. Rev. A* **93**, 013402 (2016).
- [182] T.-M. Yan and D. Bauer, "Sub-barrier Coulomb effects on the interference pattern in tunneling-ionization photoelectron spectra," *Phys. Rev. A* **86**, 053403 (2012).
- [183] N. I. Shvetsov-Shilovski and M. Lein, "Effects of the Coulomb potential in interference patterns of strong-field holography with photoelectrons," *Phys. Rev. A* **97**, 013411 (2018).
- [184] X. M. Tong and C. D. Lin, "Empirical formula for static field ionization rates of atoms and molecules by lasers in the barrier-suppression regime," *J. Phys. B* **38**, 2593 (2005).

- [185] A. N. Pfeiffer, C. Cirelli, M. Smolarski, D. Dimitrovski, M. Abu-samha, L. B. Madsen, and U. Keller, "Attoclock reveals natural coordinates of the laser-induced tunnelling current flow in atoms," *Nat. Phys.* **8**, 76 (2011).
- [186] L. D. Landau and E. M. Lifshitz, *Mechanics*, 3rd ed., Course of Theoretical Physics, Vol. 1 (Butterworth Heinemann, 1976).
- [187] M. W. Schmidt, K. K. Baldridge, J. A. Boatz, S. T. Elbert, M. S. Gordon, J. H. Jensen, S. Koseki, N. Matsunaga, K. A. Nguyen, S. Su, T. L. Windus, M. Dupuis, and J. A. Montgomery, "General atomic and molecular electronic structure system," *J. Comput. Chem.* **14**, 1347 (1993).
- [188] M. S. Gordon and M. W. Schmidt, in *Theory and Applications of Computational Chemistry: the first forty years*, edited by C. E. Dykstra, G. Frenking, K. S. Kim, and G. E. Scuseria (Elsevier, Amsterdam, 2005).
- [189] W. H. Press, S. A. Teukolsky, W. T. Vetterling, and B. P. Flannery, *Numerical Recipes in FORTRAN: The Art of Scientific Computing*, 2nd ed. (Cambridge University Press, 1992).
- [190] R. M. Parrish, L. A. Burns, D. G. A. Smith, A. C. Simmonett, A. E. DePrince, E. G. Hohenstein, U. Bozkaya, A. Y. Sokolov, R. Di Remigio, R. M. Richard, J. F. Gonthier, A. M. James, H. R. McAlexander, A. Kumar, M. Saitow, X. Wang, B. P. Pritchard, P. Verma, H. F. Schaefer, K. Patkowski, R. A. King, E. F. Valeev, F. A. Evangelista, J. M. Turney, T. D. Crawford, and C. D. Sherrill, "Psi4 1.1: An open-source electronic structure program emphasizing automation, advanced libraries, and interoperability," *J. Chem. Theory Comput.* **13**, 3185 (2017).
- [191] S. V. Popruzhenko, "Keldysh theory of strong field ionization: history, applications, difficulties and perspectives," *J. Phys. B* **47**, 204001 (2014).
- [192] W. H. Press and S. A. Teukolsky, "Adaptive stepsize Runge-Kutta integration," *Comput. Phys.* **6**, 188 (1992).
- [193] M. Meckel, D. Comtois, D. Zeidler, A. Staudte, D. Pavičić, H. C. Bandulet, H. Pépin, J. C. Kieffer, R. Dörner, D. M. Villeneuve, and P. B. Corkum, "Laser-induced electron tunneling and diffraction," *Science* **320**, 1478 (2008).
- [194] K. Liu, S. Luo, M. Li, Y. Li, Y. Feng, B. Du, Y. Zhou, P. Lu, and I. Barth, "Detecting and characterizing the nonadiabaticity of laser-induced quantum tunneling," *Phys. Rev. Lett.* **122**, 053202 (2019).
- [195] J. B. Pendry, "Low energy electron diffraction: The theory and its application to determination of surface structure," (Academic Press Inc., 1974).
- [196] A. M. Rijs, E. H. G. Backus, C. A. De Lange, M. H. M. Janssen, K. Wang, and V. McKoy, "Rotationally resolved photoelectron spectroscopy of hot N₂ formed in the photofragmentation of N₂O," *J. Chem. Phys.* **114**, 9413 (2001).
- [197] L. Serrano-Andrés and B. O. Roos, "Theoretical study of the absorption and emission spectra of indole in the gas phase and in a solvent," *J. Am. Chem. Soc.* **118**, 185 (1996).
- [198] C. Dedonder-Lardeux, C. Jouvet, S. Perun, and A. L. Sobolewski, "External electric field effect on the lowest excited states of indole: *ab initio* and molecular dynamics study," *Phys. Chem. Chem. Phys.* **5**, 5118 (2003).
- [199] J. R. Platt, "Classification of spectra of cata-condensed hydrocarbons," *J. Chem. Phys.* **17**, 484 (1949).
- [200] M. Brouard, A. V. Green, F. Quadrini, and C. Vallance, "Photodissociation dynamics of OCS at 248 nm: The S(¹D₂) atomic angular momentum polarization," *J. Chem. Phys.* **127**, 084304 (2007).
- [201] H. Franz, O. Leupold, R. Röhlsberger, S. V. Roth, O. H. Seeck, J. Spengler, J. Strempler, M. Tischer, J. Viehhaus, E. Weckert, and T. Wroblewski, "Technical report: PETRA III: DESY's new high brilliance third generation synchrotron radiation source," *Synchrotron Radiat. News* **19**, 25 (2006).

- [202] J. Feldhaus, "FLASH – the first soft x-ray free electron laser (FEL) user facility," *J. Phys. B* **43**, 194002 (2010).
- [203] E. Allaria, R. Appio, L. Badano, W. A. Barletta, S. Bassanese, S. G. Biedron, A. Borgia, E. Busetto, D. Castronovo, P. Cinquegrana, S. Cleva, D. Cocco, M. Cornacchia, P. Craievich, I. Cudin, G. D'Auria, M. Dal Forno, M. B. Danailov, R. De Monte, G. De Ninno, P. Delgiusto, A. Demidovich, S. Di Mitri, B. Diviacco, A. Fabris, R. Fabris, W. Fawley, M. Ferianis, E. Ferrari, S. Ferry, L. Froehlich, P. Furlan, G. Gaio, F. Gelmetti, L. Giannessi, M. Giannini, R. Gobessi, R. Ivanov, E. Karantzoulis, M. Lonza, A. Lutman, B. Mahieu, M. Milloch, S. V. Milton, M. Musardo, I. Nikolov, S. Noe, F. Parmigiani, G. Penco, M. Petronio, L. Pivetta, M. Predonzani, F. Rossi, L. Rumiz, A. Salom, C. Scafuri, C. Serpico, P. Sigalotti, S. Spampinati, C. Spezzani, M. Svandrlik, C. Svetina, S. Tazzari, M. Trovo, R. Umer, A. Vascotto, M. Veronese, R. Visintini, M. Zaccaria, D. Zangrando, and M. Zangrando, "Highly coherent and stable pulses from the FERMI seeded free-electron laser in the extreme ultraviolet," *Nat. Photon.* **6**, 699 (2012).
- [204] J. Arthur, G. Materlik, R. Tatchyn, and H. Winick, "The LCLS: A fourth generation light source using the SLAC linac," *Rev. Sci. Instrum.* **66**, 1987 (1995).
- [205] S. Boutet and G. Williams, "The coherent x-ray imaging (CXI) instrument at the linac coherent light source (LCLS)," *New J. Phys.* **12**, 035024 (2010).
- [206] T. Kierspel, A. Morgan, J. Wiese, T. Mullins, A. Aquila, A. Barty, R. Bean, R. Boll, S. Boutet, P. Bucksbaum, H. N. Chapman, L. Christensen, A. Fry, M. Hunter, J. E. Koglin, M. Liang, V. Mariani, A. Natan, J. Robinson, D. Rolles, A. Rudenko, K. Schnorr, H. Stapelfeldt, S. Stern, J. Thøgersen, C. H. Yoon, F. Wang, and J. Küpper, "X-ray diffractive imaging of controlled gas-phase molecules: Toward imaging of dynamics in the molecular frame," *J. Chem. Phys.* **152**, 084307 (2020), arXiv:1910.13494 [physics].
- [207] A. Nomerotski, M. Brouard, E. Campbell, A. Clark, J. Crooks, J. Fopma, J. J. John, A. J. Johnsen, C. Slater, R. Turchetta, C. Vallance, E. Wilman, and W. H. Yuen, "Pixel imaging mass spectrometry with fast and intelligent pixel detectors," *J. Instrum.* **5**, C07007 (2010).
- [208] J. J. John, M. Brouard, A. Clark, J. Crooks, E. Halford, L. Hill, J. W. L. Lee, A. Nomerotski, R. Pisarczyk, I. Sedgwick, C. S. Slater, R. Turchetta, C. Vallance, E. Wilman, B. Winter, and W. H. Yuen, "PIImMS, a fast event-triggered monolithic pixel detector with storage of multiple timestamps," *J. Instrum.* **7**, C08001 (2012).
- [209] K. Amini, E. Savelyev, F. Brauße, N. Berrah, C. Bomme, M. Brouard, M. Burt, L. Christensen, S. Düsterer, B. Erk, H. Höppner, T. Kierspel, F. Krecinic, A. Lauer, J. W. L. Lee, M. Müller, E. Müller, T. Mullins, H. Redlin, N. Schirmel, J. Thøgersen, S. Techert, S. Toleikis, R. Treusch, S. Trippel, A. Ulmer, C. Vallance, J. Wiese, P. Johnsson, J. Küpper, A. Rudenko, A. Rouzée, H. Stapelfeldt, D. Rolles, and R. Boll, "Photodissociation of aligned CH₃I and C₆H₃F₂I molecules probed with time-resolved Coulomb explosion imaging by site-selective extreme ultraviolet ionization," *Struct. Dyn.* **5**, 014301 (2018).
- [210] E. Savelyev, R. Boll, C. Bomme, N. Schirmel, H. Redlin, B. Erk, S. Düsterer, E. Müller, H. Höppner, S. Toleikis, J. Müller, M. Kristin Czwalińska, R. Treusch, T. Kierspel, T. Mullins, S. Trippel, J. Wiese, J. Küpper, F. Brauße, F. Krecinic, A. Rouzée, P. Rudawski, P. Johnsson, K. Amini, A. Lauer, M. Burt, M. Brouard, L. Christensen, J. Thøgersen, H. Stapelfeldt, N. Berrah, M. Müller, A. Ulmer, S. Techert, A. Rudenko, and D. Rolles, "Jitter-correction for IR/UV-XUV pump-probe experiments at the FLASH free-electron laser," *New J. Phys.* **19**, 043009 (2017).
- [211] J. Rothhardt, S. Hädrich, Y. Shamir, M. Tschernajew, R. Klas, A. Hoffmann, G. K. Tadesse, A. Klenke, T. Gottschall, T. Eidam, J. Limpert, A. Tünnemann, R. Boll, C. Bomme, H. Dachraoui, B. Erk, M. Di Fraia, D. A. Horke, T. Kierspel, T. Mullins, A. Przystawik, E. Savelyev, J. Wiese, T. Laarmann, J. Küpper, and D. Rolles, "High-repetition-rate and high-

- photon-flux 70 eV high-harmonic source for coincidence ion imaging of gas-phase molecules,” *Opt. Exp.* **24**, 18133 (2016).
- [212] J. Viefhaus, F. Scholz, S. Deinert, L. Glaser, M. Ilchen, J. Seltmann, P. Walter, and F. Siewert, “The variable polarization XUV beamline P04 at PETRA III: Optics, mechanics and their performance,” *Nucl. Instrum. Meth. A* **710**, 151 (2013).
- [213] T. Kierspel, C. Bomme, M. Di Fraia, J. Wiese, D. Anielski, S. Bari, R. Boll, B. Erk, J. S. Kienitz, N. L. M. Müller, D. Rolles, J. Viefhaus, S. Trippel, and J. Küpper, “Photophysics of indole upon x-ray absorption,” *Phys. Chem. Chem. Phys.* **20**, 20205 (2018), arXiv:1802.02964 [physics].
- [214] M. Burt, R. Boll, J. W. L. Lee, K. Amini, H. Köckert, C. Vallance, A. S. Gentleman, S. R. Mackenzie, S. Bari, C. Bomme, S. Düsterer, B. Erk, B. Manschwetus, E. Müller, D. Rompotis, E. Savelyev, N. Schirmel, S. Techert, R. Treusch, J. Küpper, S. Trippel, J. Wiese, H. Stapelfeldt, B. Cunha de Miranda, R. Guillemin, I. Ismail, L. Journal, T. Marchenko, J. Palaudoux, F. Penent, M. N. Piancastelli, M. Simon, O. Travnikova, F. Brauße, G. Goldsztejn, A. Rouzée, M. Géléoc, R. Geneaux, T. Ruchon, J. Underwood, D. M. P. Holland, A. S. Mereshchenko, P. K. Olshin, P. Johnsson, S. Maclot, J. Lahl, A. Rudenko, F. Ziaee, M. Brouard, and D. Rolles, “Coulomb-explosion imaging of concurrent CH₂BrI photodissociation dynamics,” *Phys. Rev. A* **96**, 043415 (2017).
- [215] F. Brauße, G. Goldsztejn, K. Amini, R. Boll, S. Bari, C. Bomme, M. Brouard, M. Burt, B. Cunha de Miranda, S. Düsterer, B. Erk, M. Géléoc, R. Geneaux, A. S. Gentleman, R. Guillemin, I. Ismail, P. Johnsson, L. Journal, T. Kierspel, H. Köckert, J. Küpper, P. Lablanquie, J. Lahl, J. W. L. Lee, S. R. Mackenzie, S. Maclot, B. Manschwetus, A. S. Mereshchenko, T. Mullins, P. K. Olshin, J. Palaudoux, S. Patchkovskii, F. Penent, M. N. Piancastelli, D. Rompotis, T. Ruchon, A. Rudenko, E. Savelyev, N. Schirmel, S. Techert, O. Travnikova, S. Trippel, J. G. Underwood, C. Vallance, J. Wiese, M. Simon, D. M. P. Holland, T. Marchenko, A. Rouzée, and D. Rolles, “Time-resolved inner-shell photoelectron spectroscopy: From a bound molecule to an isolated atom,” *Phys. Rev. A* **97**, 043429 (2018).
- [216] F. Allum, M. Burt, K. Amini, R. Boll, H. Köckert, P. K. Olshin, S. Bari, C. Bomme, F. Brauße, B. Cunha de Miranda, S. Düsterer, B. Erk, M. Géléoc, R. Geneaux, A. S. Gentleman, G. Goldsztejn, R. Guillemin, D. M. P. Holland, I. Ismail, P. Johnsson, L. Journal, J. Küpper, J. Lahl, J. W. L. Lee, S. Maclot, S. R. Mackenzie, B. Manschwetus, A. S. Mereshchenko, R. Mason, J. Palaudoux, M. N. Piancastelli, F. Penent, D. Rompotis, A. Rouzée, T. Ruchon, A. Rudenko, E. Savelyev, M. Simon, N. Schirmel, H. Stapelfeldt, S. Techert, O. Travnikova, S. Trippel, J. G. Underwood, C. Vallance, J. Wiese, F. Ziaee, M. Brouard, T. Marchenko, and D. Rolles, “Coulomb explosion imaging of CH₃I and CH₂ClI photodissociation dynamics,” *J. Chem. Phys.* **149**, 204313 (2018).
- [217] V. Lyamayev, Y. Ovcharenko, R. Katzy, M. Devetta, L. Bruder, A. LaForge, M. Mudrich, U. Person, F. Stienkemeier, M. Krikunova, T. Moeller, P. Piseri, L. Avaldi, M. Coreno, P. O’Keeffe, P. Bolognesi, M. Alagia, A. Kivimaeki, M. Di Fraia, N. B. Brauer, M. Drabbels, T. Mazza, S. Stranges, P. Finetti, C. Grazioli, O. Plekan, R. Richter, K. C. Prince, and C. Callegari, “A modular end-station for atomic, molecular, and cluster science at the low density matter beamline of FERMI@Elettra,” *J. Phys. B* **46**, 164007 (2013).
- [218] J. D. Bozek, “AMO instrumentation for the LCLS x-ray FEL,” *Eur. Phys. J. Special Topics* **169**, 129 (2009).
- [219] A. Zhao, M. van Beuzekom, B. Bouwens, D. Byelov, I. Chakaberia, C. Cheng, E. Maddox, A. Nomerotski, P. Svihra, J. Visser, V. Vrba, and T. Weinacht, “Coincidence velocity map imaging using Tpx3Cam, a time stamping optical camera with 1.5 ns timing resolution,” *Rev. Sci. Instrum.* **88**, 113104 (2017), arXiv:1707.06253 [physics].
- [220] M. Johnny, C. A. Schouder, A. Al-Refaie, L. He, J. Wiese, H. Stapelfeldt, S. Trippel, and J. Küpper, “Water as radiation protection agent for ionized pyrrole,” (2020), in preparation.

- [221] M. Johny, C. A. Schouder, A. Al-Refaie, J. Wiese, H. Stapelfeldt, S. Trippel, and J. Küpper, "Enhanced strong-field ionization of pyrrole in a microsolvated environment," (2020), in preparation.
- [222] X. Andrade, D. Strubbe, U. De Giovannini, A. H. Larsen, M. J. T. Oliveira, J. Alberdi-Rodriguez, A. Varas, I. Theophilou, N. Helbig, M. J. Verstraete, L. Stella, F. Nogueira, A. Aspuru-Guzik, A. Castro, M. A. L. Marques, and A. Rubio, "Real-space grids and the Octopus code as tools for the development of new simulation approaches for electronic systems," *Phys. Chem. Chem. Phys.* **17**, 31371 (2015).
- [223] C. Legrand, E. Suraud, and P. G. Reinhard, "Comparison of self-interaction-corrections for metal clusters," *J. Phys. B* **35**, 1115 (2002).
- [224] L. S. Wang, J. E. Reutt, Y. T. Lee, and D. A. Shirley, "High-resolution UV photoelectron-spectroscopy of CO_2^+ , COS^+ and CS_2^+ using supersonic molecular-beams," *J. Electron. Spectrosc. Relat. Phenom.* **47**, 167 (1988).
- [225] U. De Giovannini, A. H. Larsen, and A. Rubio, "Modeling electron dynamics coupled to continuum states in finite volumes with absorbing boundaries," *Eur. Phys. J. D* **88**, 1 (2015).
- [226] H. Akagi, T. Otobe, A. Staudte, A. Shiner, F. Turner, R. Dörner, D. Villeneuve, and P. Corkum, "Laser tunnel ionization from multiple orbitals in HCl," *Science* **325**, 1364 (2009).
- [227] C. Brand, J. Küpper, D. W. Pratt, W. L. Meerts, D. Krügler, J. Tatchen, and M. Schmitt, "Vibronic coupling in indole: I. theoretical description of the 1L_a - 1L_b interaction and the electronic spectrum," *Phys. Chem. Chem. Phys.* **12**, 4968 (2010).
- [228] W. Caminati and S. Di Bernardo, "Microwave spectrum and amino hydrogen location in indole," *J. Mol. Struct.* **240**, 253 (1990).
- [229] R. D. Johnson, III, ed., *NIST Computational Chemistry Comparison and Benchmark Database* (NIST Standard Reference Database Number 101, Release 20, 2019).

Acknowledgements

Many people contributed to this work and supported me in one way or another during my time as a doctoral student. I am truly grateful to all of them.

First of all, I would like to thank my supervisor, Jochen Küpper, for giving me the opportunity to join his great research group, the Controlled Molecule Imaging group, and to do science in such a highly collaborative and motivating environment, in the Center for Free-Electron Laser Science and at DESY. I was lucky to have such fine fellow group members to mutually tackle many kinds of exciting problems and projects, and to have many coffee sessions with wonderfully absurd conversations. Thanks for the good time, folks!

To Sebastian Trippel I owe particular thanks. For he taught me so many essential lessons on my way towards becoming a scientist. I feel deeply grateful for his continuous professional and personal support throughout the past years as well as for his inspiring enthusiasm for science and fundamental research.

Being part of the 47c-lab team, with all its bright former and current members, was a great benefit for me. Nele Müller and Jens Kienitz made my first years in the team a very enjoyable time and introduced me to many important aspects of daily life in the laboratory. The time spent with Andrea Trabattoni, while we were working together on the kHz2 machine and during all our passionate discussions on molecular and laser physics, was super instructive and at the same time a great pleasure for me. The cheering presence of Melby Johny always put me in high spirits, making all the beamtime, laboratory and programming work that we did together real fun experiences. I would like to thank Evangelos Karamatskos for the exciting discussions on photoelectron imaging and laser-induced electron diffraction. Moreover, I want to say thank you to Thomas Kierspel for his good-humoured, pragmatic attitude even in stressful times and for teaching me many things regarding experiments at free-electron laser facilities. Terry Mullins assumes a special place among my former colleagues. I am truly grateful to him for helping me with his wide range of skills, for infecting me with his passion for science as well as for sharing my excitement for unexpected mathematics and physics problems. Furthermore, I am deeply indebted to Jolijn Onvlee, with whom I had the pleasure to work on several molecular-physics campaigns. Her keen interest for scientific discovery in combination with great skills and precision left a lasting impression on me. I admire her always-friendly and highly collaborative way to do science.

Also, I would like to thank all the collaborators, with whom I had the opportunity to perform numerous exciting experiments at synchrotron and free-electron laser facilities, in particular Daniel Rolles and his former team. Moreover, I would like to thank Sang-Kil Son for fruitful discussions on molecular structure and strong-field ionisation. To Karol Długołęcki I feel much obliged for his precise and dedicated work whenever I needed his outstanding engineering talents. Another person without whom I would not have been able to finish my doctoral work is Barbora Vagovič. I would like to heartily thank her for helping me to not get lost in the jungle of bureaucracy.

In particular Nils Roth, Helen Bieker, Lena Worbs and Pau González Caminal made my time as a doctoral student so much more enjoyable. Thank you for all the delightful moments with you that helped me to forget about work when I urgently needed it.

Finally, I would like to express my gratitude to my dear parents and my bunch of weird, beloved friends, who were a massive emotional support for me during the past years and helped me to overcome all the different kinds of frustration that one encounters as a doctoral student.

Acronyms

ADK	Ammosov-Delone-Krainov
ATI	above-threshold ionisation
CEI	Coulomb-explosion imaging
CMI	Controlled Molecule Imaging
FWHM	full width at half maximum
HOMO	highest occupied molecular orbital
LIED	laser-induced electron diffraction
MCP	microchannel plate
MF-ARPES	molecular-frame angle-resolved photoelectron spectra
OCS	carbonyl sulfide
PEMD	photoelectron momentum distribution
PImMS	Pixel Imaging Mass Spectrometry
PPT	Perelomov-Popov-Terentev
QRS	quantitative recattering theory
REMPI	resonance-enhanced multiphoton ionisation
SCA	semiclassical approximation
SFA	strong-field approximation
TDDFT	time-dependent density functional theory
TDSE	time-dependent Schrödinger equation
VMI	velocity-map imaging
VMIS	velocity-map imaging spectrometer

Chemical hazard and precautionary statements

carbonyl sulfide (CAS number: 463-58-1)

hazard pictograms:



hazard statements:

H220	Extremely flammable gas.
H280	Contains gas under pressure; may explode if heated.
H315	Causes skin irritation.
H319	Causes serious eye irritation.
H331	Toxic if inhaled.
H335	May cause respiratory irritation.

precautionary statements:

P210	Keep away from heat, hot surfaces, sparks, open flames and other ignition sources. No smoking.
P302+P352	IF ON SKIN: Wash with plenty of water.
P304+P340+P311	IF INHALED: Remove person to fresh air and keep comfortable for breathing. Call a POISON CENTER/doctor.
P305+P351+P338	IF IN EYES: Rinse cautiously with water for several minutes. Remove contact lenses if present and easy to do. Continue rinsing.
P410+P403	Protect from sunlight. Store in a well-ventilated place.

chloriodomethane (CAS number: 593-71-5)

hazard pictograms:



hazard statements:

H301+H331	Toxic if swallowed.
H315	Causes skin irritation.
H319	Causes serious eye irritation.
H335	May cause respiratory irritation.

precautionary statements:

P261	Avoid breathing dust/fumes/gas/mist/vapours/spray.
P264	Wash hands thoroughly after handling.
P270	Do not eat, drink or smoke when using this product.
P301+P310	IF SWALLOWED: Immediately call a POISON CENTER/doctor.
P302+P352	IF ON SKIN: Wash with plenty of water.
P305+P351+P338	IF IN EYES: Rinse cautiously with water for several minutes. Remove contact lenses if present and easy to do. Continue rinsing.

bromoiodomethane (CAS number: 557-68-6)

hazard pictograms:



hazard statements:

H315 Causes skin irritation.
H318 Causes serious eye damage.
H335 May cause respiratory irritation.

precautionary statements:

P280 Wear protective gloves/protective clothing.
P302+P352 IF ON SKIN: Wash with plenty of water.
P305+P351+P338+P310 IF IN EYES: Rinse cautiously with water for several minutes. Remove contact lenses if present and easy to do. Continue rinsing. Immediately call a POISON CENTER/doctor.

2,6-difluoroiodobenzene (CAS number: 13697-89-7)

hazard pictograms:



hazard statements:

H301 Toxic if swallowed.

precautionary statements:

P301+P310+P330 IF SWALLOWED: Immediately call a POISON CENTER/doctor. Rinse mouth.

2,5-diiodothiophene (CAS number: 625-88-7)

hazard pictograms:



hazard statements:

H315	Causes skin irritation.
H319	Causes serious eye irritation.
H335	May cause respiratory irritation.

precautionary statements:

P261	Avoid breathing dust.
P280	Wear protective gloves/protective clothing/eye protection/face protection.
P302+P352	IF ON SKIN: Wash with plenty of water.
P304+P340	IF INHALED: Remove person to fresh air and keep comfortable for breathing.
P305+P351+P338	IF IN EYES: Rinse cautiously with water for several minutes. Remove contact lenses if present and easy to do. Continue rinsing.
P312	Call a POISON CENTER/doctor, if you feel unwell.
P332+P313	If skin irritation occurs, get medical advice/attention.
P337+P313	If eye irritation persists, get medical advice/attention.

indole (CAS number: 120-72-9)

hazard pictograms:



hazard statements:

H302	Harmful if swallowed.
H311	Toxic in contact with skin.
H315	Causes skin irritation.
H318	Causes serious eye damage.
H335	May cause respiratory irritation.
H400	Very toxic to aquatic life.

precautionary statements:

P261	Avoid breathing dust.
P273	Avoid release to the environment.
P280	Wear protective gloves/protective clothing/eye protection/face protection.
P305+P351+P338	IF IN EYES: Rinse cautiously with water for several minutes. Remove contact lenses if present and easy to do. Continue rinsing.
P312	Call a POISON CENTER/doctor, if you feel unwell.

iodomethane (CAS number: 74-88-4)

hazard pictograms:



hazard statements:

H226	Flammable liquid and vapour.
H301+H331	Toxic if swallowed or if inhaled.
H312	Harmful in contact with skin.
H315	Causes skin irritation.
H319	Causes serious eye irritation.
H335	May cause respiratory irritation.
H351	Suspected of causing cancer.
H410	Very toxic to aquatic life with long lasting effects.

precautionary statements:

P201	Obtain special instructions before use.
P210	Keep away from heat, hot surfaces, sparks, open flames and other ignition sources. No smoking.
P273	Avoid release to the environment.
P280	Wear protective gloves/protective clothing.
P301+P310+P330	IF SWALLOWED: Immediately call a POISON CENTER/doctor. Rinse mouth.
P302+P352+P312	IF ON SKIN: Wash with plenty of water. Call a POISON CENTER/doctor, if you feel unwell.

phenanthrene (CAS number: 85-01-8)

hazard pictograms:



hazard statements:

H302	Harmful if swallowed.
H410	Very toxic to aquatic life with long lasting effects.

precautionary statements:

P273	Avoid release to the environment.
P280	Wear protective gloves/protective clothing.
P301+P312+P330	IF SWALLOWED: Call a POISON CENTER/doctor, if you feel unwell. Rinse mouth.

pyrene (CAS number: 129-00-0)

hazard pictograms:



hazard statements:

H410 Very toxic to aquatic life with long lasting effects.

precautionary statements:

P273 Avoid release to the environment.

pyrrole (CAS number: 109-97-7)

hazard pictograms:



hazard statements:

H226 Flammable liquid and vapour.

H301 Toxic if swallowed.

H318 Causes serious eye damage.

H332 Harmful if inhaled.

precautionary statements:

P210 Keep away from heat, hot surfaces, sparks, open flames and other ignition sources. No smoking.

P280 Wear protective gloves/protective clothing.

P305+P351+P338 IF IN EYES: Rinse cautiously with water for several minutes. Remove contact lenses if present and easy to do. Continue rinsing.

P308+P310 If exposed or concerned: Immediately call a POISON CENTER/doctor.

2(5H)-thiophenone (CAS number: 3354-32-3)

hazard pictograms:



hazard statements:

H315 Causes skin irritation.

H319 Causes serious eye irritation.

H335 May cause respiratory irritation.

precautionary statements:

P302+P352 IF ON SKIN: Wash with plenty of water.

P305+P351+P338 IF IN EYES: Rinse cautiously with water for several minutes. Remove contact lenses if present and easy to do. Continue rinsing.

List of publications

Publications related to this thesis:

- 1 T. Kierspel, J. Wiese, T. Mullins, J. Robinson, A. Aquila, A. Barty, R. Bean, R. Boll, S. Boutet, P. Bucksbaum, H. N. Chapman, L. Christensen, A. Fry, M. Hunter, J. E. Koglin, M. Liang, V. Mariani, A. Morgan, A. Natan, V. Petrovic, D. Rolles, A. Rudenko, K. Schnorr, H. Stapelfeldt, S. Stern, J. Thøgersen, C. H. Yoon, F. Wang, S. Trippel, and J. Küpper, "Strongly aligned molecules at free-electron lasers," *J. Phys. B* **48**, 204002 (2015).
- 2 J. Rothhardt, S. Hädrich, Y. Shamir, M. Tschernajew, R. Klas, A. Hoffmann, G. K. Tadesse, A. Klenke, T. Gottschall, T. Eidam, J. Limpert, A. Tünnermann, R. Boll, C. Bomme, H. Dachraoui, B. Erk, M. Di Fraia, D. A. Horke, T. Kierspel, T. Mullins, A. Przystawik, E. Savelyev, J. Wiese, T. Laarmann, J. Küpper, and D. Rolles, "High-repetition-rate and high-photon-flux 70 eV high-harmonic source for coincidence ion imaging of gas-phase molecules," *Opt. Exp* **24**, 18133 (2016).
- 3 E. Savelyev, R. Boll, C. Bomme, N. Schirmel, H. Redlin, B. Erk, S. Düsterer, E. Müller, H. Höppner, S. Toleikis, J. Müller, M. K. Czwalinna, R. Treusch, T. Kierspel, T. Mullins, S. Trippel, J. Wiese, J. Küpper, F. Brauße, F. Krecinic, A. Rouzée, P. Rudawski, P. Johnsson, K. Amini, A. Lauer, M. Burt, M. Brouard, L. Christensen, J. Thøgersen, H. Stapelfeldt, N. Berrah, M. Müller, A. Ulmer, S. Techert, A. Rudenko, D. Rolles, "Jitter-correction for IR/UV-XUV pump-probe experiments at the FLASH free-electron laser," *New J. Phys.* **19**, 043009 (2017).
- 4 M. Di Fraia, P. Finetti, R. Richter, K. C. Prince, J. Wiese, M. Devetta, M. Negro, C. Vozzi, A. G. Ciriolo, A. Pusala, A. Demidovich, M. B. Danailov, E. T. Karamatskos, S. Trippel, J. Küpper, and C. Callegari, "Impulsive laser-induced alignment of OCS molecules at FERMI," *Phys. Chem. Chem. Phys.* **19**, 19733 (2017).
- 5 K. Amini, R. Boll, A. Lauer, M. Burt, J. W. L. Lee, L. Christensen, F. Brauße, T. Mullins, E. Savelyev, U. Ablikim, N. Berrah, C. Bomme, S. Düsterer, B. Erk, H. Höppner, P. Johnsson, T. Kierspel, F. Krecinic, J. Küpper, M. Müller, E. Müller, H. Redlin, A. Rouzée, N. Schirmel, J. Thøgersen, S. Techert, S. Toleikis, R. Treusch, S. Trippel, A. Ulmer, J. Wiese, C. Vallance, A. Rudenko, H. Stapelfeldt, M. Brouard, and D. Rolles, "Alignment, orientation, and Coulomb explosion of difluoroiodobenzene studied with the pixel imaging mass spectrometry (PIImMS) camera," *J. Chem. Phys.* **147**, 013933 (2017).
- 6 M. Burt, R. Boll, J. W. L. Lee, K. Amini, H. Köckert, C. Vallance, A. S. Gentleman, S. R. Mackenzie, S. Bari, C. Bomme, S. Düsterer, B. Erk, B. Manschwetus, E. Müller, D. Rompotis, E. Savelyev, N. Schirmel, S. Techert, R. Treusch, J. Küpper, S. Trippel, J. Wiese, H. Stapelfeldt, B. Cunha de Miranda, R. Guillemin, I. Ismail, L. Journal, T. Marchenko, J. Palaudoux, F. Penent, M. N. Piancastelli, M. Simon, O. Travnikova, F. Brauße, G. Goldsztejn, A. Rouzée, M. Géléoc, R. Geneaux, T. Ruchon, J. Underwood, D. M. P. Holland, A. S. Mereshchenko, P. K. Olshin, P. Johnsson, S. Maclot, J. Lahl, A. Rudenko, F. Ziaee, M. Brouard, and D. Rolles, "Coulomb-explosion imaging of concurrent CH₂BrI photodissociation dynamics," *Phys. Rev. A* **96**, 043415 (2017).
- 7 K. Amini, E. Savelyev, F. Brauße, N. Berrah, C. Bomme, M. Brouard, M. Burt, L. Christensen, S. Düsterer, B. Erk, H. Höppner, T. Kierspel, F. Krecinic, A. Lauer, J. W. L. Lee, M. Müller, E. Müller, T. Mullins, H. Redlin, N. Schirmel, J. Thøgersen, S. Techert, S. Toleikis, R. Treusch, S. Trippel, A. Ulmer, C. Vallance, J. Wiese, P. Johnsson, J. Küpper, A. Rudenko, A. Rouzée, H. Stapelfeldt, D. Rolles, and R. Boll, "Photodissociation of aligned CH₃I and C₆H₃F₂I molecules probed with time-resolved Coulomb explosion imaging by site-selective extreme ultraviolet

- ionization," *Struct. Dyn.* **5**, 014301 (2018).
- 8 S. Trippel, J. Wiese, T. Mullins, and J. Küpper, "Communication: Strong laser alignment of solvent-solute aggregates in the gas-phase," *J. Chem. Phys.* **148**, 101103 (2018).
 - 9 F. Brauße, G. Goldsztejn, K. Amini, R. Boll, S. Bari, C. Bomme, M. Brouard, M. Burt, B. Cunha de Miranda, S. Düsterer, B. Erk, M. Géléoc, R. Geneaux, A. S. Gentleman, R. Guillemin, I. Ismail, P. Johnsson, L. Journal, T. Kierspel, H. Köckert, J. Küpper, P. Lablanquie, J. Lahl, J. W. L. Lee, S. R. Mackenzie, S. Maclot, B. Manschwetus, A. S. Mereshchenko, T. Mullins, P. K. Olshin, J. Palaudoux, S. Patchkovskii, F. Penent, M. N. Piancastelli, D. Rompotis, T. Ruchon, A. Rudenko, E. Savelyev, N. Schirmel, S. Techert, O. Travnikova, S. Trippel, J. G. Underwood, C. Vallance, J. Wiese, M. Simon, D. M. P. Holland, T. Marchenko, A. Rouzée, and D. Rolles, "Time-resolved inner-shell photoelectron spectroscopy: From a bound molecule to an isolated atom," *Phys. Rev. A* **97**, 043429 (2018).
 - 10 T. Kierspel, C. Bomme, M. Di Fraia, J. Wiese, D. Anielski, S. Bari, R. Boll, B. Erk, J. S. Kienitz, N. L. M. Müller, D. Rolles, J. Viefhaus, S. Trippel, and J. Küpper, "Photophysics of indole upon x-ray absorption," *Phys. Chem. Chem. Phys.* **20**, 20205 (2018).
 - 11 F. Allum, M. Burt, K. Amini, R. Boll, H. Köckert, P. K. Olshin, S. Bari, C. Bomme, F. Brauße, B. Cunha de Miranda, S. Düsterer, B. Erk, M. Géléoc, R. Geneaux, A. S. Gentleman, G. Goldsztejn, R. Guillemin, D. M. P. Holland, I. Ismail, P. Johnsson, L. Journal, J. Küpper, J. Lahl, J. W. L. Lee, S. Maclot, S. R. Mackenzie, B. Manschwetus, A. S. Mereshchenko, R. Mason, J. Palaudoux, M. N. Piancastelli, F. Penent, D. Rompotis, A. Rouzée, T. Ruchon, A. Rudenko, E. Savelyev, M. Simon, N. Schirmel, H. Stapelfeldt, S. Techert, O. Travnikova, S. Trippel, J. G. Underwood, C. Vallance, J. Wiese, F. Ziaee, M. Brouard, T. Marchenko, and D. Rolles, "Coulomb explosion imaging of CH₃I and CH₂ClI photodissociation dynamics," *J. Chem. Phys.* **149**, 204313 (2018).
 - 12 J. Wiese, J.-F. Olivieri, A. Trabattoni, S. Trippel, and J. Küpper, "Strong-field photoelectron momentum imaging of OCS at finely resolved incident intensities," *New J. Phys.* **21**, 083011 (2019).
 - 13 T. Kierspel, A. Morgan, J. Wiese, T. Mullins, A. Aquila, A. Barty, R. Bean, R. Boll, S. Boutet, P. Bucksbaum, H. N. Chapman, L. Christensen, A. Fry, M. Hunter, J. E. Koglin, M. Liang, V. Mariani, A. Natan, J. Robinson, D. Rolles, A. Rudenko, K. Schnorr, H. Stapelfeldt, S. Stern, J. Thøgersen, C. H. Yoon, F. Wang, and J. Küpper, "X-ray diffractive imaging of controlled gas-phase molecules: Toward imaging of dynamics in the molecular frame," *J. Chem. Phys.* **152**, 084307 (2020).
 - 14 A. Trabattoni, J. Wiese, U. De Giovannini, J.-F. Olivieri, T. Mullins, J. Onvlee, S.-K. Son, B. Frusteri, A. Rubio, S. Trippel, and J. Küpper, "Setting the photoelectron clock through molecular alignment," *Nat. Commun.* **11**, 2546 (2020).
 - 15 J. Wiese, J. Onvlee, S. Trippel, and J. Küpper, "Strong-field ionization of complex molecules," arXiv:2003.02116 [physics] (2020), under review.
 - 16 J. Wiese, S. Trippel, and J. Küpper, "Disentangling strong-field multiphoton ionization of a complex molecule through photoelectron tomography," in preparation.
 - 17 T. Mullins, E. T. Karamatskos, J. Wiese, J. Onvlee, A. Yachmenev, A. Rouzée, S. Trippel, and J. Küpper, "Toward three-dimensional field-free alignment of arbitrary asymmetric top molecules," in preparation.
 - 18 M. Johny, C. A. Schouder, A. Al-Refaie, L. He, J. Wiese, H. Stapelfeldt, S. Trippel, and J. Küpper, "Water as radiation protection agent for ionized pyrrole," in preparation.
 - 19 M. Johny, C. A. Schouder, A. Al-Refaie, J. Wiese, H. Stapelfeldt, S. Trippel, and J. Küpper, "Enhanced strong-field ionization of pyrrole in a microsolvated environment," in preparation.

Other publications:

- 1 S. Wang, S. Schatz, M. C. Stuhldreier, H. Böhnke, J. Wiese, C. Schröder, T. Raeker, B. Hartke, J. K. Keppler, K. Schwarz, F. Renth, and F. Temps, "Ultrafast dynamics of UV-excited *trans*- and *cis*-ferulic acid in aqueous solutions", J. Chem. Phys. **19**, 30683 (2017)